Development of the 2-Component-Injection Moulding for Metal Powders

Ana Paula Cysne Barbosa

JÜLICH
FORSCHUNGSZENTRUM

Development of the 2-Component-Injection Moulding for Metal Powders

Ana Paula Cysne Barbosa

Abstract

2-Component-Metal Injection Moulding (2-C-MIM) is a technique derived from plastics industry which has been adapted to metal powders. By using this technology, the production of titanium parts combining dense and porous parts becomes possible. Such a structure with a gradient in porosity is attractive for biomedical implants, as the pores promote a mechanical interlock between bone tissue and implant material. The dense part of the structure is responsible for the mechanical stability of the implant.

For the fabrication of metal parts with a gradient in porosity, feedstocks with and without space holder particles are employed. A 2-C-MIM machine and a specifically designed tool are used for the combination of these feedstocks in the same green part. After removal of the binder and space holder material, the parts are sintered and a structure with a gradient in porosity is obtained.

First 2-C-MIM experiments were conducted with a standard binder system previously developed at the institute IEK-1 at *Forschungszentrum Jülich*. Results achieved with this binder system indicated binder-powder phase separation during injection, which occurred due to the low viscosity of the binder system used (0.15 Pa·s). The need for the development of a new binder system with a more suitable flowing behaviour became clear. Moreover, the partial debinding method employed so far (wicking) needed to be substituted by another method with a more industrial approach.

New binder systems comprising a wide range of viscosity were developed, where the partial debinding method employed was solvent extraction in n-hexane. A binder system with a viscosity of 12.4 Pa·s was chosen for further investigations, due to the suitability of flowing behaviour of its feedstock. The viscosity of feedstocks was measured, where the use of space holder particles was found to decrease viscosity. After addition of stearic acid and optimisation of the solids content, feedstocks with 72 and 64 Vol.% solids loading (with and without space holder, respectively) were used in injection moulding trials.

After optimisation of the injection temperature of feedstock, prototypes of titanium spinal implants with a gradient in porosity were successfully produced and characterised. The availability of the net-shape production of such implants by 2-C-MIM means a reduction of costs in case of large scale production, as compared to the fabrication method current employed (pressing and green machining).

Index

Abbreviations and Symbols

2-C-MIM	2-Component-Metal Injection Moulding
3DP	3-Dimensional Printing
CIM	Ceramic Injection Moulding
CVD	Chemical Vapour Deposition
DGF	Deutsche Gessellschaft für Fettwissenschaft (German Association for Fat Science)
DSC	Differential Scanning Calorimetry
DTG	Derivative Thermogravimetry
EBM	Electron Beam Melting
HDPE	High-density polyethylene
HIP	Hot isostatic pressing
LDPE	Low-density polyethylene
LLDPE	Linear low-density polyethylene
LM	Light Microscopy
MIM	Metal Injection Moulding
MMD	Molecular mass distribution
PIM	Powder Injection Moulding
PLIF	Posterior Lumbar Interbody Fusion
PMMA	Poly(methyl methacrylate)
SEM	Scanning Electron Microscopy
SHM	Space Holder Method
SLM	Selective Laser Melting
SPS	Spark Plasma Sintering
TGA	Thermogravimetric Analysis
XPS	X-ray Photoelectron Spectroscopy

List of Figures

List of Figures

VIII

List of Tables

1 Introduction and objectives

The human body is always subjected to diseases, where tissues or organs fail to function properly. With advances in medicine, sometimes the suitable treatment involves the introduction of artificial implants into the body. Much effort of scientists has been put on investigating materials which are able to fulfil the requirements for implantation into the body and to decrease recovering time of the patient after a surgery. The investigation of new structures which would alleviate patient suffering and make implant materials more accessible by reduction of production costs is of much interest.

Titanium is a traditional implant material with proven biocompatibility to the body, corrosion resistance and mechanical performance. It has been already in use for implantation devices for decades, where one of the uses of the material is as bone substitution. In this case, good adhesion to adjacent bone tissue is crucial. The implant may be cemented in place using polymethylmethacrylate (PMMA), so that the actual interface with the bone is the PMMA material. Another alternative is to modify the implant surface and create an open porous network to promote bone ingrowth (osseointegration). This ingrowth promotes a mechanical interlock between implant and the bone, where pores in the range of 350-500 μm are discussed to be preferrentially suitable for this purpose.

Besides improving mechanical interlocking between bone and implant, the use of porous structures brings with it another advantage. The stiffness mismatch between bone and implant, which may lead to stress-shielding, is diminished by using porous structures. By choosing the adequate porosity, mechanical properties similar to the ones of the bone can be obtained.

For load-bearing implants, a combination of a dense and porous structure or a gradient in porosity is often the best compromise to achieve sufficient stability and osseointegration. The porous part of the implant is responsible for promoting the osseointegration and the dense part for the mechanical stability.

There are many methods of production of porous metallic structures, where gas-releasing foaming agents, physical vapour deposition (PVD) on cellular performs, spark plasma sintering (SPS), plasma spraying and the space holder method (SHM) are some of the methods employed. Hereby the space holder method highlights itself due to the good homogeneity of the porous structure produced, high porosity and shape control of the pores as compared to the other methods. In this case, porous titanium is produced by adding space holder particles to the metal powder particles, pressing and green machining to the desired

shape. After removal of the space holder particles, the part is sintered. A gradient in porosity can be obtained if powder mixtures with varying amounts of space holder material are combined during the compaction step. If a large number of parts are to be produced, the method is limited due to the mechanical machining of the parts. To overcome this, the development of a method which enables the net-shape manufacturing of porous titanium implants has been under investigation at the institute IEK-1 at *Forschungszentrum Jülich* during the last years, where the metal injection moulding (MIM) technique has been investigated in detail.

The MIM technique enables the mass production of near-net-shape parts by the injection of feedstocks composed of a metal powder with a binder system. The method is similar to plastics injection moulding and enables the production of parts with complex shapes. After moulding, the part is partially debinded and sintered. Recently, the space holder method using NaCl as space holder has been adapted in combination to metal injection moulding at the institute IEK-1 at *Forschungszentrum Jülich* for the production of porous implants. By adding space holder particles to the feedstock, the near-net-shape production of porous parts with high porosities was made possible. After the partial debinding, a dissolution step for the removal of the space holder particles is added to the process. Up to now, the production of parts with simple geometries like cylinders or discs was investigated, where preliminary studies of the mechanical and biological properties of the materials were conducted. In these studies, the partial debinding method used was the wicking method, which consists in immersing the green part in a sand bed and removing a binder component by capillary forces. The method is laborious and thereby disadvantageous to the industrial operation. Further disadvantages are expected due to the low viscosity of the binder system used, which enhances the risk of separation of the binder from the powder particles in the case of more complex-shaped cavities.

The 2-component-metal injection moulding (2-C-MIM) is a technique which enables the combination of two different feedstocks in the same part. By injecting feedstocks from different injection units, it becomes possible to combine different materials and produce parts with complementing characteristics. The combination feedstocks with and without space holder in an automated 2-C-MIM process would enable the near-net-shape production of implants with a gradient in porosity. This would be the only technique suitable for large scale production of parts combining homogeneous pore structure with control of pore shape, high porosity and near-net-shaping.

For the 2-C-MIM process, adjustment of the feedstock viscosity is crucial. Very low viscous binders are susceptible to binder-powder separation and difficulties during the injection moulding process. The phase separation leads to areas with high powder concentrations, which leads to sharp viscosity increase and clogging of the injection unit. On the other hand, very high viscous binders are not desired as well, as high injection pressures are required for moulding, what could bring difficulties during the process. For optimisation of the feedstock, knowledge of the flowing behaviour of the feedstock is important, especially when space holder particles are used. These particles are much larger than the metal powder particles used and their influence on the flowing behaviour is still unknown, especially if the tool comprises small channels.

The aim of the present work is to manufacture titanium parts for biomedical applications with dense and porous areas by using the 2-C-MIM technology. Costs reduction is expected in the case of large scale production, when the new investigated technique is compared to the established production methods current in use.

For the fulfilment of the challenges of this work, new binder systems which enable the incorporation of space holder particles and the replacement of the wicking method were developed. Impurity levels in the finished part were taken into consideration as well, due to the sensitivity of the titanium powder to impurity uptake. A detailed investigation of binder components and binder systems was undertaken, followed by characterisation of feedstocks with and without space holder particles regarding debinding behaviour, part dimensional accuracy after processing steps, chemical impurities, sintered microstructure and flowing behaviour of feedstock by capillary rheometry.

After choosing the most promising feedstocks, the results were transferred to 2-C-MIM by manufacturing a prototype of a spinal implant. Hereby the geometry of a commercial spinal implant has been taken as a reference, where the implant dimensions were delivered by the company Synthes. The special challenge during the injection moulding process was the use of two injection units, with feedstocks with and without space holder particles in a fully automated process. The influence of the injection pressure during the MIM process optimisation and the sintering temperature of the implants were investigated. The implants were characterised regarding their dimensional accuracy, microstructure and impurity content.

2 Theoretical background

2.1 Porous titanium as implant material

Titanium and several of its alloys have been confirmed as one of the most effective groups of traditional biomaterials and are still the materials of choice for many implant applications [1]. Titanium is taken into account implantable devices due to its corrosion resistance and biocompatibility associated with mechanical performance.

The body fluids are relative aggressive chemical media for a metallic component, what induces metal corrosion [2]. The release of metallic ions through the implant corrosion may influence the behaviour of cells, tissues and body metabolism and is therefore undesirable for an implant material.

It is claimed in the literature that titanium is relatively inert and a corrosion resistant metal because of its self-passivating behaviour based on the formation of a thin (approximately 4 nm [3]) surface oxide layer. This fact makes the material to be more inert than other metals used in the biomedical field, like 316 L stainless steel and cobalt-chromium alloys. The 316 L high grade steel, for instance, show always higher reactivity in cell culture (in-vitro tests) as well as after implantation in animals (in-vivo tests) when compared to titanium, which may be attributed to the higher corrosion level of steel in biological media [3].

For bone applications, titanium has proved to fulfil the mechanical requirements to be in contact with bone tissue, including high resistance to loading, fatigue resistance and ductility [4, 5]. There are practically no areas of internal fixation where titanium would not be a suitable material. Where a higher strength level is required than reached by commercially pure titanium, titanium alloys such as Ti-6Al-4V or Ti-6Al-7Nb can be applied.

Nevertheless, the stiffness of the material employed as bone substitution is of great importance. Implant materials which have higher stiffness prevent the needed stress being transferred to the adjacent bone, resulting in implant loosening and stress shielding [2]. This phenomenon occurs when the implant takes the load-bearing function over and avoids loading and unloading of the bone, which occurs in the natural course of body movement. As a consequence, the bone porosity around the implant increases and implant loosening takes place.

The lower modulus of titanium alloys varying from 110 to 55 GPa compared to 316 L stainless steel (210 GPa) and chromium cobalt alloys (240 GPa) [5], is a very important advantage. Nevertheless, an ideal material for bone replacement is expected to have a

modulus still better adapted to that of the bone. The bone modulus varies in the magnitude from 4 to 30 GPa, depending on type of the bone and direction of measurement.

The introduction of pores in the titanium structure would be an effective measure to adapt the elastic properties of the implant to that of the human bone. The stiffness mismatch between bone and implant, which may lead to stress-shielding, is diminished by using porous structures. By choosing the adequate porosity, mechanical properties similar to the ones of the bone can be obtained. The elastic properties of materials aimed for implant applications was suited for this purpose by adapting the porosity of the metallic structure [6-8].

In addition to the implant material, the construction of the implant device plays an important role to ensure long-term stability in the human body. It is always the desire that a stable interface between implant and bone is created, which is able to constructively react to the body physical and biological demands. There are different ways in which adhesion of the implant to the bone tissue may be achieved. These are listed below.

- Cementation: This is the case for instance of hip replacements, which have to be cemented in place using poly(methyl methacrylate) (PMMA), so that the actual interface with the bone is the PMMA material [9]. In order to do this, the bone is machined so that a thick cement mantle can be subsequently applied. The cement is prepared at the time of surgery and inserted with syringes inside the bony implant bed after a cleaning step. The implant is introduced in the still flowing cement and, after a hardening step, the cement mantle is stable and provides anchoring to the bone.

- Screw or press-fitting: This is the case, for instance, of dental implants, for which stability is achieved with a threaded root for mechanical integration [10]. Unlike the cemented variation, a direct contact between implant and bone tissue exists. The implant achieves a stable primary fixation to the bone by press fitting, and a secondary fixation of the prothesis takes place after some weeks due to osseointegration to the threads.

- Geometrical construction: The implant for lumbar disc replacement is an example where the geometrical construction of the implant plays an important role for fixation. Lumbar discs are the largest articulated non-vascularised tissue in humans, statically and dynamically extremely loaded [2]. In a healthy spine, the function of a lumbar disc is to transfer the load from one vertebra to the other and to carry the movements of the spine together with the vertebral joints. The vertebrae and the bands of the vertebral arches together with the lumbar discs protect the spine from excessive shear, torsion and extensional loads, as well as excessive forwards and backwards movements, as shown in Figure 1 (left). In some cases, lumbar conditions are associated with strong pain and the replacement of the lumbar disc is

the most adequate treatment option. There are different concepts of lumbar disc implants, under which one of them is the PLIF-implant (posterior lumbar interbody fusion), shown in Figure 1 (right). Those implants are named after the implantation method and show often a structure like a cage, which is designed to promote the ingrowth of bone tissue into the implant. To improve this ingrowth further, the inside part of the implant may be filled with autologous bone tissue.
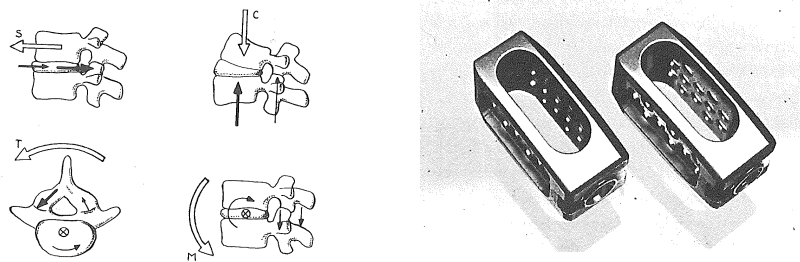
Figure 1: Left: Schematic drawing showing how the vertebrae and the lumbar discs provide resistance against: shear (S), compression (C), torsion (T) and inflexion (M). Right: PLIF-implants for lumbar disc replacement. [2]

- Open porosity on implant surface: Another alternative to promote bone ingrowth into an implant is to modify the implant surface and create a meshwork of interconnected pores in the structure. Examples of established products available which rely on open porosity for osseointegration are porous hip replacement cups and knee protheses of the company Zimmer [11]. The pores create a mechanical interlock between implant and bone. It is reported that pores in the range of 350-500 μm [10] are preferentially suitable for this purpose for titanium implants. In a *in vivo* study [12], porous blocks of titanium with pore sizes in the range of 300-500 μm and porosity in the 40-60% range delivered better results as titanium fibre mesh cylinders with pore size from 50 to 450 μm with the same porosity. Another *in vivo* study [13] showed that pores sizes with minimum 100 μm allow bone ingrowth into ceramic implants, but pore sizes larger than 150 μm are required for formation of osteon (cylindrical fundamental structures of the bone). For cobalt-based alloy implants, pore sizes in the range of 50 to 400 μm provided the maximum fixation strength in the shortest time period in implantation in dog bones [14]. It is also reported that pore sizes of about 450 μm are required for the ingrowth of blood vessels and 100 μm is the minimum pore size for the ingrowth of connective tissue cells like osteoblasts, as shown in Figure 2 [2].
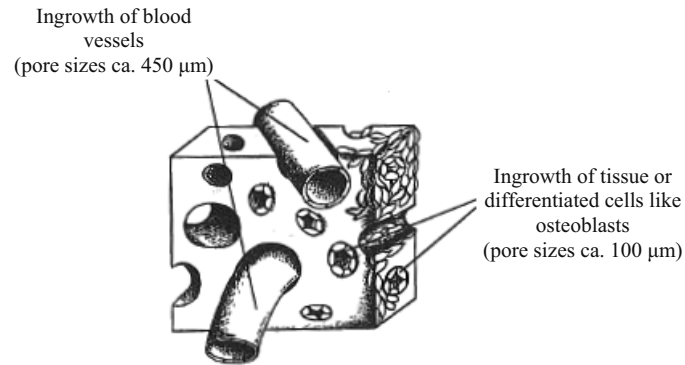
Figure 2: Schematic drawing of blood vessels and tissue ingrowth into the implant structure [2].

Besides improving mechanical interlocking between bone and implant, the use of porous structures brings with it another advantage. Adaptation of the elastic modulus of the material so that it is closer to that of the bone is possible by choosing the adequate implant porosity, as it was mentioned previously.

For load-bearing applications, it is often the case that a wholly porous structure does not fulfil the mechanical requirements and a structure with a porous coating on a dense substrate or with a gradient in porosity is needed [15]. In this case, the dense metallic part is responsible for the mechanical stability of the implant.

2.2 Fabrication methods of porous metals

There are different ways of production of porous metals. The main methods described in the literature are listed below [16, 17]:

1) Gas in the metal melt: The technique consists in bubbling a gas into the metal melt and allowing the material to solidify. Special viscosity raising agents are needed in order to stabilise the foam. A variation of the method consists in dissolving hydrogen gas in the liquid metal under pressure and solidifying the material, using the eutectic point of the mixture to deliver hydrogen-filled pores.

2) Gas-releasing foaming agents: A foaming agent (usually TiH_2) is added to the metal melt and begins to decompose. Large volumes of gas are formed and viscosity raising agents are needed as well. Foaming agents may also be added to the metal powder. The mixture is then compacted and the material is heated up inside a mould with the desired final geometry.

3) <u>Entrapped gas expansion</u>: The metal powder is sealed in a canister which is subsequently evacuated, filled with argon and consolidated to a high relative density by hot isostatic pressing (HIP), causing a reduction of pore sizes and a strong pressure increase. A rolling step is introduced to refine the structure and create a more uniform distribution of small pores. The final step is the expansion of the entrapped gas by heating up the material to temperatures where creep processes become possible.

4) <u>Investment casting using polymer material precursor as template</u>: An open-cell polymer foam template is selected. It is coated with a mould casting ceramic powder slurry, which is dried and the mould is heated up to harden the casting material and decompose the polymer material. The mould is filled with liquid metal and allowed to cool down. After removal of the mould material, the metal foam is left behind. Metal powder slurries can also be used, which are subsequently sintered.

5) <u>Metal deposition on cellular performs</u>: An open-cell polymer precursor, previously shaped in the desired form, is placed in a chemical vapour phase deposition (CVD) reactor and after the desired metal layer has been deposited, the metal-coated polymer is burnt out. This results in a cellular metal structure with hollow ligaments. The ligaments are densified in a subsequent sintering step. The process allows the production of foams with the lowest relative density available (0,02-0,05).

6) <u>Metal powder or fibre sintering</u>: Powders or fibres are compacted together and subsequently sintered. The sintering process is stopped in an early stage after formation of sintering necks. Pore size and shape are dictated by powder / fibre size and shape. Hollow spheres made by different methods (like vapour deposition of the metal onto polymer spheres or suspension coating of spherical polymer templates followed by debinding and sintering) may be used as well.

7) <u>Plasma spraying</u>: Powder for coating is injected in a plasma gas stream produced by an electric arc. The powder is accelerated to a high speed, melted and impacted onto a substrate. Porous coatings with varying degrees of porosity can be created by adjusting spraying parameters.

8) <u>Combustion synthesis</u>: The reactant powders are mixed and pressed. Metal powder fusion is obtained by an extremely rapid self-sustaining exothermic reaction driven by the large heat released by the synthesis. The reaction can be instigated through different methods.

9) <u>Rapid prototyping</u>: The process, in form of three-dimensional printing (3DP), is used to obtain three dimensional parts from a computer model. It consists in a layered printing process in which the information for each layer is obtained by applying a slicing algorithm

to the computer model of the part. Parts are created inside a cavity that contain a powder bed supported by a moving piston by a layer thickness and filling the resulting gap with a thin distribution of powder. The powder particles are joined together by a binder material. In this way, a ceramic shell is created without the need of a wax pattern and one step of the standard lost-wax casting process is saved. Selective laser melting (SLM) and selective electron beam melting (EBM) are also rapid prototyping methods, in which the parts are generated by applying powder material layers in a printing process and selectively scanning the area with a laser or electron beam in order to melt the powder layer and create bonds between the layers. The latter processes do not use a binder material and are therefore especially suitable for oxidation sensitive powders as titanium.

10) Electrodischarge compaction: Involves the application of an external current to assist powder consolidation. Also known as spark plasma sintering (SPS), under other denominations.

11) Space holder method (SHM): A space holder material is mixed to the metal powder and the mixture is pressed together. After removal of the space holder, pores are left in the metallic structure. After sintering, porous parts with defined pore shapes, sizes and distributions are formed.

The processing methods 1 and 2 usually result in random distribution of pore sizes, location and shapes. The use of the melt gas injection method for the production of porous titanium and titanium alloys is also very unlikely to be successful, due to the strong tendency of titanium to react with oxygen [18]. The techniques involving foaming agents are critical for titanium materials as well. Interstitial solution of hydrogen, as well as oxygen, which are introduced during foaming, embrittles the titanium matrix. Furthermore, the decomposition of TiH_2 occurs too fast in metals with melting points higher than that of aluminium [16]. Although other metals are under investigation, methods 1-2 are nowadays restricted to aluminium and aluminium alloys production, due to the low melting temperature, which fits with the decomposition of TiH_2 and the tendency of the aluminium material to not excessively oxidize.

The method of HIPing by gas entrapment (3) is suitable for the fabrication of porous titanium structures but here the high costs of the HIP-process are an important issue [16]. The additional steps for homogenisation of pore distribution may also contribute significantly for economical inviability of the process. The fabrication of porous Ti-6Al-4V [19] and titanium

[20] materials were obtained by this method, where different heating cycles after hipping were investigated in order to study foaming kinetics.

Methods 1-3 generate a closed-cell porosity. Although a closed porosity allows matching of mechanical properties of the implant to bone-like, it does not allow much bone ingrowth. The methods which deliver open-cell structures (4-11) are more attractive for implant applications with surrounding bone tissue.

The casting method using polymer precursors (4) is also named replication and was already investigated for the production of porous titanium and titanium alloy structures with powder slurries [17]. It is reported that flaws in the titanium structure were present and were corrected after a second impregnation step. It seems that the technique is laborious when more mechanically stable structures need to be produced. The production of titanium foams by the replication method was investigated by another group as well, where the cost factor was raised as a concern for the commercial feasibility of the process [21].

Although the CVD process (5) is also suitable for titanium [16], the method involves many processing steps, which contributes to increasing of processing costs. The fatigue strength of the final product is also a concerning step [17]. The process has been employed for the fabrication of tantalum biomedical foams with a carbon core, which are commercialised under the trade name Hedrocel by the company Implex [22].

The sintering of metal powder (6) has been studied for the production of porous titanium samples for implant applications [17]. Although porosities in the range of 30-50 % may be achieved, the mechanical properties of sintered metal powders are a concern. Regions of poor bonding after sintering have been also reported. Single spheres may lose from the matrix due to the notch effect produced by the sintering necks, what makes the material prone to crack propagation. When metal fibres are used to produce a porous coating, they must be compacted to a form prior to sintering, what is not necessarily the case if powders are used. In another study, the notch sensitivity was reported to be diminished by the addition of Si to assist liquid-phase sintering [8].

Although titanium implants with increased surface roughness may be fabricated by plasma spraying (7), the method involves at least a two-step processing route, which increases the cost of the product [17]. Problems of contamination and the presence of impurity phases may also be an issue. Rough coatings were obtained by plasma spraying TiH_2 powder, where improved bone-implant interface strength was confirmed by *in-vivo* tests [23]. In another study [24], where commercially pure titanium powder was sprayed, a gradual change in porosity was achieved, so that the elastic properties of the material would be more adapted to

11

that of the bone. Plasma spraying is an established surface modification process already employed for hip and knee protheses available in the market.

Highly pure resulting foams are obtained with the combustion synthesis method (8), due to the expulsion of volatile impurities during the process. The final microstructure of the part is controlled by various processing parameters such as reactant particle size, use of binder material and compaction pressure [25]. The combustion synthesis method involves the reaction between the starting powder materials and is a established method for the production of NiTi alloys [26, 27]. Hereby the pore size, pore form, overall porosity and chemical homogeneity are difficult to control due to the fast evolution of the exothermic reaction between the starting materials.

The rapid prototyping method (9) was investigated for the production of porous implants and it is claimed that parts with controlled size, shape and distribution of porosity as well as functionally graded parts were produced [17]. Although the method allows the production of ceramic shells without the need of a wax pattern, it is still a casting method, with the disadvantages brought with it, such as an individual ceramic shell for each casting. There are also dimensional limitations [28], regarding the minimum strength of the ceramic unit to withstand handling, the removal of powder from the ceramic and the pressure required to fill the small features during casting. The production of Ti-6Al-4V porous structures by selective electron beam melting (EBM) [29, 30] and the production of a porous interbody fusion cage for use as a spinal implant by selective laser melting (SLM) [31] were reported. Hip, knee, shoulder and spinal implants produced by the EBM method are commercialised by the company Arcam [32].

It is claimed that the electrodischarge powder compaction (10) method is suitable for the production of titanium implants with a functional gradient in porosity [17]. In a study for the fabrication of titanium dental implants [33], the sample was fabricated using a smooth surface cap with a beaded porous body. Although compressive and torque strength were reported to be adequate for the application, no fatigue tests were performed, which is a concern when porous layers in contact with a solid substrate are in use. In another study [34], samples with a relative dense core and a porous outer layer were produced, but lack of consistent internal integrity (voids) was reported. Moreover, final part complexity is limited, as the powder must be compacted in a form prior to the electro-discharge.

The space holder method (11) is a method for producing porous implants with or without a gradient in porosity by powder metallurgy. By this method, suitable space holder particles are mixed with metal powder and, after removal of the space holder and sintering of the part, a

porous structure is formed. Pore sizes and total porosities up to 80% with homogeneous pore distribution and pore sizes from 0,1 to 2,0 mm may be achieved with this method [35]. Other authors investigated the fabrication of porous magnesium [36] and porous aluminium [37] by using the same principle.

2.3 Metal Injection Moulding (MIM)

The Powder Injection Moulding (PIM) is a technique derived from the conventional plastics injection moulding, in which the advantage of the complex shaping is transferred to the production of parts moulded with a mixture of binder and powder materials. This technique is suitable either for ceramic (Ceramic Injection Molding – CIM) as well as for metal powders (Metal Injection Moulding - MIM). Today, the process is mainly employed for the production of complex shaped parts, where high precision and productivity play a very important role.

The main process limitation is the component size. The removal of the binder material is more difficult in larger parts, so that small parts are preferred. A typical steel component fabricated by PIM is a trigger for a sporting shotgun with a final weight of 40 g [38]. Direct competitors of the process are investment casting techniques or die compaction, if more simple geometries are to be produced.

The MIM technique was developed at the beginning of the 1970s and has since then proved to be a promising process for the mass production of small and complex shaped metal parts [38]. The process is shown schematically in Figure 3:
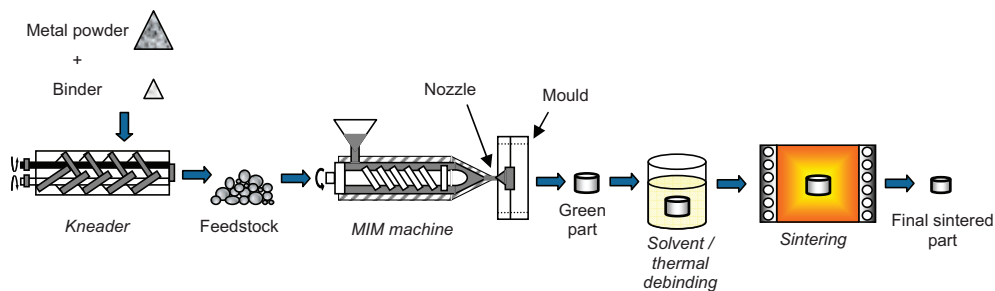
Figure 3: MIM-technique.

The first step of the process is the fabrication of the feedstock to be injected. The chosen powder and binder are homogenised in a kneading machine at a temperature above the melting point of the binder system used. A detailed description of the state of the art of binder systems is given later in chapter 2.5. Normally, at least two components are required in order to achieve a compromise between suitable flowing behaviour, debinding availability and

13

mechanical stability. The resulting mass is granulated after cooling down, so that the feedstock is produced. As a second step, a powder injection moulding machine is used to inject the feedstock, so that the parts with the desired shape are formed. These parts are named green parts. The extraction of the first binder component takes place at the third step of the process, in which a thermal or solvent debinding is employed. After this step, interconnected pores are formed and the remaining binder assures the mechanical stability of the partly debinded part. As a last step, the rest of binder is thermally removed, where the binder-free sample is named brown part. At the final stage of thermal debinding, binder material is only present at the contact points of the powder particles and capillary forces hold the particles together until sintering starts [39].

The PIM process is a complex one and a successful production depends on several factors. The first one is the choice of starting materials. The powders used are normally small, to aid sintering and to provide homogeneous filling of small cavities. High packing densities are desired, so that homogeneous sintering shrinkage with low shrinkage values and high sintering densities are obtained. The typical size range of the particles is reported to be from 0,1 to 20 [38] or 10 μm in average [40]. Particles with near spherical shapes are preferentially used, to promote flow during injection.

The binder material is normally wax and polymer-based, but other variations are possible. A very wide range of binder systems have been developed so far [41]. The binder system should be specifically chosen for the powder in use and its characteristics are one of the main factors which determine the success of the subsequent steps. Hereby, the amount of binder in the feedstock plays an important role. The optimal amount of binder is the one in which sufficient lubrication exists between the powder particles, so that the feedstock allows itself to be injected without major problems. It is believed that at this point all voids between particles are filled with binder material [38]. If insufficient binder is in the mixture, voids are formed and the viscosity of the feedstock is too high for it to be injected. On the other hand, if too much binder is used, problems during debinding may occur and a homogeneous sintering shrinkage is impaired.

The injection process itself is very complex as well, as many parameters may be varied and operator experience plays an important role for a successful production of the parts [38]. The feedstock is injection moulded in the desired shape by heating in the mould machine and hot ramming it under pressure into the tool cavity. Some of the process parameters can be distinguished as the most important ones, such as the temperatures inside the barrel, the injection temperature, the mould temperature, the charging volume, the injection volume flow

rate, the injection pressure, the holding pressure and holding time. A special hardened screw for powder injection moulding inside the injection unit in the machine promotes the transport of the mass with a defined velocity to the injection nozzle. Figure 4 shows the stages of the moulding operation. In plastication, the screw rotates and transports molten feedstock up to the nozzle. In the moulding stage, the screw acts as a plunger with a rapid forward motion that forces feedstock flow through the nozzle as a check ring seals against the screw tip.

Inside the barrel, there are four heating zones, which can be independently regulated. The fifth heating zone is at the injection nozzle, where the injection temperature is defined. The charging volume is defined by the position of the screw inside the injection unit. The injection volume flow rate is defined by the velocity of the displacement of the screw, which can be stepwise regulated. When the defined charging volume is achieved, the mass is pressured with the defined holding pressure and time. The holding pressure can be also stepwise regulated, where up to ten subsequent holding pressures with different holding intervals can be defined. Its main objective is to compensate the shrinkage of the injected part while cooling down. Another important parameter is the mould temperature. It is externally regulated by a circulating oil thermostat, where a direct control of the mould temperature is possible with a thermocouple element.
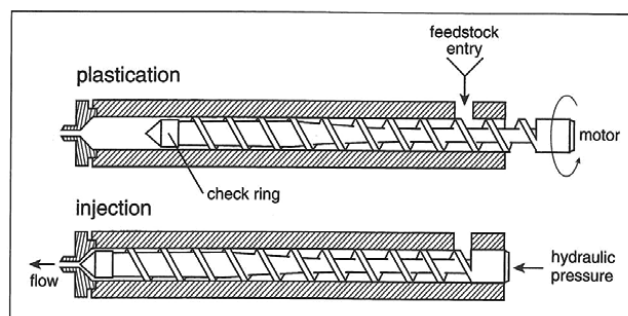
Figure 4: States of the screw in the barrel relating to plastication and injection states [38].

2.4 2-Component-MIM

In the plastics industry, different materials are often combined so that the optimal properties of each material can be used in the finished part. The technologies involved are much specialised and specially constructed injection moulding machines are necessary, in which at least two injection units are required. Malloy [42] generally named the process as „Co-Injection Moulding", in which at least two subcategories can be differentiated, as described below.

A toothbrush and a computer keypad are examples of parts which can be produced with the „2-Component-Injection Moulding" or „2-Colour-Injection Moulding" techniques. The process is essentially the injection of one component after the other, in which part of the mould is moved or turned after the injection of the first component. The second component is subsequently injected over the previously injected part.

Another subcategory of the „Co-Injection" process is the „Sandwich-Injection-Moulding". By this method, the first mass is injected in the mould cavity by an injection unit, so that an outer skin is formed. Immediately afterwards the core of the part is formed by the injection of the second mass by another injection unit. Both masses are hereby injected through a common valve, which controls the separation of both materials.

Another author [43] names the combination of materials by injection moulding as „Inmoulding" or again as „2-Component Moulding". Hereby many subcategories are cited: two-colour, paint coating, decorating, inmould assemble, two-laminate, two colour rotary, two colour shuttle, double daylight, inmould labelling, in which overmoulding is the basic principle. Hereby is the „Insert Moulding" process described, in which pins, studs, connecting parts or other components are inserted in the mould cavity before the injection, in order to spare post processing procedures in the finished part.

In summary, the denominations of the different techniques overlap in the literature and there is no general agreement between the authors about it. Also different denominations may be found in other sources.

Some of the techniques described above for the combination of plastic materials were transferred to PIM recently. In the literature, three main methods are described for the combination of different powder materials via injection moulding: the "Overmoulding", the "Sequential Injection Moulding" or "Insertion Injection Moulding" and the "Co-injection Moulding" or "Sandwich Injection Moulding". "2-Component-MIM" (2-C-MIM) is the general denomination for the aforementioned techniques, when metal powders are used.

Overmoulding

By the "Overmoulding" method, a powder injection moulding machine with two injection moulding units and a mould with a rotation device is used. As a first step of the process, a green part is produced in the mould cavity. The mould then opens and the second working position is achieved after a mould rotation of 180°. After closing of the mould, the first green part is in the second working position for the injection of the second component, as shown in Figure 5. The method was used for the investigation of the combination of stainless steel and carbon steel [44, 45]. Based on dilatometry studies of the sintering shrinkage, the investigated material systems enabled the production of defect-free parts.
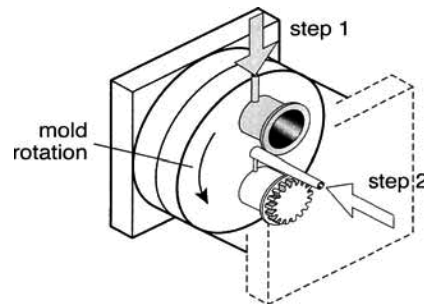
Figure 5: Schematic illustration of the *overmoulding* PIM-process [45].

Another variation of the "Overmoulding" technique is when only part of the mould is moved or pulled after the injection of the first component. This principle was used in a study where different porcelain feedstocks were combined [46]. But, in this case, delamination problems occurred already in the green state and sintering defects such as cracks were also present at the interface between the materials. The technique was also studied to combine ZrO_2 and steel feedstocks [47], where good adherence of the materials was achieved after dilatometric studies. Another study involved the production of parts composed of different steel feedstocks [48]. Hereby the mould also allowed the injection of the feedstocks at the same time (additionally to overmoulding). Both injection variations were studied in that work and problems related to the joint between the sintered materials were reported.

Sequential Injection Moulding or Insertion Injection Moulding

By the "Sequential Injection Moulding" or "Insertion Injection Moulding" process, a pre-injected part is placed inside the mould and a second feedstock is injected in the remaining

cavity. The combination of masses with and without space holder for the fabrication of parts with a gradient in porosity was investigated by Nishiyabu et al. [49]. Titanium and steel parts with a gradient in porosity (gradation 0-30-65 %) with pore sizes from 10 until 180 μm and PMMA as the space holder were produced. The disadvantage of the "Insertion Injection Moulding" is the need of additional steps in the process, as the insertion of the pre-injected green part in the mould for instance, what leads to longer production cycles. The problem may be overcome by the use of more machines in sequence with robot systems.

Co-Injection Moulding or Sandwich-Injection Moulding

By the "Co-Injection Moulding" or "Sandwich-Injection Moulding", an enclosed core of material is introduced into an outer skin. Firstly the skin material is injected by the vertical injection unit into the moulding cavity, followed by the injection of the core material by the horizontal injection unit. Then a second injection of the skin material ends the cycle, so that the first component completely encapsulates the second component. In this way, the core material is unable to be at the surface of the moulded part and the sprue system is cleared for the subsequent shot. As the masses are injected very rapidly after each other, the difference in temperature between the injected materials is relatively lower as compared to the aforementioned processes, so that interface tension is less likely to happen. The cycle time is considerably lower as well. This process was investigated by some research groups. Nishiyabu et al. [49] produced parts with a gradient in porosity with both steel and titanium powders with particle sizes of respectively smaller than 9 and 24 μm and PMMA space holder particles from 10 until 180 μm. The sintered parts with a gradient in porosity are shown. Another group [50, 51] investigated the combination of different steel materials. Figure 6 shows a green part produced by "Sandwich-Injection Moulding" with a outer skin of 316-L stainless steel material (particle size ≤ 0.5 μm) and a core of carbonyl iron (particle size ≤ 1 μm). In the skin feedstock, 5% of alumina particulate phase has been introduced to confer improved wear resistance on the surface. The production of part-sintered parts without delamination is reported, but fully sintered parts are not shown in the cited work.
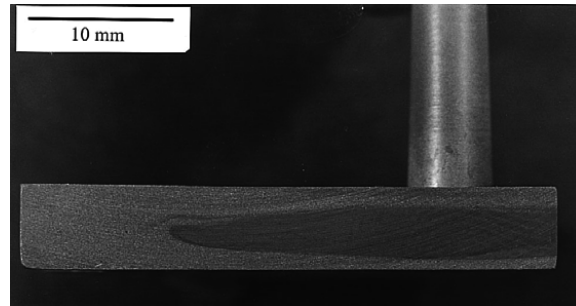
Figure 6: A green part which was produced by *sandwich-injection moulding* (core: carbonyl iron, outer skin: 316 L stainless steel and alumina) [51].

In the same study, a computer model was developed for "Sandwich-Injection Moulding" process for the system 316 L with aluminium oxide and carbon steel with the particle sizes mentioned previously. According to the model, the viscosity of the feedstock influences the ratio of the thickness between the outer skin and the core. It is mentioned that the powder fraction, the powder particle size and the backbone polymer can be specific selected to adjust the material to the desired ratio of the core and outer skin.

2-Component-MIM with space holder particles

The 2-C-MIM has been extensively studied in the recent years and its potential for the combination of different feedstocks has been proved. The choice of feedstocks and materials feasible for combination is a crucial step, so that delamination and sintering defects are avoided.

The combination of the space holder method with the 2-C-MIM process makes the production of near-net-shape parts with a gradient in porosity possible, when feedstocks with and without space holder are combined. For this purpose, a special 2-C-MIM machine with two injection units and an automated mould are required. Figure 7 shows the process steps of 2-C-MIM in combination with the SHM. The first step consists in producing the feedstocks, one with and another without space holder particles. The powder material and the binder are homogenised in a kneader. The green parts are injection moulded and the space holder removed after the first stage of debinding. The parts are then thermally debinded and sintered.

1st step: homogenisation of the materials

Metal powder -Ti

+

(Space holder NaCl)

+

Binder

Kneader

Feedstock without
space holder

Feedstock with

space holder

2nd step: injection of the feedstocks

Feedstock with

space holder

Feedstock

without space

holder

Horizontal

unit

Nozzles

Vertical unit

Mould

2-C-MIM machine

2-component

green part

3rd step: Solvent debinding and removal of space holder

2-component

green part

Immersion in

solvent

Immersion in

water

2-component

part

4th step: Sintering

2-component

part

Sintering oven

2-component

part

Figure 7: Schematic drawing of the 2-C-MIM process in combination with the space holder method.

2.5 MIM feedstocks

The MIM feedstock is the raw material of the MIM process. Its composition and processing procedure are therefore main factors leading to a successful production. In the next sections, an overview about the main issues concerning feedstocks; namely binder systems, debinding methods, solids content and flowing behaviour, are discussed.

2.5.1 Binder systems

The binder is a crucial constituent for the shaping of the part during the MIM-process, as it provides the flowability of the feedstock and a homogeneous distribution of the powder particles in the finished part. Moreover, the binder ensures the mechanical stability of the part until the beginning of sintering.

Even though the binder is not present in a finished sintered MIM-part, it can influence its final characteristics. The homogeneity, the final density and the chemical impurities in a finished MIM-part are examples of characteristics which can be influenced by the binder system used. As a consequence, the mechanical properties of the finished sintered part can be influenced, among others. Therefore, the choice of the binder system plays an important role in the quality of a MIM-part.

The most binder systems are composed of several components, in which the major features of the feedstock can be influenced by the addition of even small amounts of specific additives. In that way, a feedstock can be specially tailored for a specific application.

There are at least five different types of binder systems discussed in the literature, which are listed below [38]:

1. Thermosetting systems
2. Water-based systems
3. Gelatination systems
4. Inorganic systems
5. Thermoplastic systems

Thermosetting polymers form cross-links among the molecules and become permanent rigid on heating. The recycling of the feedstock is not possible and reactions are generally slow, so that the time required to form a stable green part is relatively long as compared to feedstocks with other binder systems. The advantage of a thermosetting structure is the higher green

strength of the injected parts, but debinding times are normally longer. Although it is reported the investigation of epoxy resin and thermosets based on polycarbosilanes [52] as binder materials for PIM, the use of thermosetting compounds has been generally unsuccessful in industry, with only few exceptions [38].

Feedstocks with water-based systems solidify by a freezing process, where a slurry of powder and water is frozen in the die [38]. Simple freezing binder systems are composed of soap and water or starch and water. The water is removed by vacuum sublimation, what reduces the risk of crack formation. The advantage of the method is that the production of relative large parts is possible, but specially constructed MIM machines with special freezing moulds are required for operation. It is described in the literature that the process was developed by the company CPS - Ceramic Process Systems in USA, which validated the suitability of the method for its production cycle [41]. Despite of some patents [52], it is described that the process was put in operation in Europe only by the company IMPAC in France, in a cooperation work between CPS and Vallourec [41]. There are no other indications about a broader use in industry.

In gelatination systems, a single large molecule that extends throughout the sample is formed [38]. Certain polysaccharides, polyaminoacids and synthetic polymers interact with water molecules to form gels. The advantage of the method is that the water can be removed easily in a conventional oven or by microwave drying and the use of water does not involve an anisotropic thermal expansion which may be associated with polymeric binder systems [41]. The limitations are low strength before drying, which hinders automatic ejection of the green part from the mould.

Inorganic compounds are a variation of the water-based system, where a high concentration of sodium or ethyl silicate is added to the solution [38]. Inorganic silicate glass gels are initiated by exposing the solution to freezing temperatures, carbon dioxide, or an organic ester. The strong glass structures impart high green strength, but silica remains in the component after drying. The material to be sintered must be compatible with this contamination.

Even though many variations are possible, the thermoplastic systems are the preferred ones in industry [38]. Normally a thermoplastic-based binder system is composed of a major constituent of oil or wax, a polymer material and an additive, which can be used for viscosity control, wetting of the powder particles or debinding assistance, for instance. In many cases, several constituents may be present and a component takes over more than one function in the system. Generally at least two components are present in a binder system, in which the major constituent (the first component) is removed in a first debinding step and the other one (the

second component) holds the powder particles together and ensures the part stability until the beginning of sintering.

The first and second components of the binder system are often present in roughly equal proportions. Nevertheless, contents of the first binder content in the range of 20 to 80 Vol.% are described in the literature, and even at low contents in the range of 20 to 30 Vol.% are described to be enough to assure interconnectivity of this component throughout the green part [38]. This is necessary for allowing binder removal at the first stage of debinding and a sufficient porosity of the part for the escape of decomposition products during thermal debinding.

The components must be at least partially soluble in each other, so that the mixture is homogeneous enough to be processed and to ensure the part stability. On the other hand, it is reported that the solubility of the components in each other can not be so high so that the molecules of the first component remain trapped in the system and can not be removed during the first debinding step [53]. An indication of the chemical interaction of polymer materials and its solubility in each other is the change in phase transition temperatures (such as melting temperature) of the component in the mixture as compared to the single component [54, 55]. Those are indicatives of the intersolubility of the binder components.

Additive materials like stearic acid, oleic acid or vegetable oil are commonly used in PIM, being stearic acid the most widely used [38]. Those materials preferentially interact with the surface of the powder particles and reduce the contact angle by lowering the surface energy of the binder-powder interface. In this way, the viscosity of the feedstock may be reduced and higher powder loadings are allowed to be reached as compared to additive-free feedstocks.

As waxes and thermoplastic polymers are the preferred materials used in PIM, a brief overview about these components is given below. An overview of the additive stearic acid follows the text.

Waxes

Waxes are normally composed of not only one component, they are rather complex mixtures. Functional groups like carboxyls, alcohols, esters, ketones and amides are found in waxes [56]. Waxes can be of natural or synthetical basis. Natural waxes can be used as binder components for PIM [38], like bee or carnauba wax. These waxes are composed of hydrocarbons with aliphatic esters, carboxylic acid esters are free alcohols. Although their properties are suitable for the use in the MIM-process, waxes of natural basis are generally

23

more expensive nowadays than synthetic waxes and, as a natural raw material, material properties and their availability are subjected to oscillations.

The use of waxes obtained from crude petroleum in industry has been increasing continuously for two reasons: the increasing demand for lubricating oil with low pour points and the large proportion of paraffinic crudes in total crude oil production that have to be dewaxed for the production of lubricating oils [56]. This development has increased the need to find more industrial applications for petroleum waxes, which are by-products of lubrication refineries. Petroleum waxes are classified into two main branches: macrocrystalline waxes (paraffin waxes) and microcrystalline waxes (microwaxes). This classification depends on the natural occurrence and crystallinity of the material. Paraffin waxes originate from light and middle lubricating oil cuts of vacuum distillation. Microwaxes are obtained from residues from vacuum distillation and from sediments of paraffinic crude oil.

Paraffin waxes consist predominantly of mixtures of straight chain alkanes and the molar mass range depends on the boiling point range of the lubricating oil distillate from which they are obtained. Paraffin waxes are generally insoluble in water and soluble in ketones, chlorohydrocarbons, petroleum spirit, benzene, toluene [56] and in n-hydrocarbons as hexane and heptane [57]. The solubility decreases markedly with increasing molar mass of the wax, whereas its melting point increases with increasing molar mass. Paraffin waxes are normally unreactive under normal conditions, but oxidation may occur in presence of oxygen and catalytically active metals. They have a C-number distribution of n-alkanes from 18 to 45 [56], but even the lower boiling point fractions of petroleum contain varying amounts of other hydrocarbons, namely cycloalkanes and aromatic compounds, which could be present in paraffin wax as well [58]. The main characteristics and chemical composition of various paraffin waxes are shown in Table 1.

Table 1: Main characteristics and chemical composition determined by mass spectrometry of various paraffin waxes [58]. Differences in materials A-F originating from different distillation cuts from crude oil and refining processes.

Characteristics and composition	A	B	C	D	E	F
Melting point, °C	50.7	52.9	57.3	57.5	58.7	62.8
Oil content (ASTM), wt-%	<0.2	0.3	<0.2	<0.2	<0.2	0.5
n-Alkanes, wt-%	75.5	94.0	86.4	81.9	82.2	66.5
Branched alkanes, wt-%	13.5	2.6	6.3	10.4	8.2	17.9
Monocycloalkanes, wt-%	10.2	3.4	7.1	7.4	9.0	13.4
Polycycloalkanes, wt-%	0.6	0.0	0.1	0.3	0.5	1.9
Monocycloaromatics, wt-%	0.2	0.0	traces	0.0	0.1	0.3
Aromatic cycloalkanes	0.0	0.0	0.0	0.0	0.0	traces

Microwaxes are, on the other hand, more reactive than paraffin waxes because of the higher concentration of complex branched hydrocarbons with tertiary and quaternary carbon atoms [56]. Their C-C bonds are not very thermally stable on prolonged heating.

Another type of synthetic waxes, which is not coming from oil distillation, is polyethylene wax. High-pressure polyethylene waxes are produced, like high-pressure polyethylene plastic, at elevated pressures and temperatures in the presence of radical formers. The process will be described in detail in the next section. The difference between polyethylene plastics and polyethylene waxes lies on the molar mass. Polyethylene waxes have molar masses considerably lower than that of plastics. The molar mass range is adjusted during polymerisation by addition of regulators. The *Deutsche Gesellschaft für Fettwissenschaft* (DGF, German Association for Fat Science) definition of wax gives the approximate boundary of ca. 37,000 g/mol (weight average molecular mass $\overline{M}_w$) for the highest molecular mass for waxes. High-pressure polyethylene waxes with molar masses between 3,000 and 20,000g/mol dominate the market. Like other waxes, they also dissolve in nonpolar solvents (aliphatic, aromatic and chlorinated hydrocarbons) on heating.

Beyond the natural and synthetic waxes, there is the intermediate group of partially synthetic waxes [56]. If natural waxes or wax like materials are modified by chemical reactions such as estearification, amidation or neutralisation of acidic waxes, partially synthetic waxes are obtained. The group of amid waxes fall into this classification. This group consists of reaction products of fatty acids with ammonia, amines and diamines. One of the waxes which fall in this category and is used as a lubricant in the powder metallurgy industry is n,n'-1,2-ethanediylbis-octadecamide, which is an amide wax commercialised under the names of Plastflow, Synthewax or Wax C [59]. Its molecular structure is shown in Figure 8.

$$CH_3 - (CH_2)_{16} - \overset{\overset{\displaystyle O}{\|}}{C} - NH - CH_2 - CH_2 - NH - \overset{\overset{\displaystyle O}{\|}}{C} - (CH_2)_{16} - CH_3$$
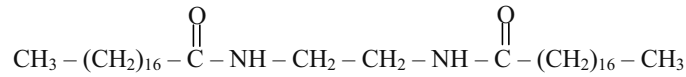
Figure 8: Molecular structure of n,n'-1,2-ethanediylbis-Octadecamide [59], which is used as lubricant in the powder metallurgy industry under the trade name Wax C, Synthewax or Plastflow.

Thermoplastics

Thermoplastics is the generic denomination for plastics which yield solid materials by cooling of a polymer melt (a physical process) and soften while being heated, in a reversible shaping process [60]. Thermoplastic materials such as polyethylene, polypropylene or polybutadiene-1 do not contain oxygen in their chemical structure and are named polyolefins [61].

Polyethylene is the most widely plastic material used worldwide and is derived from the polymerisation of ethylene [61]. Its molecular structure is shown in Figure 9, where the typical $\overline{M}_w$ is in the range of 130,000 to 200,000 g/mol.

$$\begin{bmatrix} \overset{\displaystyle H}{\underset{\displaystyle H}{\overset{|}{\underset{|}{-C}}}} & \overset{\displaystyle H}{\underset{\displaystyle H}{\overset{|}{\underset{|}{-C-}}}} \end{bmatrix}$$
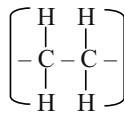
Figure 9: Molecular structure of polyethylene. n = 4600-7100

Despite ethylene's simple structure, the field of polyethylene is a complex one with a very wide range of types and many different manufacturing processes. Polyethylene derives from the polymerisation of ethylene and is classified into several categories, based mostly on its density and molecular branching. Low-density polyethylene (LDPE) has a random long-branching structure, with branches on branches. The molecular mass distribution (MMD) is moderately broad. Linear low-density polyethylene (LLDPE) has branching of uniform length which is randomly distributed along the chain, with fairly narrow MMD. High-density polyethylene (HDPE) is essentially free of both long and short branching. The MMD is typically of medium width. The branching of the molecules influences the crystallisation process, as the side branches are excluded from the crystalline region because their geometry is too different from that of the main chains which form the crystalline lamellae. That is the reason why the branched molecules have lower densities than the branching-free materials. The measurement of the density of the material is a means of determining its degree of

26

crystallinity. The different molecular structures and the lamellar crystal of polyetyhlene are shown in Figure 10.
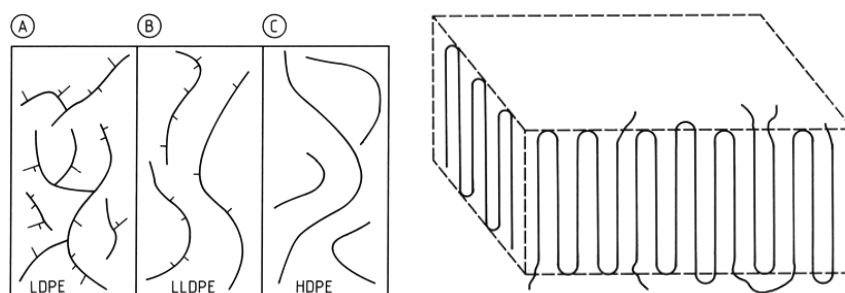
Figure 10: Left: Schematic molecular structure: (A) Low-density polyethylene, (B) Linear low-density polyethylene, (C) High-density polyethylene. Right: Folded chain lamellar crystal of polyethylene. [61]

Polyethylene manufacturing processes are usually categorised as high-pressure and low-pressure operations [61].

The high-pressure process results in the low-density materials and was the first way of synthesising polyethylene ever discovered back in the 1930s. The polymers made this way, by using free-radical initiators, are partially crystalline and densities in the range 0,91 - 0,92 g/cm^3 are obtained. A completely crystalline polyethylene material would have the density of 1,0 g/cm^3, but the lower densities obtained are due to the branching of the molecule, produced by side reactions at high temperatures, typically around 220°C. The pressure may vary from 150-200 MPa in an autoclave or 200-300 MPa in a tubular reactor.

The low-pressure variation, discovered in the 1950s, uses catalysts which allow the production of high-density polyethylene. The polymers made this way are more crystalline and have densities in the range of 0,96 g/cm^3. The reaction conditions are around 1,0 MPa pressure and temperature in the range of 80-90°C in an autoclave process and 3-4 MPa and 100°C in a loop-reactor process. The catalysts employed are named coordination catalysts and allow the production of essentially linear polyethylene at low pressure and temperature. The most employed catalysts of this category are the Philips and the Ziegler-Natta catalysts. Metallocene catalysts were latter developed for improvements of the MMDs obtained.

Polyethylene does not dissolve in any solvent at room temperature, it only dissolves above its melting point in aromatic and chlorinated hydrocarbons. Although LDPE and LLDPE do not dissolve at room temperature, they may swell in certain solvents with deterioration in mechanical strength [61].

27

Additives

There are many additives which may be used in PIM industry. Even a binder solvent may be added to the mixture in order to decrease viscosity. Silicone oil may also be used to enhance lubrication. Although many additives are possible, stearic acid is the one most widely used in powder processing.

Monomolecular layers of stearic acid on metal surfaces effect a pronounced reduction in the coefficient of friction [62]. In a work with ceramic powders, the incorporation of stearic acid into a feedstock reduced the iron content of the resulting ceramic from 2200 ppm to 1200 ppm, due to decrease of abrasive wear during the mixing of the feedstock [63].

The molecular structure of stearic acid is shown in Figure 11. It is composed of a carbolixic acid group with a hydrocarbon tail.

Adsorption phenomena mainly involve van der Waals type forces, but the use of materials with carboxylic acid groups makes possible a acid-basic interaction with basic oxides and stronger coulumbic adsorption forces [64]. Stearic acid interaction to alumina powder was verified by infrared (IR) spectroscopy [65], where the affects of stearic acid were a a reduction of the viscosity of feedstock by a factor of 20, minimised separation of binder from the powder during moulding, but a higher content of binder burnout residue was observed. In a study with XPS (X-ray photoelectron spectroscopy) measurements with carboxylic acid layers on oxidized metals for MIM, it was shown that stearic acid was adsorbed on metal powders with oxide layers [66]. Due to its hydrophobic hydrocarbon tail, it has the ability to interact to the polymer materials of the same nature and so the surfactant nature of stearic acid is demonstrated [67].

$$CH_3 - (CH_2)_{16} - \overset{\overset{\displaystyle O}{\|}}{C} - OH$$
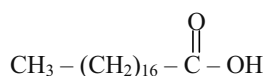
Figure 11: Molecular structure of stearic acid [59].

2.5.2   Debinding methods

The goal of debinding is to effectively remove the binder without causing defects. The choice of a binder system is strongly dependent on the chosen debinding method. The debinding methods used in PIM are shown in Figure 12. The major methods include thermal, solvent and catalytic debinding, but other unique methods may be employed as well [68].

By the solvent method, the part may be immersed in a solvent bath, in solvent vapour or solvent condensed vapour. By the thermal method, the binder component is removed by vaporisation, decomposition or melting followed by extraction through capillary forces.

In the case of a catalytic debinding, the atmosphere in which the part is immersed contains a catalyst for depolymerisation, so that the polymer molecules are decomposed during the process. This is the process developed by the company BASF [69], in which a polyacetal-based binder system is depolymerised in the presence of an acidic gas and volatises as formaldehyde.

Other unique methods exist, although they are not as prevailing as the methods previously mentioned. Unique methods include super critical debinding, thermosetting condensation process, freeze-drying and will not be discussed here.
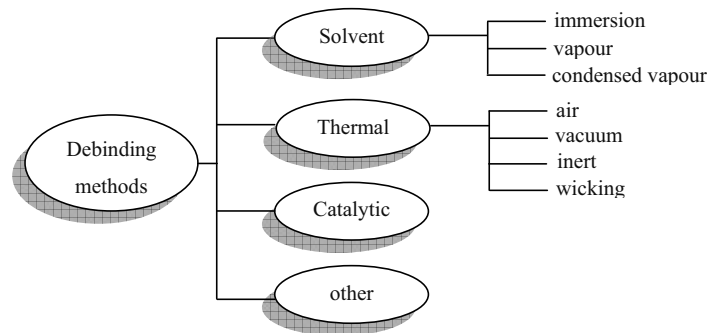
Figure 12: Overview of the various debinding techniques [68].

The solvent and the thermal debinding methods (including binder burnout and wicking) are described more in detail in the following text due to their relevance to the present work.

Solvent debinding

During solvent debinding, at least one binder component is extracted, so that pore channels are formed inside the part, providing pathways for the decomposing products to escape during the subsequent thermal debinding process.

The parts may be immersed in the liquid solvent or are exposed to the solvent vapour or solvent condensed vapour [68]. In solvent vapour or condensed solvent debinding [70], parts are placed on a debinding tray and get in contact with the solvent vapour. Although the method has the advantage that fresh solvent is constantly replenished, debinding rates are

slower as compared to immersion in liquid solvent [68]. A typical solvent debinding curve, showing the loss of binder material as a function of debinding time is shown in Figure 13.
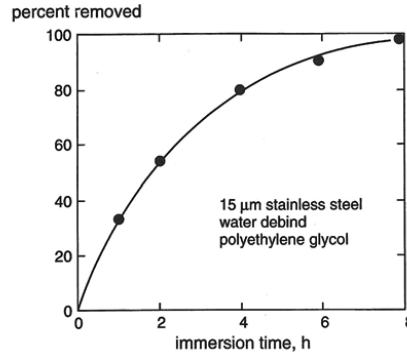
Figure 13: Extraction data for solvent debinding. Binder: polyethylene glycol basis, stainless steel compact with 6 mm wall thickness [38].

According to German [38], the solvent debinding time is dependent on the section thickness and the debinding temperature as follows:

$$t = \frac{H^2}{\beta} \ln\left(\frac{V_B}{1-\varphi}\right) \exp\left(\frac{Q}{kT}\right)$$

Formula 1

where:

t = debinding time

T = debinding temperature

H = section thickness

V_B = fraction of binder to be removed

β = binder solubility in the solvent

φ = solids loading

Q = activation energy of binder solution in solvent

k = Boltzmann's constant

Higher debinding temperatures favour a fast debinding, as suggested in the formula above and confirmed in experimental studies in the literature [71], where the debinding temperature mainly affects the debinding time for periods shorter than four hours for the parts studied.

In another study [72], the effect of the molecular weight of the first component was studied, where lower molecular weights favoured a faster debinding. In the same study, reducing the amount of the second component (a thermoplastic polymer) accelerates the extraction process as well.

Another solvent debinding model takes the volume to surface area ratio of the part in account for predicting solvent debinding times [73]. The model suggests that green parts having larger volume to surface area ratios require a longer time to debind. It predicts a similar debinding behaviour of parts with different geometries, but with similar volume to surface area ratios.

The solvent debinding process can be considered a combination of two steps [73]. In the first step, the solvent creates pores by dissolving the soluble phase on the surface of the compact. In the second step, the solvent gets into the pores via capillary transport, thereby gaining access to the soluble material inside the compact. The dissolved material diffuses through tortuous paths of solvent-filled pores and leaves the green body. Under these conditions, dissolution or diffusion, whatever is slower, becomes the rate-determining step. In the early stage of debinding (before the formation of pores), the process is preferentially controlled by dissolution because the soluble material is easily accessible. As debinding proceeds, the portion of the part still containing soluble material is relatively far from the surface, making diffusion of the dissolved material through the solvent-filled pores the rate-determining step.

Dimensional change may occur during solvent debinding and may lead to defects as cracking and slumping of the part. In a study with a non-contact laser dilatometer, dimensional changes of PIM parts during solvent debinding were evaluated [74]. The dimensional changes exhibited two stages, in which the first one is caused by the swelling of paraffin wax due to infiltration of the solvent in the wax microstructure. Swelling increases with paraffin wax density and lower solvent temperature. The final swelling is caused by the swelling of insoluble polymers and increases with increasing temperature and insoluble polymer content, decreasing solids loading and paraffin wax density. Increasing solvent temperatures increase the debinding rate. In the cited study, polypropylene (PP) and linear low density polyethylene (LLDPE) were used, which are more likely to swell in contact with solvents as compared to high density polyethylene (HDPE) [61].

Among the various solvents available, n-alkanes such as n-hexane and n-heptane are quite effective for wax-based binders systems [73] and the lower the carbon number, the higher the penetrating capability into the part [75].

Thermal debinding – binder burnout

During thermal debinding, the parts are heated up to the temperature where one of the low molecular weight binder components can decompose or evaporate while the other component remains solid [68]. When the first component is removed, the temperature is raised to decompose the second component. Very slow heating rates are usually required to avoid blistering, bubbling or cracking, which can appear if the pore channels achieved after removal of the first component are not sufficient to promote the release of decomposing gases.

A typical thermal debinding cycle may last several days, which is the drawback of the method if it is employed alone. The combination of a solvent extraction or wicking as a first step of debinding, followed by the thermal debinding of the remaining binder, reduces the overall debinding time significantly.

It is proposed in the literature [38] that with increasing debinding degree, two types of structure can be recognised in the part. In a first stage, pores are formed in the binder material between the powder particles (funicular state). In a more advanced stage, binder necks are formed between the particles (pendular state), as shown in Figure 14 below. The transition from second to third state takes place normally at binder contents of less than 20%.
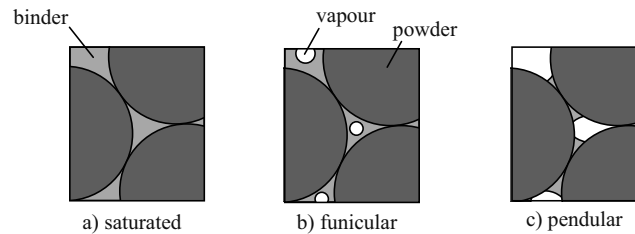
Figure 14: Schematic drawing of the structures during the thermal debinding process: a) completely filled with binder, b) funicular state, c) pendular state [38].

Thermal debinding in air under atmospheric pressure is the oldest technique and still in use [68], where the binder is decomposed by oxidative degradation. Oxides are formed on metal powders surface, which may hinder sintering. Therefore, this atmosphere is mainly used for ceramic powders.

Reducing atmospheres are preferentially employed for metal powders, where pure hydrogen, and hydrogen / nitrogen mixtures are used. Low pressure or vacuum may also be employed

during thermal debinding in order to increase the debinding rate. The thermal debinding may be conducted under inert gas flow, such as argon. The inert gas avoids contamination of the powder and sweeps away the decomposition products. The thermal debinding of titanium and titanium alloys MIM parts has been successfully performed under argon flow [7, 76].

During thermal debinding, the structure of the molecule which is thermally decomposed is of great importance if oxidation sensitive powders are used. Polyethylene does not contain oxygen in its structure and is therefore less likely to contaminate metal powders during thermal decomposition. The decomposition of PE begins with the statistical break up of molecules to primary radicals, followed by unzip reactions to ethene at higher temperatures or formation of alkanes and dienes at lower temperatures [77]. Although the degradation of PMMA molecules has been reported to follow an unzip reaction leading to monomer formation [78], the presence of oxygen in the molecule may contribute to impurity uptake in oxidation sensitive powders like titanium. The formation of char as one of the degradation products has been reported as well [79], which additionally contaminates the moulded part with carbon.

Strong contamination of powder material by PMMA is confirmed in a study with different binder systems for titanium and titanium alloys [80], where the influence of feedstock composition on the carbon and oxygen levels of the final products was investigated. The worst contamination level of oxygen and carbon in the final product were obtained when PMMA was used. The oxygen level reached 2.3 wt% and the carbon level 0.22 wt%.

The binder vapour or the decomposed molecules leave the part through its pores either by permeation, if the system is under atmospheric pressure, or by diffusion, if the system is under vacuum. The difference between debinding by permeation and debinding by diffusion lies in the different length paths of the molecules through the pores during the debinding process. Both processes were already modelled, in order to determine the debinding times versus the binder systems employed [81]. In the cited work, an isothermal process and small molecular weight of the vapour molecules were chosen as boundary conditions. A schematic drawing of the employed model is shown in Figure 15:
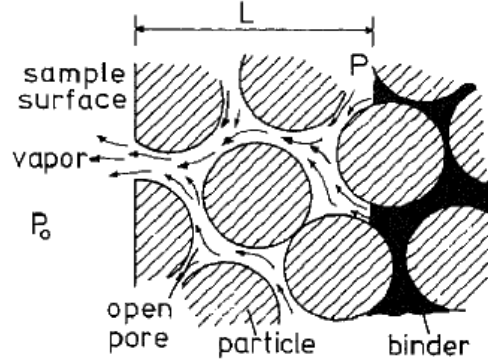
Figure 15: Schematic drawing of the pore model for the debinding by permeation or diffusion [81].

The permeation controlled debinding is found more often in practice. Hereby the debinding time t can be calculated by using the following formula [81]:

$$t = \frac{22{,}5 * H^2 P \; G(1-E)^2}{D^2 F(P^2 - P_o^2)E^3}$$

Formula 2

where:

H = thickness of the part

P = pressure at the interface binder-vapour

P_o = pressure at the surface of the part

G = viscosity of the vapour

D = particle mean diameter

F = ratio between the volume of the binder as solid and as vapour at the pressure P

E = fractional porosity (inversely proportional to the packing density)

The partial porosity E is dependent on the pore diameter R and the particle diameter D [81]:

R = 0,306.E.D

Formula 3

Formula 2 suggests that the debinding time is proportional to the vapour viscosity, the square of the part thickness, inversely proportional to the square of the particle diameter and inversely proportional to the pressure drop. The dependence on the porosity is complex. Figure 16 shows the porosity function $(1-E)^2/E^3$ versus the fractional density, in which the

34

strong dependence of the porosity at high densities is shown. This is an indication that parts with high packing densities are expected to be difficult to debind.
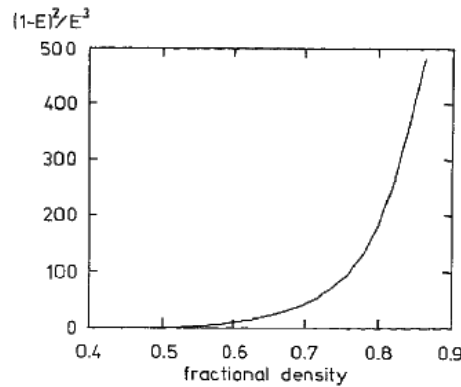
Figure 16: Dependence of the porosity on the debinding time, shown as a function of the fractional density (or packing density) [81].

For a fast debinding, the parts should exhibit low thicknesses, large particle diameters and a high porosity. Moreover, high pressure gradients and high temperatures favour a fast debinding.

Thermogravimetric analysis (TGA) is a useful method for determining the decomposition temperatures of the binder materials used and may be applied to predict debinding temperatures. In a study using TGA, it was shown that metal powders tend to catalyse the decomposition of polymers during thermal debinding [82].

In another modelling study [83], it was suggested that the total deformation of the part during thermal debinding is caused by the sum of the deformations caused by polymer content change, temperature change and internal pressure. During an initial low debinding rate period, the deformation caused by temperature increase controls the total deformation of the part and the part expands. During the subsequent high debinding rate period, the deformation caused by polymer content reduction dominates the total deformation and the entire part contracts. The deformation caused by gas pressure is minor in comparison during the whole process. According to the study, smaller powder particle size, higher powder loading, lower debinding temperatures, lower volume fraction of polymer in the binder system and a polymer with high viscosity will contribute to decrease the deformation of the moulded part.

Thermal debinding – wicking

Wicking is classified as a thermal debinding method, by which the first component of the binder system is removed. By wicking, a capillary active material, like alumina sand for instance, is employed. The sand should have relatively fine pores, so that it absorbs the binder from the moulded part through capillary transport, like shown in Figure 17:
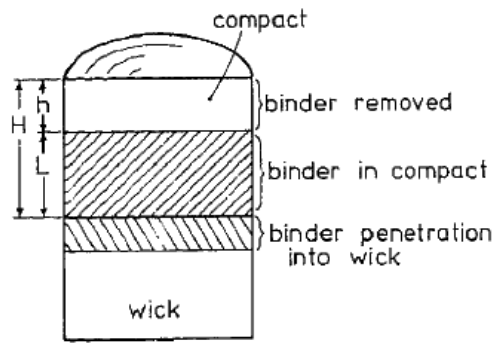
Figure 17: Schematic drawing of the removal of the binder during the wicking process [81].

This method of debinding was already modelled and the debinding time can be calculated by the following formula [81]:

$$t = \frac{4,5\ G\ H^2 D_w (1-E_c)^2}{W\ D_c (D_c - D_w) E_c^3}$$
Formula 4

where:

E_c = porosity of the part

G = viscosity of the fluid

H = thickness of the part

D_c = mean particle diameter of the powder

D_w = particle diameter of the wicking sand

W = binder surface energy

This formula suggests that the debinding time is dependent on the square of the part thickness, analogous to the permeation model previously shown (Formula 2). The dependency on the porosity behaves the same way as in Figure 16.

The deformation of the part by wick debinding was already investigated and modelled [84]. The lowest distortion was obtained with slow initial heating and low holding temperature, where the first and the second components are distinct separate phases and only the first component is in the molten state and is extracted by wicking. A temperature model which minimizes the deformation during debinding and maximizes the debinding rate was suggested. According to the model, there is a critical heating rate for debinding, which increases with increasing temperature. By following the proposed heating path, the degree of deformation of the part and debinding time would be minimised.

2.5.3 Solids loading

The amount of binder is a determining factor for a successful MIM process [38]. Too few binder leads to a high viscosity with voids in the feedstock, which brings difficulties during the moulding process. On the other hand, too much binder leads to distortion and shape loss of the moulded part during debinding and sintering. There is an amount of binder in between, which is the optimal amount for the feedstock. This amount is specific for a given powder-binder system. The three possible cases are shown in Figure 18.
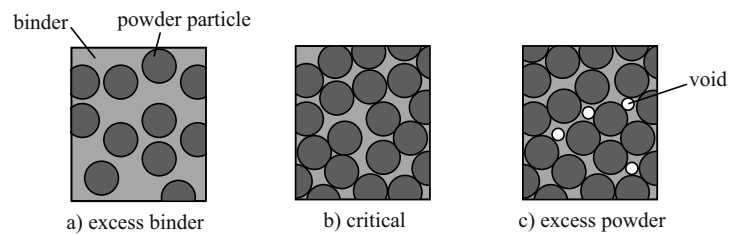
Figure 18: Three possible situations in a powder-binder mixture: a) excess binder, b) critical binder concentration, c) voids due to insufficient binder [38].

Optimal feedstocks have a little bit less powder than the critical concentration. As a first guess, the powder content lies 2 to 5 Vol.% lower than the critical value [38]. The critical point is reached when all particles are close packed and all spaces in between are filled with binder. There are different ways in order to determine the critical point or the optimal solids

loading of a specific feedstock. These include the measurement of the powder tap density, the feedstock density, the feedstock mixing torque or the feedstock viscosity.

The simplest method of determining the amount of binder to be used is the measurement of the tap density of the feedstock. After compaction of the powder through tapping of the recipient, the tap density of the material is measured and, after dividing it by the theoretical density, the percentage of empty spaces in between the particles is easily calculated. In the feedstock, the resulting empty spaces must be completely filled with binder. As a consequence, powders that are able to pack to high densities require less amount of binder. Mixtures of powders resulting in a bimodal particle size distribution result in higher packing densities as compared to monomodal powders and, as a consequence, require less binder amount. A study of the effect of the particle size distribution on packing density [85] showed a highest packing density of 78 % for powders with bimodal distribution, compared with 65 - 67 Vol.% for single distributions and 61 % for uniformly sized particles.

Another method involving density measurement involves feedstock density, as shown in Figure 19. The feedstock density increases with increasing volume fraction of powder following the mixing rule up to a point, which is the critical loading of the mixture [38]. Here, the particles are in their closest packing condition and just enough binder exists to fill the voids between the particles. Beyond that point, the density of the feedstock decreases with increasing solids content, due to the formation of voids. At zero binder content, the measured density is the powder tap density. In a study about processing of a 316-L feedstock [86], the critical loading of the mixture was determined by this method, where the density started to deviate from the theoretical value at 65 Vol.% powder.
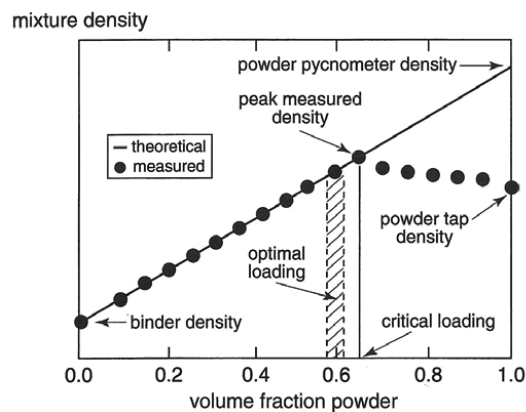
Figure 19: Loading curve showing mixture density versus volume fraction of spherical nickel aluminide powder in a wax-polymer binder [38].

Another method for determining the optimal powder content of a feedstock is by measuring the mixing torque. By torque rheometry, the mixing torque of the feedstock is measured for various powder-binder concentrations, where mixing torque increases with increasing powder content. A rapid increase in torque and an erratic torque signal are indications that the critical point has been reached. A typical torque against solids loading plot is shown in Figure 20.
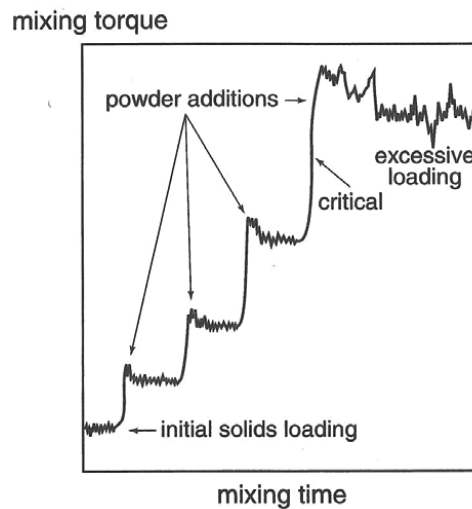
Figure 20: Mixing torque as a function of the mixing time at various levels of solids loading [38].

The method was used for determining the critical solids loading of water soluble binder based systems, where the critical loading was found to be around 65 [87] and 71 Vol.% powder [88] for the steel powders investigated. In another study [71], where a paraffin-based binder system was used with titanium powder, the critical loading determined by torque rheometry was 58 Vol.% powder. The differences in the solids loadings obtained are due to the different powder and binder systems used.

Capillary rheometry may be used for the determination of the optimal solids loading as well. The viscosity of the feedstock is measured at various solids loadings, where the viscosity increases with increasing solids content. The determination of the optimal solids loading of the feedstock by capillary rheometry brings the advantage of direct measurement of feedstock viscosity. Moreover, the flowing behaviour of feedstock may be investigated with this equipment up to shear rates typical for MIM, which may reach up to 100,000 s^{-1} [38].

The mathematical model for the viscosity of feedstock described in literature is shown below [38]:

$$\eta_M = \eta_B \frac{A}{\left(1 - \dfrac{\phi}{\phi_c}\right)^n}$$
<div align="right">Formula 5</div>

where:

η_M = mixture (feedstock) viscosity

η_B = binder viscosity

A = coefficient representing the shear rate sensitivity and particle size effects, typically near one

φ = solids loading

φ_c = critical solids loading

n = exponent found to be 2.0 for powder-binder mixtures typical for PIM

The formula above is derived from the work of Maron and Pierce [89, 90], which is regarded as the best empirical expression available for the viscosity of suspensions in polymeric liquids [91]. The parameter φ_c is related to the particle packing and has other denominations in the cited studies.

The viscosity of feedstock increases with increasing solids loading, as Formula 5 suggests. With decreasing binder content, lubrication between particles decrease, which results in viscosity increase. When the binder amount is so low that particle-particle friction takes place, viscosity increases sharply and tends to infinity. At this point, the critical point of the mixture was reached, as shown in Figure 21.
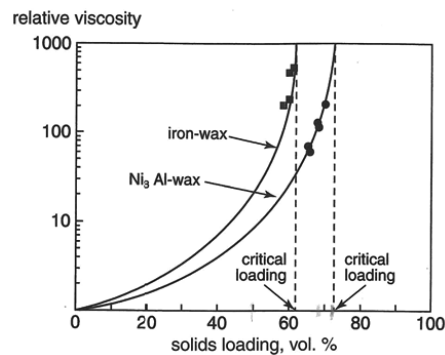
Figure 21: Viscosity versus solids loading for two powders. The coarser nickel aluminide powder has a higher packing density than the iron powder. [38]

An overview about feedstock flowing behaviour, rheology principles and capillary rheometry is going to be shown in the next section.

According to literature [38], PIM feedstocks vary from 45 Vol.% solids loadings to high values near 75 Vol.% and a few demonstrations have pushed the solids loading up to 85 Vol.%. Iron and steel powders are typically processed in the 58 to 62 Vol.% range. Powders with bimodal particle size distributions require less amount of binder, due to their higher packing density as compared to monomodal systems.

Sometimes, binder systems are especially tailored for a specific application and to increase the solids loading. By reducing the amount of the second component in a PEG-PMMA binder system, it was possible to increase the solids loading when the PMMA amount in the binder system was reduced [72].

2.5.4 Flowing behaviour and rheology

As previously mentioned, it is of great importance to determine the flowing behaviour of the feedstock for a successful MIM process.

Non-homogeneous flow and binder-powder separation tend to occur with feedstocks with very low viscosity, especially at higher shear rates or sharp direction changes [38]. As a consequence, non-homogeneous green parts may be produced, which tends to crack formation during debinding and sintering or poor mechanical properties of the sintered parts. In most severe cases, even injection may not be possible with feedstocks with phase separation. The viscosity increases sharply in areas with high powder-binder ratio, which leads to clogging of the injection moulding machine. On the other hand, a very high feedstock viscosity is also not desired, as masses with high flowing resistance require higher injection pressures to be injected, what could lead to problems during injection.

The issue of the ideal viscosity of binder and feedstock is controversially discussed in the PIM community. German [38, 92] claims that the maximal binder viscosity should be 10 Pa•s and that the maximal feedstock viscosity should be about 10^3 Pa•s, in the shear rate range of 10^2-10^3 s^{-1}. Another author [93] suggests that the binder should exhibit very low viscosity, down to 0,5 Pa•s. Actually, the values found in literature should be used as a reference and not be taken as absolute values. Each system has its own requirements and the feedstock should be specially tailored for it.

The flowing behaviour of a feedstock may be influenced by various parameters. The addition of stearic acid decreases viscosity and allows an increase in the solids loading [65, 72]. The

ratio of the binder components can be varied to modify feedstock viscosity and to make it more suitable for a specific application [51]. Different backbone polymer materials influence feedstock viscosity as well [88]. An increase in temperature usually decreases feedstock viscosity at a constant shear rate [38]. Feedstock viscosity is influenced by the solids loading as well, as discussed in the previous section. The powder size has also an effect on flowing behaviour, which will be discussed later in this section.

The capillary viscometer is a useful device for determining the flowing behaviour and measuring the viscosity of the feedstock within the range of shear rate usually found in powder injection moulding, ranging from 100 up to 100,000 s^{-1} [38]. In order to understand the working principle of a capillary viscometer, a brief overview of rheology and viscosity measurement is shown. Due to the use of metal powder and space holder particles of very different sizes in 2-C-MIM, an overview about the effect of powder size on the flowing behaviour of feedstocks follows below.

Rheology principles

Considering a material placed between two infinite parallel plates (Figure 22), the bottom one being fixed and the top one subject to an applied force parallel to the plate, which is free to move in its plane. The material is assumed to adhere to the plates and its properties can be classified by the way the top plate responds when the force is applied [94].

The mechanical behaviour of a material and its mechanical or rheological properties can be defined in terms of how the shear stress τ_{yx} (force per unit area) and shear strain γ_{yx} (which is a relative displacement) are related. These are defined, respectively, in terms of the total force (F_x) acting on area A_y of the plate and the displacement (U_x) of the plate, as shown by Formulas 6 and 7 below:

$$\tau_{yx} = \frac{F_x}{A_y}$$

Formula 6

$$\gamma_{yx} = \frac{U_x}{h_y} = \frac{du_x}{dy}$$

Formula 7

The manner in which the shear strain responds to the shear stress defines the mechanical or rheological classification of the material. For a rigid material, $\gamma_{yx} = 0$, as it will not move at all no matter how much force is applied. If the material is purely elastic, the top plate moves a distance which is in proportion to the applied force and then stops. The correlation in this case is $\tau_{yx} = G\gamma_{yx}$, where G is a constant if the material is linear elastic, or G is a function if the

42

material is nonlinear elastic. If the material flows continuously and does not stop, it is classified as a fluid. If it flows in such a way that the force is proportional to the relative rate of movement (the velocity gradient), the material is a Newtonian fluid. The equation that describes this behaviour is:

$$\tau_{yx} = \eta \dot{\gamma}_{yx} \hspace{4cm} \text{Formula 8}$$

where η is viscosity of the fluid. If shear stress and shear rate are not directly proportional but are instead related by some more complex function, the fluid is said to be non-Newtonian. If the material has both the elastic (solid) and viscous (fluid) properties, it is said to be viscoelastic. Most polymers fall into this classification.
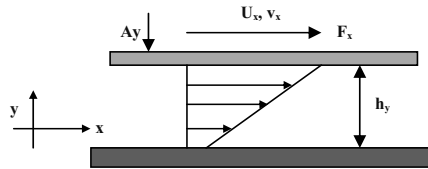
Figure 22: Schematic drawing for illustration of simple shear [94].

Determination of the shear viscosity

For the determination of the shear viscosity, different types of viscometers can be employed. A rotational viscometer may be used for the determination of the viscosity of binder components and binder systems employed for PIM, where the torque required to rotate a disc at a certain speed is recorded. The torque required to rotate the disc is proportional to the viscosity of the fluid, which can be then calculated. The suitability of such equipment for the characterisation of PIM feedstocks is impaired as powder particles can be large enough not to fit in between the plate gap, depending on the powder used. Alternatively, the determination of feedstock viscosity is preferentially done by using a capillary viscometer, in a process analogous to the injection of the material by the injection moulding unit. Due to the relevance for this work, an overview of the calculation of the shear viscosity using a capillary viscometer is presented next.

In a capillary viscometer, the shear stress and the shear rate are correlated for the calculation of viscosity. A schematic drawing illustrating the working principle of the capillary viscometer is shown in Figure 23. The investigated material is pressed by a plunger, which can be operated at different pressing velocities, through a nozzle with known geometry [95].

43

In this way a laminar flow profile is developed in the capillary and if the volume flow is known, the shear rate can be calculated. The resistance of the material to flow causes a pressure drop along the capillary, which corresponds to a specific shear stress. This pressure drop is the actual measured variable. Due to the small diameter of the nozzle, the pressure is not directly measured in the nozzle, but in the inlet area.
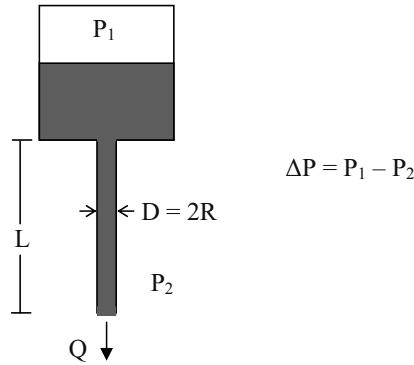
Figure 23: Schematic drawing of a capillary viscometer [94].

In principle, from the measured pressure, the shear stress is obtained (Formula 9) and from the known volume flow, the shear rate is known (Formula 10). From the quotient of the shear stress and shear rate, the shear viscosity is calculated (Formula 11). The subscript "app" stands for "apparent". The terms are "apparent" because corrections must be applied in order to get the "true" values, as will be shown later.

$$\tau_{app} = \frac{R \cdot \Delta P}{2L}$$ Formula 9

$$\dot{\gamma}_{app} = \frac{4Q}{\Pi R^3}$$ Formula 10

$$\eta_{app} = \frac{\tau_{app}}{\dot{\gamma}_{app}}$$ Formula 11

where:

τ_{app} = apparent shear stress

$\dot{\gamma}_{app}$ = apparent shear rate

η_{app} = apparent viscosity

R = radius of the capillary

ΔP = pressure drop

L = length of the capillary

Q = volume flow rate

Formula 8 is derived from a momentum balance in the capillary. By the general conservation law of a system (for energy, mass and momentum) [94]:

Rate of X into the system	-	Rate of X out of the system	=	Rate of accumulation of X in the system

where X is the conserved quantity.

By Newton's second law, the rate of momentum is equivalent to force. In addition to the rate of momentum convected into and out of the system by the entering and leaving streams, the sum of all the forces that act on the system (the system defined as a specific volume of fluid) must be included. The resulting macroscopic conservation of momentum then becomes:

$$\sum_{onsystem} \vec{F} + \sum_{in} (\dot{m}\vec{V})_i - \sum_{out} (\dot{m}\vec{V})_o = \frac{d}{dt}(\dot{m}\vec{V})_{sys}$$

Formula 12

If there is only one entering and one leaving stream, then $\dot{m}_i = \dot{m}_o = \dot{m}$. The mass flow $\dot{m}$ can also be written as $\dot{m} = \rho\vec{v}\vec{A}$, where ρ is the density of the fluid, $\vec{v}$ is the average velocity through the cross sectional area $\vec{A}$. We apply the momentum balance to a fluid in a plug flow in tube, as illustrated in Figure 24. The fluid element in the "slice" of dx is the system, and the momentum balance equation on this system is:

$$\sum_{onfluid} F_x + \dot{m}V_x - \dot{m}(V_x + dV_x) = \sum_{onfluid} F_x - \dot{m}dV_x$$

$$= \frac{d}{dt}(\rho V_x A dx) = 0$$
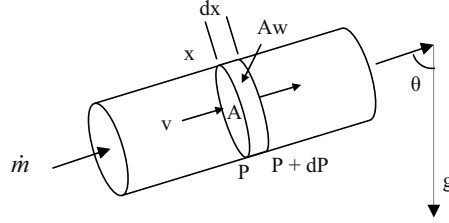
Formula 13

Figure 24: Momentum balance on a „slice" in a stream tube [94].

The forces acting on the fluid result from pressure (dF_p), gravity (dF_g), wall drag (dF_w) and external shaft work ($\delta W = - F_{ext} dx$), so that:

$$\sum_{onfluid} F_x = dF_p + dF_g + F_{ext} + dF_w \qquad \text{Formula 14}$$

where:

$$dF_p = A_x (P - (P + dP)) = -A_x dP$$

$$dF_g = \rho g_x A_x dx = -\rho g A_x dx \cos\theta = -\rho g A_x dx$$

$$dF_w = -\tau_w dA_w = -\tau_w W_p dx$$

$$-\delta W = F_{ext} dx$$

Here, τ_w is the stress exerted by the fluid on the wall (the reaction to the stress exerted on the fluid by the wall) and W_p is the perimeter of the wall in the cross section that is wetted by the fluid ("the wetted perimeter"). After substituting the expressions for the forces from Formula 13 into the momentum balance equation, Formula 12, and dividing the result by $-\rho A$, where $A = A_x$, the result is:

$$\frac{dP}{\rho} + gdz + \frac{\tau_w W_p}{\rho A} dx + \delta w + VdV = -\frac{dV}{dt} dx \qquad \text{Formula 15}$$

where $\delta w = \delta W/(\rho A dx)$ is the work done per unit mass of fluid. Integrating this expression from the inlet (i) to the outlet (o) and assuming steady state gives:

$$\int_{P_i}^{P_o}\frac{dP}{\rho} + g(z_o - z_i) + \frac{1}{2}(V_o^2 - V_i^2) + \int_L \frac{\tau_w W_p}{\rho A}\,dx + w = 0 \qquad \text{Formula 16}$$

Comparing this with the Bernoulli equation:

$$\int_{P_i}^{P_o}\frac{dP}{\rho} + g(z_o - z_i) + \frac{1}{2}(V_o^2 - V_i^2) + e_f + w = 0 \qquad \text{Formula 17}$$

shows that they are identical, provided:

$$e_f = \int_L \left(\frac{\tau_w W_p}{\rho A}\right)dx \qquad \text{Formula 18}$$

or, for steady flow in a uniform conduit:

$$e_f \cong \frac{\tau_w W_p L}{\rho A} = \frac{\tau_w}{\rho}\left(\frac{4L}{D}\right) \qquad \text{Formula 19}$$

Where e_f is the dissipated energy associated with irreversible effects, directly related to the stress between the fluid and the tube wall (τ_w), or it can be interpreted as the work required to overcome the resistance to flow.

By taking Formula 19 and substituting in Formula 17 and assuming constant flow rate, no external shat work and neglecting the gravitational force, Formula 9 is obtained, which shows the shear stress at the wall of the capillary viscometer:

$$\tau_w = \frac{R.\Delta P}{2L} \qquad \text{Formula 9}$$

Considering that the wall shear rate for a Newtonian fluid in a tube is given by [94]:

$$\dot{\gamma}_w = \frac{8V}{D} = \frac{8V}{2R} = \frac{4V}{R} \qquad \text{Formula 20}$$

As V is the mean fluid velocity and can be written as $V = Q/ (\Pi R^2)$, and substituting it in Formula 20 yields:

$$\dot{\gamma} = \frac{4Q}{\pi R^3}$$

Formula 10

The viscosity is then calculated by the quotient between the wall shear stress and the wall shear rate, as showed previously in Formula 10. A typical viscosity versus shear rate curve obtained with a capillary viscometer is shown in Figure 25. The effect of the addition of stearic acid is shown and the shear thinning behaviour, typical for PIM feedstocks, is evident.
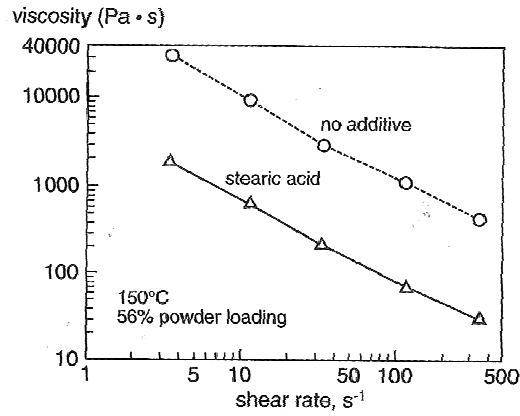
Figure 25: Viscosity versus shear rate for carbonyl iron in a wax-polymer binder, showing the effect of stearic acid [38].

Bagley correction

It must be pointed out that additional pressure drops occur at the entrance area of the capillary [95]. These can occur due to acceleration of the material compared to the flowing velocity in the capillary, due to secondary streams, but mainly due to elastic deformation of the material at the entrance of the die. These additional pressure drops should be known and the proper corrections must be applied, so that the true shear stress is known.

If an experiment is run with dies of different lengths L, but of the same radius R, under the same conditions, the pressure drop can be measured and an extrapolation of the results allows the pressure drop of a "zero-length" die to be calculated. This yields the pressure drop at the entrance of the die, and not in the capillary. If a single bore capillary rheometer is used, the

measurement should be repeated with dies of different lengths, so that the true viscosity is obtained. So, if a die with length $e \cdot R$, in which e represents the extrapolated L/R-ratio, the following equation is derived for the corrected shear stress after Bagley [95]:

$$\tau_w = \frac{\Delta P \cdot R}{2(L + e \cdot R)}$$

Formula 21

The determination of the entrance pressure drop by Bagley extrapolation is illustrated in Figure 26, where different behaviours are expected in a low and in a high shear rate regime:
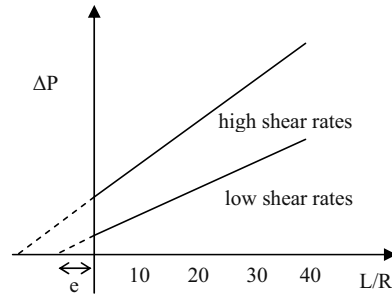
Figure 26: Determination of the entrance pressure drop by Bagley extrapolation [95].

This type of Bagley correction is not only time consuming but also problematic, as by extrapolation wrong values for the entrance pressure drop may obtained. It could happen that the material exhibits wall-slip, so that the total pressure drop is not proportional to the die length, among other effects which lead to a non-linear correlation between total pressure drop and die length. Due to this non-linearity, this method is normally associated with errors. It is difficult even with three or more points to extrapolate to a "zero length" die.

The advantage of a double capillary viscometer lays in the fact that by using one of the bores with a "zero length" or "orifice die" (actually with a very small length), the value for the entrance pressure drop ΔP_o is determined for this small capillary. At the same time, the other bore contains a capillary with length L. In this way, the corrected shear viscosity can be obtained after one measurement. The Bagley corrected wall shear stress is obtained after the following equation:

$$\tau_w = \frac{(\Delta P_l - \Delta P_o)R}{2L}$$

Formula 22

where ΔP_l is the measured pressure drop in the capillary with length L and radius R.

Rabinowitsch correction

As a result of a constant shear rate measurement, the dependency of the shear stress to the shear rate is obtained. From this, the viscosity curve can be calculated, as previously discussed. If the viscosity is independent of the shear rate, so the material exhibits a Newtonian behaviour.

Nevertheless, materials exhibit often behaviours which deviate from the Newtonian. Some substances exhibit pseudoplastic or shear thinning behaviour, whereas others exhibit dilatant or shear thickening behaviour. A combination of these or more complex behaviours are possible as well. The Rabinowitsch correction takes into account the deviations from the Newtonian behaviour. These examples of behaviour under shear are shown in Figure 27 below:
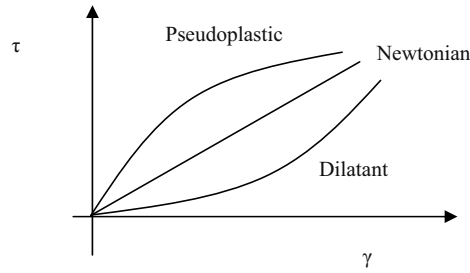
Figure 27: Examples of different flowing behaviours under shear.

The correction is done by plotting log τ_w / log γ_{app} and calculating the slope of the curve obtained, which is the parameter "n". The corrected shear rate can be calculated after Rabinowitsch by the following equation [96]:

$$\dot{\gamma}_w = \frac{3n+1}{4n}\dot{\gamma}_{app}$$
Formula 23

If the slope of the curve is one, i. e. if the material exhibits Newtonian behaviour, the true wall shear rate is the same as the actual value measured.

50

Effect of powder size

The evaluation of the stability of PIM-feedstocks in an experimental rheological study is described in the literature, where the influence of powder size on feedstock stability was investigated with a capillary viscometer [97]. Spherical particles with various particle sizes were employed in feedstocks with 55 Vol.% solids loading. The instability of the feedstock, characterised by the variation of the viscosity during the measurement, was found to increase with the particle size.

Still according to the mentioned study, there is a difference between the flow behaviour of bimodal and monosized powders. Feedstocks made of blended powders showed an increased instability compared to feedstocks made of monosized powders. Such a phenomenon would be related to a segregation of particles of different size within the feedstock. During flow through the capillary tube, particles suspended in a fluid migrate from the wall toward the centreline in a phenomenon called the Segre-Silberg effect. When entering the faster moving stream near the core of the tube, the particles are transported more rapidly than the average of suspension and a concentration gradient occurs. This effect becomes more important for the larger particles, in the case of the feedstocks with bimodal particle distribution. This concentration gradient of feedstocks made of blended powders may indicate these feedstocks are more prone to concentration gradients in a variable shear rate regime, compared to the feedstocks made of monosized powders. Such concentration gradients would result in viscosity variation and increased risk of separation.

Goto and Kuno [98] made kinetic studies of the motion of bimodal suspensions of polystyrene particles, with 398 and 84 μm average diameters, in ethylene glycol and propylene glycol with a capillary viscosimeter. The study of this group included taking pictures of the suspension flow with a high-speed camera. In this way, the number of particles near the wall could be counted and a quantitative study was developed. The viscosities of bimodal suspensions were always smaller than those of single solid component suspensions under the same total solid volume fraction. Furthermore, when the mixture passed through the capillary tube, it was observed that the proportion of large and small particles at the wall varies with the shear rate. For the monosized suspension, the number of particles near the wall for the low shear rate regime ($\sim$200 s^{-1}) is greater than that for the high shear rate regime ($\sim$3400 s^{-1}). On the other hand, for the suspension of blended powders, the number of larger particles near the wall for the low shear rate regime is smaller than that for the high shear rate regime. Moreover, for the low shear rate regime, the number of large particles near the wall for the

51

blended suspension is smaller than that for the single solid component suspension. This suggests that the radial distribution of larger particles is affected by the presence of smaller ones and this changes the viscosity of the suspension, as the decrease of the number of particles located near the tube wall reduces the viscosity.

In another study [99], where feedstocks with monodispersed glass beads were used, the viscosity was shown to approach infinity at around 60 Vol.% solids loading, independent of particle size. The viscosity of bimodal systems was lower and the minimum viscosity of a bimodal system was achieved with 25 to 35 Vol.% of the fine particles, the remainder being the coarser size.

The effect of lower viscosity with bimodal systems is also predicted in Formula 5. Systems with bimodal particle size distributions have higher packing densities and therefore higher values for the φ_c parameter, which lead to lower viscosity values for the feedstock.

Similar flowing phenomena are expected if feedstocks with and without space holder particles are used. The space holder particles are much coarser than the metal particles and this difference in size is likely to contribute to different flowing behaviours of the feedstocks.

2.6   State of the art in Jülich

The space holder method (SHM) was extensively studied at *Forschungszentrum Jülich* for the fabrication of medical implants. Titanium porous cups for hip replacement [100, 101] were produced by pressing and machining in the green state. The porosity of the samples lied in the range of 60-75 % and space holder particles in the range of 355-500 μm were used. Dental implants with a porous coating [102] were produced by cold isostatic pressing of the coating on a dense substrate, with similar porosity and pore sizes. The space holder material preferentially used was ammonium hydrogen carbonate. These implants are shown in Figure 28.
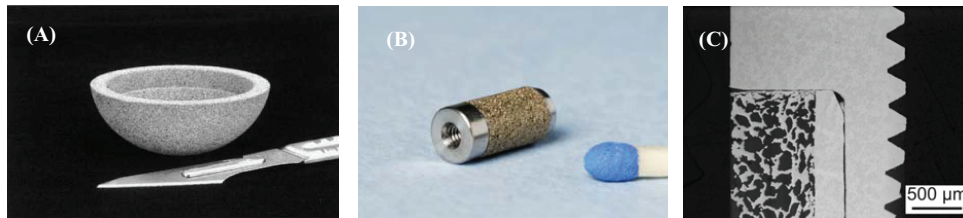
Figure 28: (A) Porous cup for hip replacement. (B) Dental implant with porous coating. (C) Microstructure of the cross section of the dental implant.

Another research group conducted an *in vivo* study [103], where the pores of an implant produced with the space holder method were completely filled with bone tissue 12 weeks after implantation. The picture of the cross section of the bone is shown in Figure 29. The space holder used was ammonium hydrogen carbonate and the overall porosity of the implant was 60%, with pores in the range of 100 to 700 μm.
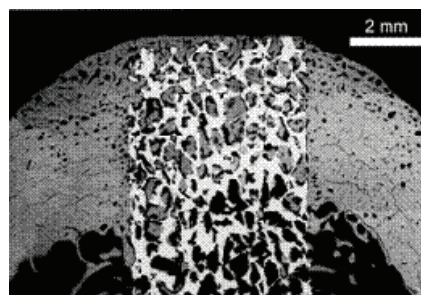
Figure 29: Cross-section of a porous titanium implant (white) produced with the SHM. Full bone ingrowth after 12 weeks of the implantation [103].

The space holder method was used for the fabrication of the spinal implants in Figure 30 as well. The processing method developed at *Forschungszentrum Jülich* was licensed to the company Synthes for the development of spinal implants with a gradient in porosity. This spinal implant is composed of a porous part (porosity 60-65 %) and a part with clearly reduced porosity, responsible for the fixation of the implant after surgery [6]. Here, it was shown that for implant applications in the lumbar spine, a porosity in the range of 60 to 65% was more adequate. The implant is placed between two vertebrae and replaces the lumbar disc. Similarly to the concept of the cages shown in Figure 1, the neighbouring bone tissue grows into the structure of the implant. Nevertheless, the special porous structure of the implant produced by the space holder method is advantageous regarding the primary fixation to the bone, due to the development of a more homogeneous distribution of bone tissue from the vertebrae in the implant. This enhances the overall mechanical stability of the system.
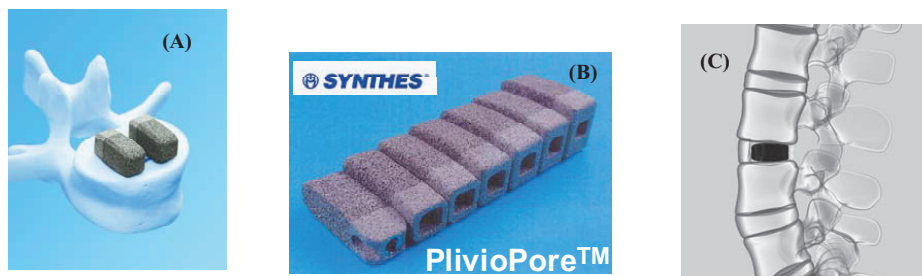
Figure 30: Spinal implant of the company Synthes. (A) Implants on the vertebra bone. (B) Row showing the different sizes available. (C) Implant placement after surgery. [104]

A specific feature of this spinal implant is the rotation during the surgery procedure, as shown in Figure 31. This rotation promotes a permanent tension of the adjacent vertebrae on the implant, which avoids implant migration and supports bone ingrowth. For this rotation procedure, sufficient implant strength is required, which is ensured by the dense part of the implant.

Figure 31: Drawing showing the rotation procedure of the implant during surgery.

The MIM technique has recently been investigated in combination with the space holder method for the fabrication of near net shaped porous implants at *Forschungszentrum Jülich*. Among the materials studied, sodium chloride was found to be the most appropriate space holder material to be used in combination with the MIM process, due to its thermal and mechanical stability and minimum contamination of the metallic matrix [76]. The MIM process in combination with SHM was used for the production of simple shaped parts of NiTi, Ti6Al4V and Ti materials. On cylinders, the mechanical and biological properties of porous NiTi alloys produced by MIM were studied in detail regarding their suitability as implant material and damping devices [7].

Among the great variety of binder systems possible for the MIM process, binders composed of a mixture of paraffin, polyethylene and stearic acid are reported to be used for Ti6Al4V [105] and Ti powders [106] for the fabrication of medical implants with success, but no indication about trade names of binder components, binder components ratio or component characteristics like molecular weight or viscosity are available. The first component is removed by extraction with hexane or heptane. The binder system with this composition is employed by the company *TiJet Medizintechnik GmbH* [107] for the commercialised products. A binder system of a similar composition was employed for the fabrication of NiTi parts as well [108]. Another binder system with an aromatic compound (naphthalene) was described in the literature to be suitable for titanium powder [109], but no evidence of its use in the industry has been found.

The binder system used so far at *Forschungszentrum Jülich* is a mixture of 60 Vol.% amide wax (Wax C) and 40 Vol.% polyethylene wax (PE 520). This binder system was developed in the early 1990s in Jülich [110, 111] and was recently used for the production of net-shaped NiTi with [112] and without [113] space holder particles by metal injection moulding. Although this binder system is composed only of two components, its suitability for the

production of titanium and titanium alloys parts by MIM in combination with the space holder method was demonstrated, together with acceptable contamination levels [7, 76]. Up to now, only simple geometries like cylinders and discs were produced and the main disadvantage of this binder system lays on the partial debinding method, which is the wicking method. The wicking method is laborious, as sand residues have to be removed from the part surface after debinding, which deteriorates surface quality.

Titanium and titanium alloys powders with space holder have been processed with 75 Vol.% solids content, in which 50 Vol.% of the solids fraction is composed of space holder particles, whereas feedstocks without space holder have been processed with 68 Vol.% powder [7].

3 Objectives of this work

The combination of SHM with 2-C-MIM would enable the near-net-shape production of implants with a gradient in porosity without the need of green machining, as it is the case of the current production method of the spinal implant of the company Synthes (Figure 30). This would impart costs reduction in case of large scale production of such implants. The 2-C-MIM brings advantages when compared to isostatic pressing of a coating with space holder particles as well, as it is the case of the production of the aforementioned dental implants (Figure 28). The MIM process brings up the possibility of producing parts with complex geometry, what is limited in the case of pressing of a porous coating. Porous coatings are also a concern when regarding their fatigue strength. Interface regions can always act as stress concentrators, compromising the use of these materials in high-loading applications. This was seen in the interface region between the dense core and the porous coating of the dental implant. This area acted like a weakness point of the structure and a notch was seen in that region after a fatigue test [102]. The problem was overcome with an additional weld seam at the interface, but this would mean a post-processing step in the production process. This disadvantage applies for all methods involving coatings, such as plasma spraying, fibre or powder sintering on substrates. It is reported that the current practice in designing porous-coated titanium and titanium alloys is to avoid porous coatings on surfaces that might be subjected to substantial tensile stresses in service [15]. The bonds between substrate and coating have been shown sometimes inadequate in several clinical applications, where radiographic evidence of porous coating separation from the implant is available [114].

The near-net-shape production of implants with graded porosity by 2-C-MIM would mean a cost reduction in case of a large scale production, as compared to all other methods cited previously. The method combines shape flexibility with fast production cycles. The objective of this work is to develop the 2-C-MIM technique in combination with the space holder method for the fabrication of implants with graded porosity.

According to what was described in the last sections, a profile of a suitable binder system for 2-C-MIM for the production of titanium implants with a gradient in porosity is proposed. The requirements for a suitable binder system are to:

• be suitable for debinding and sintering, with and without space holder;

- show suitable flowing behaviour for injection moulding with and without space holder particles during the filling of complex shaped cavities with changes in flow direction without binder-powder separation;
- have the decomposition temperature above injection moulding temperature;
- decompose with the least contamination possible of the metal powder during thermal debinding;
- promote the least dimensional changes possible after processing steps;
- ensure mechanical stability of the part for handling during processing steps.

The feedstock suitable for 2-C-MIM should have the least amount of binder possible for injection moulding, in order to avoid part distortion and shape loss, as usual for any MIM feedstock. Additionally, the amount of binder to be used for the feedstocks with and without space holder particles should be adjusted so that a mismatch in sintering shrinkage of both feedstocks is avoided. Such a mismatch may produce defects and distortions in the final part.

4 Experimental part

4.1 Processing techniques

4.1.1 Starting materials

The starting powders and space holder used in this work are listed in Table 2. Although the typical grain size used in the MIM technique is from 0,1 to 20 or 10 μm in average [38], the use of coarser powder fractions (< 45μm) was preferred in this work. In previous investigations [112], the use of finer powders in combination with the space holder method was unsuccessful. The small powders hindered desalination and the NaCl could not be completely removed even after very long desalination periods. The NaCl particle size range was chosen due to the desired pore size in the final product. Pore sizes in the range of 350-500 μm were reported in the literature to be adequate for bone ingrowth in the implant material [2, 10, 14].

Titanium powder was used for the production of samples for preliminary studies with different binder systems and for the production of implants. Fe22Cr-powder was employed for the rheological characterisation of feedstocks. As rheological measurements required relative high amounts of feedstock, cheaper Fe22Cr powder was used for this purpose. Due to the similar particle size ranges of the Ti- and the Fe22Cr-powder, it was assumed that feedstocks produced with either powder would exhibit similar flowing behaviour.

Table 2: Starting powder materials used in this work. Ti and Fe22Cr: particle size range as delivered by manufacturer, NaCl: fraction sieved from starting material. Data as in product data sheet.

Powders	Manufacturer	Charge	Particle size range	Theoretical density (g/cm³)
Ti (Grade II)	TLS Technik	1071/3	< 45μm	4.51
NaCl	AppliChem	8 O 010051	355-500 μm	2.17
Fe22Cr	H.C. Starck	0549.01	20-53 μm	7.67

The binder components chosen for the investigations are shown in Table 3.

Wax C and PE 520 are binder components of the standard binder system used in *IEK-1* at *Forschungszentrum Jülich* and were used for investigations with this reference binder system.

A paraffin material (Paraffin 65) was chosen for the new binder systems, in which solvent debinding would be performed as the partial debinding step. Solvent debinding replaces the wicking process, which is less appropriate for the industrial application. Paraffin is reported to

be a suitable material to undergo solvent debinding and paraffin-based binder systems have been reported to be used for Ti [106], Ti6Al4V [105] and NiTi [108] powders. The industrial use of a paraffin-based binder system has been reported for titanium powder as well [107].

As second component of the new binder systems, different polyethylene materials were chosen primarily due to the difference in viscosities. The polyethylene waxes PE 520 and PE 190, and the conventional polyethylene material Hostalen GA 7260 G have been investigated for this purpose. According to the producer, PE 520 is less viscous than PE 190 at the same temperature. The Hostalen material, as being a conventional polyethylene material and no polyethylene wax, is expected to have a higher viscosity than PE 520 and PE 190 [56], although no direct viscosity value is available at the product data sheet. This Hostalen material was chosen among the great variety of polyethylene materials available in the market because it is an almost additive-free material and is designed for the production of plastic parts for advanced applications in the medical field, as advised by the manufacturer. Its low additive amount (500 ppm calcium stearate) is expected to be suitable for a low residue amount after thermal debinding. No information about chemical composition or additives was supplied for PE 520 and PE 190 by the manufacturer. The application of PE 520, PE 190 and Hostalen GA 7260 G as second binder component is expected to cover a wide range of viscosity, so that the influence of binder viscosity on feedstock characteristics as the flowing behaviour could be investigated.

Stearic acid was added to some feedstocks as the third binder component, in order to investigate its expected lubricant behaviour.

Table 3: Binder components used in this work. If not otherwise specified, the data is from product data sheet.

Component	Producer	Density (g/cm^3)	Melting temperature (°C)	Viscosity (Pa.s)
Wax C	Clariant	1.00	142	-
Paraffin 65	Sigma-Aldrich	1.01 [59]	> 65	-
PE 520	Clariant	0.92-0.94	117-123	0.65 (at 140°C)
PE 190	Clariant	0.95-0.97	132-138	25 (at 140°C)
Hostalen GA 7260 G	Basell	0.96	-	-
Stearic acid	Merck	0.94 [59]	-	-

With the binder components listed in Table 3, binder systems were composed as shown in Table 4. The standard binder is composed of Wax C and PE 520. The binder systems BS 1, BS 2 and BS 3 are composed of Paraffin 65 and either PE 520, PE 190 or Hostalen GA 7260

G as second component. For these binder systems (SB, BS 1, BS 2 and BS 3), the ratio of the first to the second component was kept constant to 60/40 Vol.%, as reported to be suitable for the successful production of MIM parts [38] and found suitable in previous studies with the SB system [112]. For feedstocks with the SB system, the first debinding step employed is wick extraction. For the paraffin-based binder systems, on the other hand, solvent debinding was chosen as the partial debinding method.

The addition of stearic acid and the variation of component ratio on the feedstock behaviour were investigated in the systems BS 4 and BS 5. As given in the literature [115, 116], an amount of stearic acid of about 4 wt.% of the binder is suitable to obtain the desired lubrication of the feedstock. In this work, 5 Vol..% (or 4.7 wt.%) was the percentage of stearic acid used. As stearic acid is soluble in hexane [117], it is expected that the material is removed during solvent extraction. The amount of Hostalen GA 7260 G was decreased in 5 Vol.% in the system BS 5, in order to investigate the effect of the binder component ratio on the flowing properties of the feedstock.

Table 4: Binder systems investigated in this work. The number in brackets is the volume ratio of the component.

	1st component	2nd component	3rd component
SB	60 Vol.% Wax C	40 Vol.% PE 520	-
BS 1	60 Vol.% Paraffin 65	40 Vol.% PE 520	-
BS 2	60 Vol.% Paraffin 65	40 Vol.% PE 190	-
BS 3	60 Vol.% Paraffin 65	40 Vol.% Hostalen GA 7260 G	-
BS 4	55 Vol.% Paraffin 65	40 Vol.% Hostalen GA 7260 G	5 Vol.% Stearic acid
BS 5	60 Vol.% Paraffin 65	35 Vol.% Hostalen GA 7260 G	5 Vol.% Stearic acid

Based on these binder systems, different feedstocks with Ti as well as Fe22Cr powders were prepared. The list of the investigated titanium feedstocks is shown in Table 5. Titanium feedstocks with the binder systems SB, BS 1, BS 2 and BS 3 with and without space holder were used for preliminary experiments with the warm press. The feedstocks with space holder had a constant amount of 50 Vol.% of space holder particles. This amount of space holder material was used, as higher amounts of space holder could not be injected with the MIM machine in previous experiments with the same space holder particles [112]. The solids loading was 68 Vol.% for feedstocks without space holder and 75 Vol.% for feedstocks with space holder, as used in previous works with the standard binder system [112]. Titanium

feedstocks with BS 4 and BS 5 systems were produced after optimisation of the solids loading after viscosity measurements with the capillary viscometer, where Fe22Cr powder was used.

Table 5: Ti feedstocks investigated in this work.

Feedstock	Solids loading Φ (vol %)	Binder content 100 – Φ (vol %)	Metal powder fraction of the solids loading (vol %)	Space holder fraction of the solids loading (vol %)
Ti SB	68	32	100	0
Ti SB SH	75	25	50	50
Ti BS 1	68	32	100	0
Ti BS 1 SH	75	25	50	50
Ti BS 2	68	32	100	0
Ti BS 2 SH	75	25	50	50
Ti BS 3	68	32	100	0
Ti BS 3 SH	75	25	50	50
Ti BS 4	64	36	100	0
Ti BS 4 SH	68	32	50	50
Ti BS 5 SH	72	28	50	50

The Fe22Cr feedstocks investigated are listed in Table 6. Fe22Cr feedstocks with various solids loadings were produced for investigations with the capillary viscometer.

Table 6: Fe22Cr feedstocks investigated in this work.

Feedstock	Solids loading Φ (vol %)	Binder content 100 – Φ (vol %)	Metal powder fraction of the solids loading (vol %)	Space holder fraction of the solids loading (vol %)
Fe BS 2	50/60	50/40	100	0
Fe BS 3	50/60/64/68	50/40/36/32	100	0
Fe BS 4	50/60/64/68	50/40/36/32	100	0
Fe BS 4 SH	50/60/68/72	50/40/32/28	50	50
Fe BS 5 SH	60/68/72/75	40/32/28/25	50	50

4.1.2   Feedstock preparation

The feedstocks were prepared by mixing the powder and the binder in a Haake HKD-T 0,6D kneader. The binder components were firstly mixed by hand with the powder and space holder particles before introducing the mixture in the kneader. The material was allowed to homogenise for a total of 2 hours at 150°C. After the homogenisation in the kneader, the material was taken out of the chamber and reduced to smaller pieces by hand while cooling down. The pieces were granulated in a granulator of the company Wanner Technik GmbH, Wertheim/Main.

4.1.3   Shaping by warm pressing

The shaping process by warm pressing was used when small amounts of feedstock had to be investigated. The warm press required much less effort of processing as compared to the MIM process, so that it was employed as a first evaluation of a new feedstock. Although the warm pressing is a much simpler and less sophisticated shaping technique than the MIM process, the basic principle of both processes is similar: the feedstock is warmed above the melting temperature of the binder and injected / pressed to the desired shape while cooling down.

The feedstocks were warm pressed with a modified P/O/Weber press. A schematic drawing of the press is shown in Figure 32. The feedstock material was placed in between the two pressing plungers and allowed to heat up for 2 minutes. A piece of fine aluminium foil was placed between the lower pressing plunger and the cooled pressing matrix to avoid the material to fall into the pressing matrix before starting the pressing procedure. The material was pressed with 12,5 kN force (110 MPa) with 30 seconds holding time, while cooling down in the water cooled pressing matrix. Cylindrical compacts with 12 mm diameter and approximately 10 mm height were produced. An attempt was made so that all the samples had an approximately constant height. This was done by using a balance to weight the same quantities of feedstock material to be pressed. Direct measurements of the temperature of the die with a thermocouple placed in a drilled hole in the die wall revealed that the measured temperature shown by the equipment was actually lower than the actual temperature of the material inside the press. In a reference measurement using another thermocouple, it has been shown that a temperature of 132°C shown by the equipment is related to a temperature of 150°C inside the press, ensuring a complete melting of the binder systems used in this work.
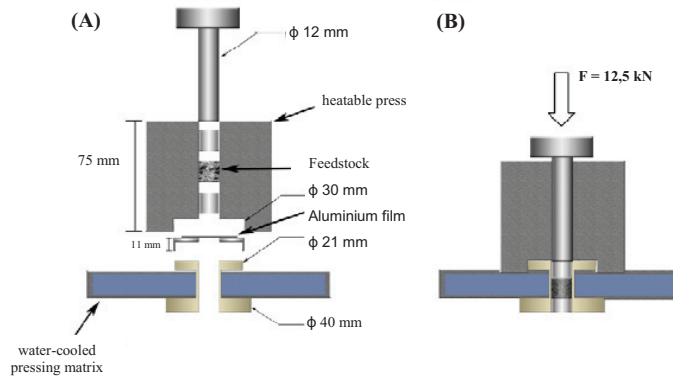
Figure 32: Schematic drawing of the P/O/Weber press. (A) Device before the pressing procedure (B) Pressing procedure with pressing force of 12,5 kN. [112]

4.1.4 Shaping by Metal Injection Moulding

Although warm pressing delivers a very useful first impression of the investigated feedstock, shaping by MIM is the actual aim to the feedstocks investigated. MIM is much more complex than warm pressing, especially because of the wide range of shear rates to which the feedstock is subjected during the process, which could reach up to 100,000 s^{-1} [38], depending on the injection flow rate and flowing channels inside the equipment and the mould.

All MIM experiments were conducted with an Arburg Allrounder 370 U 700 100/100 2-component injection moulding machine, which is shown in Figure 33. The machine is composed of two injection units, which enable the injection of two different feedstocks in the same mould.
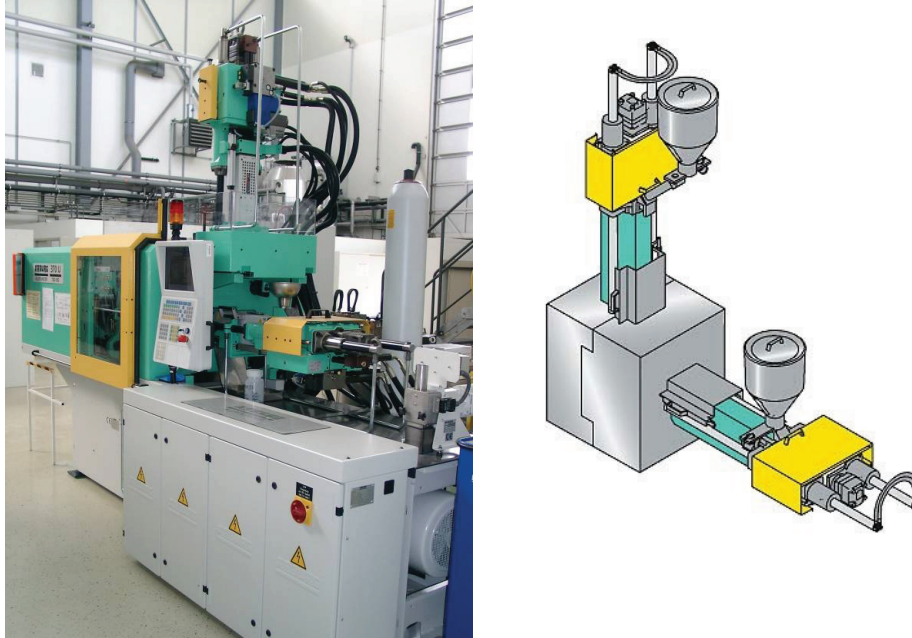
Figure 33: Left: picture of the 2-component MIM-machine used. Right: schematic drawing of the injection units [118].

The moulds used were designed for the investigation of the availability of the combination of feedstocks with and without space holder for the production of parts with a gradient in porosity. Different 2-C-MIM techniques were hereby investigated and these are discussed next. For all methods, injection parameters were optimised as described in [119].

2-C-sandwich-MIM

The first technique investigated is named here 2-component-sandwich-MIM and is schematically shown in Figure 34. It was the technique used for preliminary experiments for the operation of the 2-C-MIM unit. The first mass is injected in the mould cavity by the horizontal injection unit, so that an outer skin is formed. Immediately afterwards the core of the part is formed by the injection of the second mass by the vertical injection unit. A final injection of the first mass, which clears the injection channel for the subsequent shot, ends the cycle.
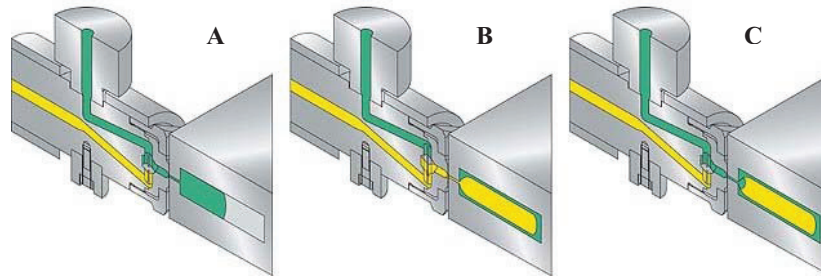
Figure 34: 2-component-sandwich-MIM process. (A): Injection of the mass from the vertical unit. (B): Injection of the mass from the horizontal unit. (C): Second injection of the mass from the vertical unit. [118]

Both feedstocks are hereby injected through a common valve, which controls the separation of both materials. This switch-valve is located inside an interval unit, which is shown in Figure 35. By injection of the first feedstock by the vertical unit, the pressure gradient inside the valve promotes the displacement of an internal small piece, which blocks the second feedstock and allows only the first one to be injected. By injection of the second feedstock by the horizontal unit, the piece is once more displaced by the pressure gradient created and only the second feedstock is injected. A picture of the switch-valve with its internal small piece is shown in Figure 35 as well.
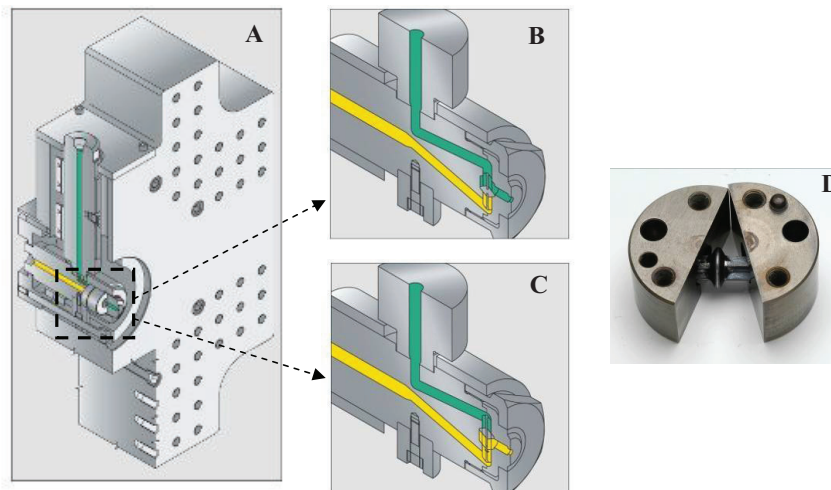
Figure 35: (A) Construction of the interval unit. (B) Injection of the vertical component. (C) Injection of the horizontal component. [118] (D) Photo of the switch-valve with internal piece.

The mould used for the 2-C-sandwich-MIM investigations was a cylinder shape (L = 65 mm, ø = 12 mm). The mould was produced by the company Topic (Solingen) and the geometry of the part is shown in Figure 36.
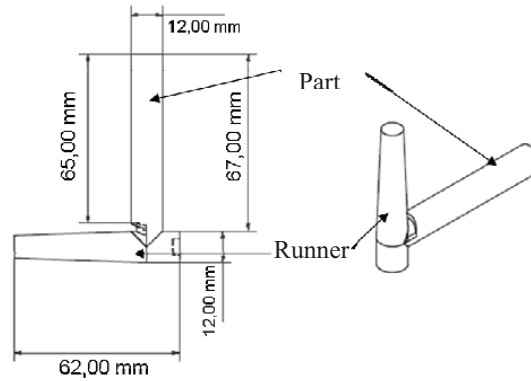
Figure 36: Technical drawing of the MIM-cylinder.

2-C-insertion-MIM

The second approach used to investigate the availability of the production of parts with a gradient in porosity was the 2-C-insertion-MIM, which is schematically shown in Figure 37. By this technique, green parts are produced with removable inlays inside a mould with a cylindrical shape (Ø = 14 mm, L = 28 mm). As a second step, the runner material is removed and the part is inserted in the mould after being rotated by 180°. By injecting the second feedstock in the mould, a green part composed of the two different materials is produced. This technique requires the use of only one injection unit.
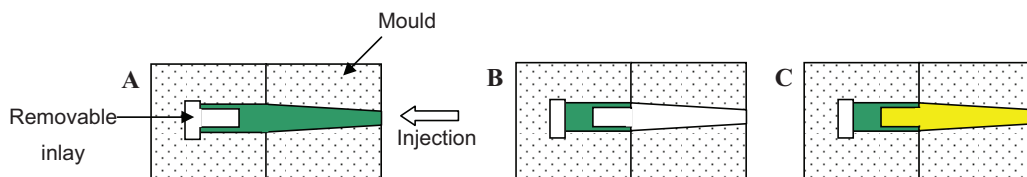
Figure 37: 2-component-insertion-MIM. (A) Injection of the first mass. (B) Insertion of the part in the mould. (C) Injection of the second mass.

By producing removable inlays with different geometries, it is possible to produce parts with different geometries of the porosity gradient. One of the geometries produced is shown in Figure 38 as an example.
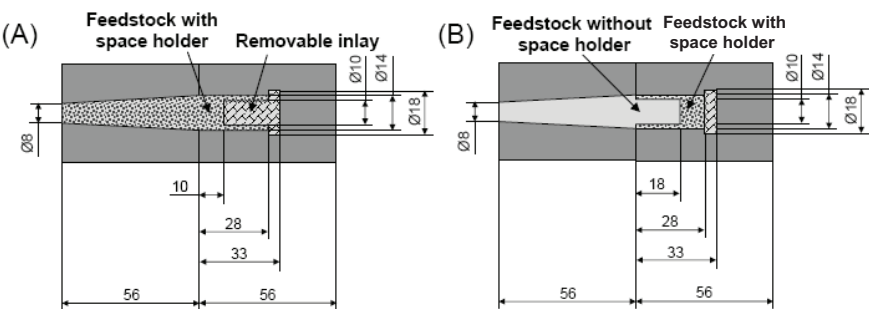
Figure 38: Dimensions of one of the geometries produced by 2-C-Insertion-MIM with the small cylinder mould. (A) Green part produced with the removable inlay. (B) Inlaid green part in the mould.

2-C-MIM with an automated mould

The third approach used to investigate 2-C-MIM was more industrially focused, as a mould with a spinal implant shape was used. The spinal implant of the company Synthes was taken as a model, where the part dimensions were supplied by Synthes. A plastic prototype of the implant was produced to assist mould design, as shown in Figure 39. As mentioned before, this implant is conventionally produced by pressing and machining in the green state [6].
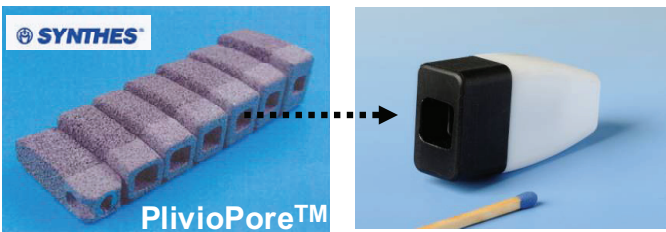
Figure 39: Titanium spinal implant of the company Synthes and its plastic prototype.

The dimensions of the spinal implant produced by 2-C-MIM are as shown in Figure 40. The 2-C-MIM process enables the manufacture of this implant by injection of a feedstock with space holder and a feedstock without space holder in the same mould. A sintering shrinkage

of 10% was taken into consideration, so that the final part meets the dimensions of the final desired product.
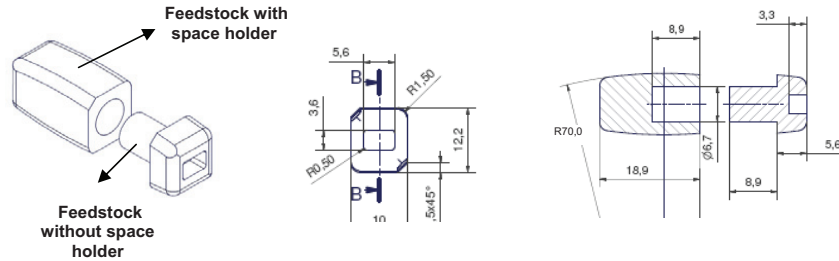
Figure 40: Technical drawing of a spinal implant composed of dense and porous parts for demonstration of the 2-C-MIM process.

In order to produce the spinal implant, a special automated mould was used. The first feedstock (without space holder) is injected through the horizontal unit so that the dense part of the implant is produced. The mould afterwards opens and an inside part is automatically pushed, as it is equipped with a hydraulic pushing system. This displacement of the internal part of the mould makes it possible the second feedstock (with space holder) to be injected and the final green part to be formed. The schematic drawing of the mould used is shown in Figure 41. The mould was produced by the company DIA-Nielsen (Düren).
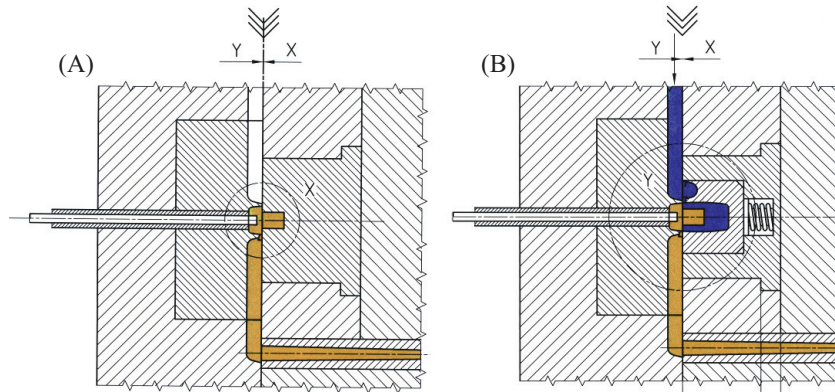
Figure 41: Schematic drawing of the 2-C-MIM mould used for the fabrication of spinal implants.
(A) Injection of the feedstock without space holder. (B) Injection of the feedstock with space holder.

4.1.5   Partial debinding

The partial debinding was performed either by wicking or solvent extraction. In the case of feedstocks produced with the standard binder SB, the method used was wicking. The feedstocks produced with the paraffin-based binder systems were debinded by extraction with n-hexane.

By wicking, the warm pressed green parts were immersed in Al_2O_3-sand (355-500 μm) and heated up in a fan oven at 150°C for 10 hours. These were the standard parameters used, which were already employed in previous studies with this binder system [7]. Nevertheless, if the sample was larger than the warm pressed parts (Ø = 12 mm, H ≈ 10 mm), as it is the case of the parts produced by 2-C-insertion-MIM, the wicking time was increased, as the debinding time is dependent on the square of the part thickness as a first approximation.

By solvent extraction, the samples were immersed in an n-hexane bath. This solvent was chosen due to its reported suitability to dissolve paraffin materials [73, 75]. The bath was heated up by a heating plate in a flat bottom flask. At the top of the equipment, a condenser allowed the evaporated n-hexane to return to the system. The debinding time was investigated as a function of the solvent temperature. The mass loss was determined by weighing the samples before and after the extraction procedure, where the samples were put in a fan oven for 10 hours at 50°C after removal from the hexane bath.

4.1.6   Removal of space holder

The desalination of MIM samples was already investigated [112], where the standard desalination parameters were 60°C bath temperature and 24 hours immersion time of warm pressed samples with 50 Vol.% space holder. These were the parameters used in this work as well.

4.1.7   Thermal debinding and sintering

The thermal debinding and sintering were performed in a furnace of the company Thermal Technologies. The partially debinded and desalinated samples were placed on a Y_2O_3 sintering substrate in a Al_2O_3 crucible. Yttrium oxide is the standard sintering substrate at IEK-1 at *Forschungszentrum Jülich*, as it was shown that its suitability for reactive metals like NiTi was shown in previous studies [113]. The crucible was covered with a porous titanium getter material in order to protect the samples from possible contaminations which

could be in the oven chamber. The positive effect of the titanium getter on the chemical impurity level of NiTi samples was shown in previous studies as well [113].

Inside the oven, there is a molybdenum chamber, in which the sintering crucible is placed. A suction system directs the decomposition products of the thermal debinding from the molybdenum chamber to a cooled chamber. This procedure avoids the condensation of the decomposition products of thermal debinding on the water-cooled walls of the oven.

Before thermal debinding, the oven was evacuated to an absolute pressure of < 0,09 mbar. An argon flow of 10 L/min is afterwards employed to rinse the oven chamber, where a maximal pressure of 14 mbar in the oven chamber is reached. After thermal debinding, the oven was evacuated to high vacuum operation ($<10^{-5}$ mbar). In previous studies [113], the vacuum atmosphere showed itself to be more suitable for maintaining the chemical purity of titanium alloys than reducing atmospheres during sintering, so that vacuum was used for sintering the samples.

During thermal debinding, the samples were heated up to 500°C at 1 K/min heating rate up to 500°C, where the temperature was held for 2 hours. The warm pressed samples were heated up to the sintering temperature of 1300 °C at 5 K/min. These were the parameters used in previous studies [112], which were further evaluated by TGA measurements of the binder components and binder systems. In the case of the spinal implants, sintering temperatures of 1200 and 1300°C were investigated. The dwell time was 3 hours. The samples were afterwards cooled down to room temperature with 5 K/min cooling rate.

4.2 Analysis and measuring methods

4.2.1 Thermogravimetric Analysis (TGA)

TGA measurements were performed in order to investigate the decomposition behaviour of the binder components themselves as well as the binder systems.

The sample is submitted to a temperature program and the weight w is recorded as a function of the temperature or time [120]. The principle of a thermogravimetric curve or (TG curve) is shown in Figure 42 A. A plot of the rate of weight loss (dw/dt) versus temperature is referred as the derivative thermogravimetric curve (or DTG curve) and is shown in Figure 42 B.
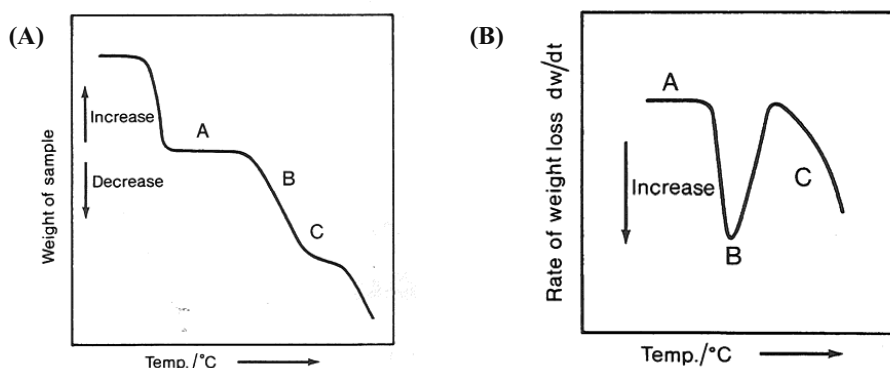
Figure 42: (A) Typical TG curve. (B) Typical DTG curve. [120]

In Figure 42 A, the plateau A indicates constant weight. A curved portion (B) indicates mass loss, the steepness of the curve indicates the rate of loss. These portions are seen in Figure 42 B, where the portion of the DTG curve lying on the line $dw/dt = 0$ is equivalent to the plateau A in the TG curve. The point where the plateau starts to deviate from zero indicates the start of mass loss. The peak of the DTG curve corresponds to the curved portion B on the TG curve with the peak maximum in Figure 42 B (dw/dt_{max}) corresponding to the maximum slope at B in Figure 42 A. The C portion of the TG curve corresponds to an inflection at which once more mass loss is recorded.

In a TG curve of a single stage non isothermal reaction, there are mainly two characteristic temperatures: the initial temperature T_i and the final temperature T_f. T_i is defined as the lowest temperature at which the cumulative weight change can be detected by the thermobalance. The definition of T_f is analogous: T_f is the temperature at which the cumulative weight change first reaches its maximum value. The difference between T_i and T_f is termed the reaction interval. These were detected in this work by plotting the DTG curve and reading the values where the rate of weight changes as described above. The peak temperature of the DTG curve was recorded as well. When two or more peaks were identified, in the case of more component mixtures, these were separately recorded.

The samples were subjected to a heating cycle from room temperature to 1000°C with a 2 hours holding period at 500°C. The decomposition behaviour of the binder components and binder systems could be investigated in this way. The holding period at 500°C was employed in order to investigate if the binder was already decomposed completely at this temperature,

which was employed for the thermal debinding cycle of warm pressed and injection moulded samples as well. The holding period and holding temperature were found to be suitable for the samples with the standard binder system (SB) in previous works [112].

4.2.2 Chemical Analysis

Chemical analysis was performed for the control of chemical impurities in the titanium material. The starting powder, the thermally debinded sample and the sintered sample were analysed. Three to five specimens were analysed pro sample material. All the measurements were undertaken at the *Zentralabteilung für Chemische Analysen (ZCH)* at *Forschungszentrum Jülich*.

The nitrogen and oxygen levels were determined by hot extraction in helium flow with subsequent thermal conductivity measurement for nitrogen and IR-spectroscopy for oxygen. The samples were placed in a graphite crucible inside the equipment LECO TCH 600 in helium flux and heated up by an electrical current. The oxygen of the sample reacts with the carbon of the graphite of the crucible and carbon monoxide (CO) is produced. The nitrogen leaves the samples as N_2 during the process. By thermal conductivity spectroscopy and IR-spectroscopy the levels of respectively nitrogen and oxygen are detected. By this method, the measurement error of the equipment is less than 1%.

The carbon content of the sample was determined by IR-spectroscopy after burning the sample. The sample is placed in a ceramic crucible in the equipment LECO CS 600 and burnt under oxygen flow, resulting in the formation of CO and CO_2. After a cleaning process of the efflux gas, the carbon content is determined by IR-spectroscopy. The measuring error of the equipment is once more less than 1%, according to the producer.

4.2.3 Density measurements

Tap density measurements were performed on powder and space holder/powder mixtures, for assistance on the determination of the optimal binder content of the feedstocks. Density measurements on feedstocks were performed for the same purpose using the Archimedes principle.

The tap density was measured by dropping of the material in a volumetric cylinder. The cylinder was placed on the tapping volumeter STAV 2003 of the company JEL and the machine was allowed to tap for 1000 times. The volume of the powder material was then measured and the tap density (ρ_{tap}) calculated. By comparison to the theoretical density (ρ_{theo})

of the powder material, the percentage of hollow spaces (V_{spc}) in the material was calculated as shown in the formula below:

$$V_{spc} = \left(1 - \frac{\rho_{tap}}{\rho_{theo}}\right)x100 \qquad\qquad \text{Formula 24}$$

The density of the feedstocks with different solid amounts was measured with the same purpose of assisting determination of the optimal binder content, as shown in Figure 19. The weight of the sample was recorded with a Mettler Toledo XS 204 scale outside and immersed in water. The density of the sample was then calculated automatically by the device by using the Archimedes' principle. The calculation of the theoretical density of the feedstock was done by the rule of mixture.

For warm-pressed samples, the green density of the samples was evaluated by two methods. By the geometrical method, the samples were weighted and measured with a sliding calliper and the density calculated by simply dividing the obtained mass by the volume of the sample. The other method used was the Archimedes method with water, as described previously for measurement of feedstock density.

4.2.4 Differential Scanning Calorimetry (DSC)

The Differential Scanning Calorimetry (DSC) was performed in order to determine the melting behaviour of the binder components and binder systems investigated. The method allows the measurement of heat streams in a sample when subjected to a specific temperature program [121].

A crucible with the sample inside and an empty reference crucible are subjected to a same temperature program and the released or absorbed heat amount is recorded. Exothermic and endothermic events as phase changes like melting, vaporisation or crystallisation in the sample lead to a difference in heat flux between the reference crucible and the crucible with the sample. This difference in heat flux occurs as the sample requires less or more heat for respectively exothermic or endothermic processes, as compared to the reference crucible.

Figure 43 shows a typical DSC curve of a polymer material. The onset of melting (T_i) is graphically determined by drawing a baseline on the curve and recording the point where this baseline meets the line of the curve steepness, as shown in the figure. The temperature of complete melting of the material (T_f) is calculated in an analogous way. The peak melting

74

temperature (T_p) is the temperature at which most of the molecules of the material experience the phase transition. Crystallisation temperatures may be calculated in the same way.
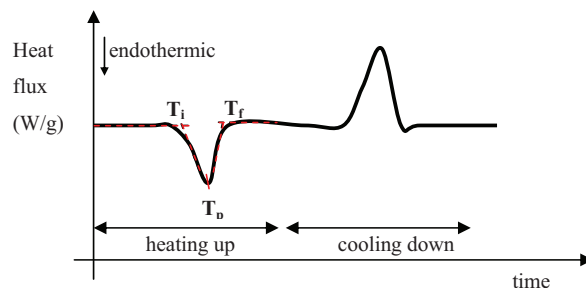
Figure 43: Typical DSC curve.

The temperature program was a heating cycle from 20 to 200°C at 10 K/min and a cooling cycle to 20°C with the same rate. A second heating cycle was performed and this one was used for the evaluation of the melting behaviour of the samples, so that it was sure that all samples had the same thermal history when evaluated.

4.2.5 Light Microscopy (LM)

The sintered samples were subjected to light microscopy (LM) in order to investigate the microstructure of the samples.

The cross-section of the samples was placed in a recipient in an embedding pot of the company Buehler under low pressure (200 mbar). The recipient was then filled in with a resin (Araldit from the company Ciba) and the sample was infiltrated with the material. After 24 hours, the resin was already hard enough to be further processed. The samples were clamped to a sample holder, grinded and polished with the polishing machine Saphir 550 from the company ATM with SiC sandpaper (company Hermes) with different grain sizes up to 4000 under water flow. For the final polishing step, the samples were polished with a very fine polishing cloth from the company Buehler with the same polishing machine with addition of a suspension containing 75 Vol.% SiO_2 suspension (0,1 μm, company Buehler), 20 Vol.% H_2O_2 suspension (company Merck) and 5 Vol.% dishwashing detergent to aid lubrication.

The LM pictures were taken with the microscope PMG3 of the company Olympus with the high definition camera ProgRes 3008 of the company Jenoptik.

4.2.6   Viscosity and torque measurements

The viscosity of binder components, binder systems and feedstocks was determined in order to investigate the flowing behaviour of the materials. The flowing behaviour is a very important issue in 2-C-MIM, as the process deals with feedstocks with particles of very different sizes and a binder system with a suitable viscosity is necessary.

The viscosity of the binder components and binder systems was determined with the rheometer MCR 100 of the company Physica with the cone-plate principle with a 0,048 mm distance between the plate and the substrate and 25 mm plate diameter. The samples were investigated in an up and down shear rate ramp from 0,1 to 1000 s^{-1} at the primary working temperature determined by DSC.

The feedstock viscosity was measured with the twin bore capillary viscometer RH2200 of the company Malvern, shown in Figure 44. As it has a double bore, this equipment allows the simultaneous measurement of the entrance pressure drop, so that the Bagley correction can be directly applied. The Bagley correction takes the entrance pressure drop at the capillary into account for the calculation of the shear stress, as previously discussed. The Rabinowitsch correction can be automatically applied as well, where deviations from the Newtonian behaviour are considered, as also described previously. Both corrections were applied for the results obtained. The results were compared to the uncorrected measurements.
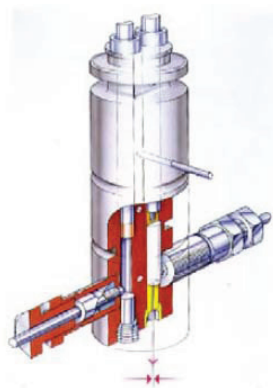
Figure 44: Drawing of the capillary viscometer RH 2200 of the company Malvern.

In order to determine the shear rate range for the capillary measurements, an attempt was made to estimate what would be the maximum shear rate reached at the MIM-machine, when the automated spinal implant mould was used. The maximum shear rates are achieved when

the material flows through the smallest channel in the flowing path, for a same flow rate. The smallest channels through which the feedstocks with and without space holder would go through for the spinal implant mould are the channels directly at the runner gate areas in contact with the implant (1,5 mm x 3,0 mm and 0,8 x 3 mm, respectively). The dimensions of these rectangular channels were different for the feedstocks with and without space holder due to the difference in size between space holder and metal powder particles. The smallest dimension of the runner of the feedstock with space holder was chosen to be at least 2 times larger than the largest space holder particle in the mixture, so that blocking of this channel would be avoided.

The maximum shear rate through a rectangular channel can be calculated with the formula [122]:

$$\dot{\gamma} = \frac{6Q}{wh^2} \hspace{4cm} \text{Formula 25}$$

where Q is the volume flow rate, w and h are the width and the height of the rectangular channel, being h the smallest dimension.

The typical flow rate for PIM is reported to be around 1.5 cm^3/s [38], but variations are always possible depending on feedstock characteristics, mould design, etc. Therefore, a broader range of flow rates up to 6 cm^3/s is going to be used for approximations regarding shear rate.

Using the formula above and considering that and that the maximum volume flow rate reached to be about 6 cm^3/s , the results obtained are 18,750 s^{-1} for the feedstock without space holder and 5,333 s^{-1} for the feedstock with space holder. The maximum shear rate is of course lower in the case of the feedstock with space holder, as the channel in this case is larger than in the case of the feedstock without space holder.

The shear rate achieved during a measurement with the capillary viscometer depends on the die chosen to run the experiment as well as the piston speed. Table 7 summarizes what is the maximum shear rate which would be achieved with a specific die at different piston speeds with a bore diameter of 24 mm, which is the bore diameter of the equipment used.

Table 7: Maximum shear rates achieved as a function of the die diameter and piston speed [123].

Die diameter (mm)	Speed (mm/min)				
	0.1	1.0	10	100	500
0.5	61.4	614	6,144	61,440	307,200
1.0	7.68	76.8	768	7,680	38,400
2.0	0.96	9.6	96	960	4,800

From the shear rate ranges calculated and the maximum shear rates achieved with the capillary dies, the measurements were performed with the 2.0 and 1.0 mm diameter dies for the feedstocks with and without space holder, respectively. The capillary lengths used were respectively 32 and 16 mm. Orifice dies with 0.26 mm length were placed in the second bore of the equipment. Orifice dies and capillaries with the same diameter were used for the same measurement all times.

After placing the adequate die in the equipment, the feedstock material was fed in both bores and allowed to heat up for 15 minutes. The pistons were then moved downwards, so that it was sure that the feedstock material was inside the capillary die. The measurement was immediately afterwards started. The shear rate was stepwise increased by increasing the piston velocity step by step, in an up and down shear rate ramp. The maximum shear rate was 4,000 and 20,000 s^{-1} for feedstocks with and without space holder, respectively. Although a broader shear rate range (until 5,333 s^{-1}) was aimed for feedstocks with space holder, preliminary experiments showed that 4,000 s^{-1} was the maximal shear rate possible to be measured for these feedstocks. The shear stress was automatically recorded and the viscosity automatically calculated by the equipment. Bagley and Rabinowitsch corrections were automatically applied and compared to uncorrected values. The first experiments were conducted at 150°C. The temperature was varied further for selected feedstocks. The temperature was measured at the bore wall by three thermocouples positioned at different locations at the bore wall.

Additionally to the viscosity measurements on binder and feedstock, torque measurements of the feedstock were also performed, in order to assist the determination of the binder content.

The torque measurements were performed with a Rheomix 3010 p / Rheocord 300 p torque rheometer of the company Haake. The mixing chamber was heated to the working temperature. The measurement was started with 45 Vol.% binder content and feedstock was removed and powder material added, so that the solids content was increased at each step. The

volume of the removed feedstock and the volume of powder added were the same. After adding the powder material, the feedstock was allowed to homogenise for 30 minutes before the recording of the torque measurement was initiated. For each step, an average torque and its standard deviation were calculated. The procedure was repeated until the mixing torque could not be measured anymore due to the increase in viscosity of the material. The experiments for torque measurements were conducted at 150°C. The temperature was measured by a thermocouple inside the mixing chamber.

5 Results

5.1 Preliminary 2-C-MIM experiments with the standard binder system

As a preliminary experiment to determine the potential as well as the challenges of the 2-C-MIM process when dealing if the production of net-shaped titanium parts with a gradient in porosity, titanium feedstocks with and without space holder (Ti SB SH and Ti SB, respectively) were injection moulded with the 2-C-insertion-MIM and 2-C-sandwich-MIM techniques.

For these preliminary works, the standard binder system SB was employed. This binder system was developed in the institute IEK-1 at *Forschungszentrum Jülich* in the early 1990s [110, 111] and was recently used for the production of net-shaped NiTi with [112] and without [113] space holder particles by metal injection moulding.

In a first approach, titanium feedstocks with and without space holder particles were produced with the standard binder system SB and simple shaped parts with a gradient in porosity were produced by 2-C-insertion-MIM and 2-C-sandwich-MIM. Results of these preliminary experiments are given in this chapter. They show that there is a strong need for the development of a new feedstock system if fully automated 2-C-MIM production of complex-shaped parts with a gradient in porosity is aspired.

5.1.1 Results of 2-C-insertion-MIM

The 2-C-insertion-MIM was performed with removable inlays with different geometries. Just the horizontal unit of the injection moulding machine was used. The feedstock with space holder was injected first and, after replacing the feedstock and inserting the green parts in the mould, the second feedstock was injected. The injection parameters were taken from previous works with this binder system [112] and are summarised in Table 8.

Table 8: Injection parameters used for the injection of the feedstocks Ti SB and Ti SB SH for the small cylinder mould.

Feedstock charging			Temperature						
Screw rotational velocity (U/min)	Charging volume (cm^3)	Decompression volume (cm^3)	Zone					Nozzle	Mould (°C)
			1 (°C)	2 (°C)	3 (°C)	4 (°C)		5 (°C)	
64	9,15*	3	100	130	141	143		145	45

Injection pressure (bar)	Compression pressure				
	1 (bar)	2 (bar)	3 (bar)	4 (bar)	Total compression time (s)
1000	800	650	500	100	3,6

* For half cylinder shape.

The parts were afterwards debinded by wicking, desalinated in water and sintered (1300°C, 3 h, vacuum). The cross-sections of the sintered parts obtained are shown in Figure 45.
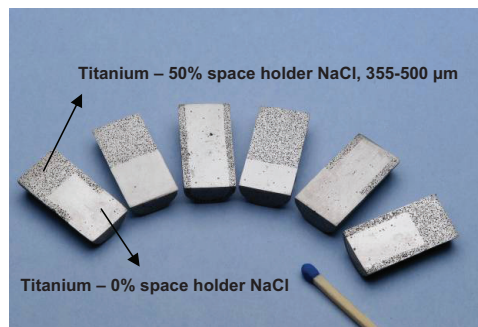
Figure 45: Cross-sectioned sintered samples produced by 2-C-insertion-MIM. Sintering parameters: 1300°C, 3 h, vacuum.

With the different inlays, it was possible to obtain parts with a stepwise gradient in porosity in different geometries. The average sintered radius of all samples (15 parts of different geometries) was 12.59 mm with a standard deviation of 0.08 mm, which means that the deviation of these samples was less than 0.7%. Considering the radius of the green parts of 14.18 mm, a shrinkage of approximately 11% took place.

Microstructure examinations (Figure 46) showed that a well-defined interface between porous and dense areas is present. The microstructure of the porous part is typical for the space holder method, with very well defined pores homogeneously distributed.
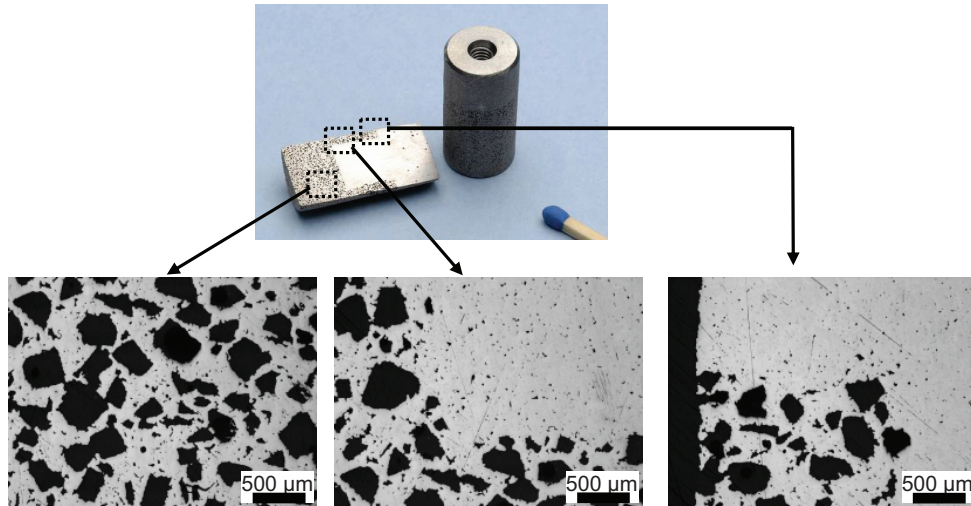
Figure 46: Light microscope pictures of one of the graded samples, showing the porous microstructure and the interface regions between porous and dense areas. Sintering parameters: 1300°C, 3 h, vacuum.

5.1.2 Results of 2-C-sandwich-MIM

After checking the availability of the 2-C-insertion-MIM method, the 2-C-sandwich-MIM technique was investigated. The same titanium feedstocks, Ti SB and Ti SB SH, were fed to the horizontal and vertical injection units, respectively. The parameters used for injection are were the same as described in Table 8, except for the charging volumes, which were in this case 4,39 cm^3 for the feedstock with space holder and 13,90 cm^3 for the feedstock without space holder.

During the injection moulding process, difficulties aroused and the process could not be undertaken continuously. Binder-powder separation was noticed on the vertical nozzle and on the inlet areas of the interval unit, as shown in Figure 47. A binder skin was noticed inside the switch-valve as well, as shown in the figure. The vertical injection unit was clogged and the feedstock could not flow out of the injection unit after some injection shots.

The phase separation of the feedstocks with the standard binder system was thought to be caused by the very low viscosity of this system. Binders with very low viscosity tend to separate from the powder material when subjected to sharp direction changes [38], as seen in the interval unit. The powder is denser and has greater inertia, and sharp corners in the flow

path induce binder and powder to follow different directions. Probably the 90° bends inside the switch-valve induced the separation. The sudden decrease in flow cross-section inside the switch-valve, as it partially blocks the passage of the material, may also have contributed to the phase separation. As a consequence, the viscosity of the feedstock tends to infinity (Figure 21) if the solids loading is pushed beyond the critical point, what hinders material flow and leads to clogging of the equipment.
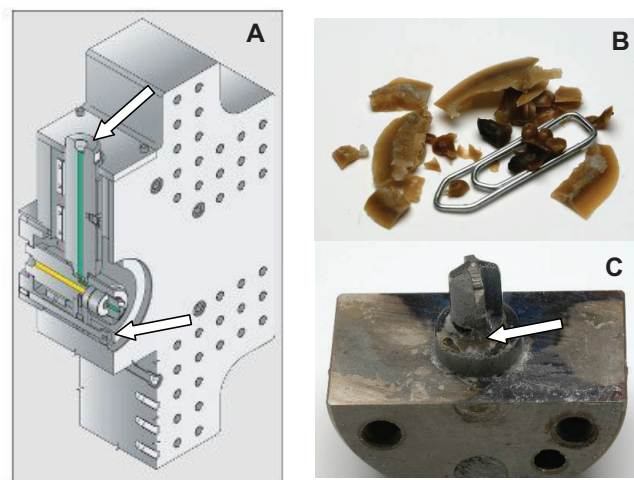
Figure 47: (A) Construction of the interval unit with the switch-valve [118]. The arrows indicate the locations where the separated binder was found. (B) Binder separated from powder found at location indicated. (C) Detail of the binder skin on the switch-valve.

Although the injection process was interrupted due to clogging after some cycles, some green parts were obtained, in which the feedstock with space holder formed the outer skin and the feedstock without space holder formed the core of the part. The green parts obtained were debinded, desalinated and sintered (1300°C, 3 h, vacuum). The microstructure of the sintered part is shown in Figure 48.

Similar to the samples produced by 2-C-insertion-MIM, a very well defined interface between dense and porous areas was achieved with a very well-defined interface between skin and core is clear. A shrinkage of about 12% took place in this case.
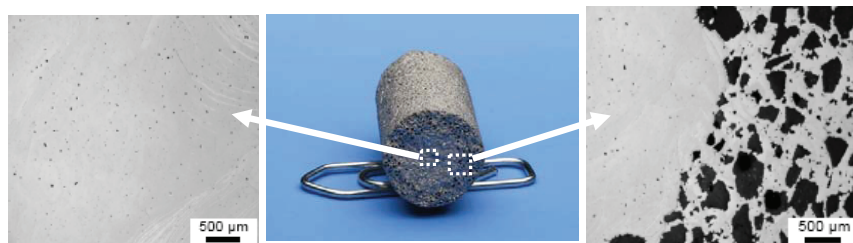
Figure 48: Titanium sintered sample produced by 2-C-sandwich-MIM. Sintering parameters: 1300°C, 3 h, vacuum.

5.1.3   Discussion of preliminary results

The feedstocks with the standard binder system showed themselves to be suitable for 2-C-MIM if the mould geometry used is relative simple. If sharp direction changes and decrease in flow cross-sections are present, strong difficulties in moulding arise due to phase separation. The use of the vertical injection unit was difficult as well, as the injection unit itself was clogged after some cycles.

Based on the results of the preliminary studies, it was concluded that a new binder system needs to be developed for successful application of the 2-C-MIM technique. The standard binder SB does not fulfil the requirements for a suitable binder system for the application, which were listed in Section 3. This binder does not show suitable flowing behaviour for the aimed application of this work and the partial debinding method (wicking) does not have practical relevance to industry. The new binder needs to be more stable regarding phase separation, so that a continuous 2-C-MIM process can be carried out and another partial debinding method must be employed.

5.2   Development of a new binder system for 2-C-MIM parts with a gradient in porosity

For the development of a new binder system suitable for the 2-C-MIM application, three new systems (BS 1, BS 2, BS 3) were investigated as the basis of the new development. As discussed in section 4.1.1, feedstocks produced with these binder systems are debinded via solvent extraction and cover a wide range of component viscosities.

After characterisation of the starting powder and binder materials, feedstocks with the three new binder systems and with the standard binder system SB were produced with and without space holder particles. Taking the standard binder system SB as a reference, the solids loading

and the space holder content (in the case of feedstocks with space holder) were the same as used in previous works [112] and kept constant for these feedstocks. Samples were warm-pressed, debinded, desalinated and sintered. The samples were characterised and evaluated for the further development, where the flowing behaviour of feedstocks was additionally investigated and taken into account. The system with the most promising characteristics was chosen for further investigations, where the solids loading was optimised and influences of stearic acid addition (system BS 4) and of binder component ratio (system BS 5) were evaluated. The most promising feedstocks were chosen for further development steps.

5.2.1 Characterisation of powders and space holder

The investigated powders and space holder were subjected to particle size analysis and scanning electron microscopy (SEM). The particle size distribution is shown in Table 9 and the result lies within the range specified by the producers. A significant grain size difference between metal powders and space holder is evident. The particle size distribution of the Fe22Cr- and the Ti-powder lays within a similar range, so that a transfer of viscosity measurement results from Fe22Cr to Ti powders is expected.

Table 9: Particle size distribution of the investigated powders and space holders.

Material	Particle size range	Manufacturer	Batch	d_{10} (µm)	d_{50} (µm)	d_{90} (µm)
Fe22Cr	20-53 µm	HC Starck	15779	18	34	43
Ti (Grade II)	< 45 µm	TLS	1071/3	8	20	37
NaCl	355-500µm	AppliChem	8 O 010051	172	348	612

The SEM pictures of the Fe22Cr- and the Ti-powder are shown in Figure 49. Although the predominant shape is round, inhomogeneities and satellites (sticking of small particles on the surface of coarse ones) are clearly present for both powders. Such deformations may have an influence on the flowing behaviour of the feedstock, on the green density of samples, as well as on their sintering behaviour.
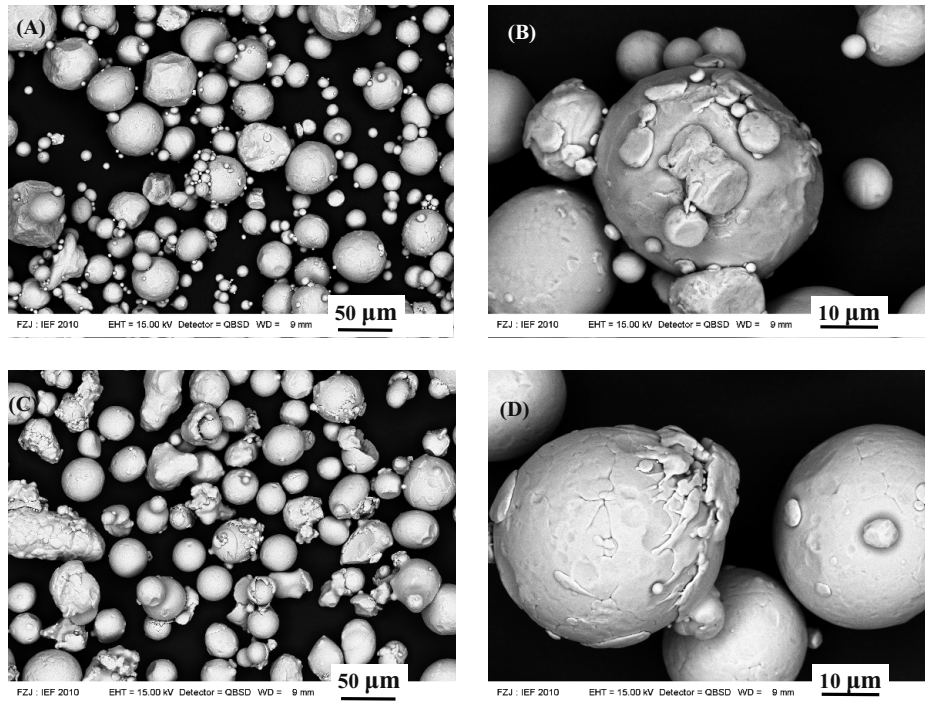
Figure 49: (A) and (B): SEM pictures of the Ti-powder. (C) and (D) SEM pictures of the Fe22Cr-powder.

The SEM picture of the NaCl particles are shown in Figure 50, where a picture of the NaCl particles together with the Ti-powder particles is shown as well. The NaCl particles are roughly square and much larger than the metal powder. These differences in size and shape are likely to influence flowing behaviour of the feedstock.
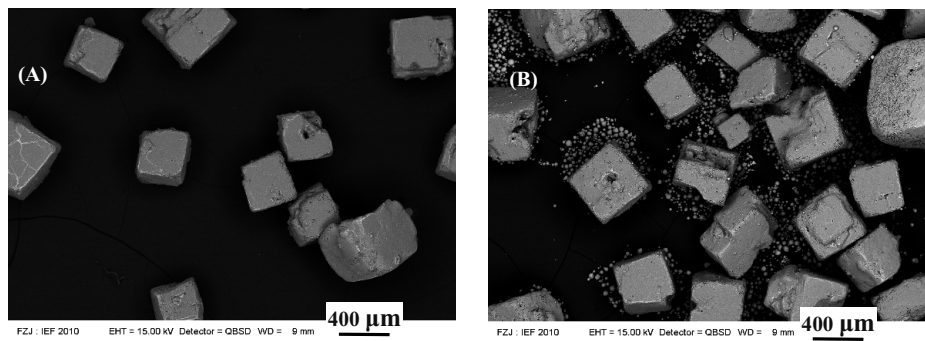
Figure 50: (A) SEM picture of the NaCl particles. (B) SEM picture of the NaCl particles together with the titanium powder.

The chemical analysis results for the titanium powder are shown in Table 10. The composition is within the ISO 5832-2 limit range for titanium grade 2 (C <0.08 wt%, O <0.25 wt%, N <0.05 wt%).

Table 10: Chemical analysis results for the titanium powder used.

Material	Particle size range	Manufacturer	Batch	C (wt %)	O (wt %)	N (wt %)
Ti (Grade II)	< 45 μm	TLS	1071/3	0.01	0.18	< 0.001

5.2.2 Characterisation of binder components and binder systems

For the preliminary experiments with warm pressed samples with the standard binder (SB) and the paraffin-based binder systems BS 1, BS 2 and BS 3, the respective binder components and binder systems were analysed by DSC, TGA and rotational viscosimetry. All curves are shown in Table 11 and Table 12.

The DSC curves shown are derived from the second heating cycle. It is clear that the melting peaks of the single components are present in the binder systems investigated. The initial (T_i), peak (T_p) and final (T_f) melting temperatures were recorded and are shown in Table 13 (binder components) and Table 14 (binder systems). Table 15 shows the differences in the peak melting temperature for the single component measured alone and the component characteristic peak in the binder system. The peak displacement is defined here as the difference between these peaks.

When no significant peak displacement exists, as it is the case for the SB system, there is an indication that the components are mainly not soluble in each other. The melting peaks of the paraffin-based systems show peak displacement, which indicates phase interaction. The most significant displacements are seen for BS 2 and BS 3, reaching up to 16°C in the case of BS 3. It is described in the literature [121] that polymer binary systems are normally mixtures that split into two metastable phases, in which both component materials are present. Displaced melting temperatures suggest that the materials are present in either phases and change therefore its characteristics. Phase equilibria diagrams of binary systems show this behaviour [124].

Due to the melting peak displacements observed for the paraffin-based systems, it was concluded that a working temperature of 150°C would be high enough for preliminary experiments regarding feedstock preparation and characterisation. Further optimisation of the

working temperature was conducted after capillary measurements, as will be described later. The same working temperature was chosen for experiments with the standard binder (SB), as it was found to be suitable in previous works as well [112].

Table 11: DSC, TGA and viscosity curves of the binder components and binder systems SB and BS 1.
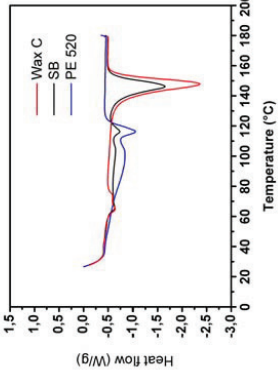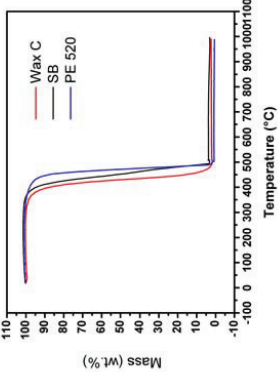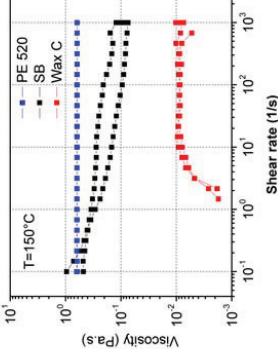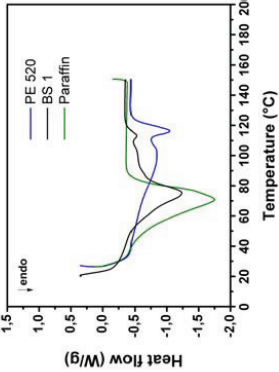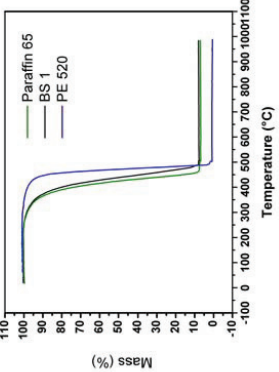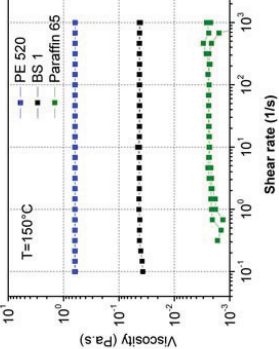
	DSC	TGA	Viscosity
Standard binder (SB)			
BS 1			

Table 12: DSC, TGA and viscosity curves of the binder components and binder systems BS 2 and BS 3.

	DSC	TGA	Viscosity
BS 2			
BS 3			

Table 13: Initial (T$_i$), peak (T$_p$) and final (T$_f$) temperatures of the curves of the second heating of DSC for the binder components.

	T$_i$	T$_p$	T$_f$
Paraffin 65	-	71.0	93.7
PE 520	-	116.7	130.2
PE 190	87.8	138.7	156.7
Hostalen GA 7260 G	85.8	141.2	158.5
Wax C	113.4	147.6	163.2

Table 14: Initial (T$_i$), peak (T$_p$) and final (T$_f$) temperatures of the curves of the second heating of DSC for the binder systems.

	T$_i$	T$_p$	T$_f$
SB (1st peak)	-	116.4	-
SB (2nd peak)	-	146.3	163.1
BS 1 (1st peak)	-	75.3	-
BS 1 (2nd peak)	-	113.4	127.3
BS 2 (1st peak)	-	79.5	-
BS 2 (2nd peak)	-	125.8	142.4
BS 3 (1st peak)	-	72.7	-
BS 3 (2nd peak)	-	125.1	136.0

Table 15: Displacements of the temperature of the melting peak (T$_p$) of the DSC curves.

	Degrees (°C)
SB (1st peak)	-0.3
SB (2nd peak)	-1.3
BS 1 (1st peak)	+4.2
BS 1 (2nd peak)	-3.3
BS 2 (1st peak)	+8.5
BS 2 (2nd peak)	-12.9
BS 3 (1st peak)	+1.6
BS 3 (2nd peak)	-16.1

The results of the TG analysis indicate the temperature for thermal decomposition of the binder components and binder systems. The initial (T$_i$), maximum loss rate (T$_{dw/dt}$) and final (T$_f$) temperatures are shown in Table 16 (binder components) and Table 17 (binder systems). All binder components and binder systems are already decomposed before 500°C or during the 500°C holding period. This shows that probably all binder materials are decomposed at this temperature during the thermal debinding cycle used for the warm pressed and injected

samples. Nevertheless, it is likely that the powder material has a catalytic effect on binder decomposition, as it was previously described in other studies [82]. In the case of the binder systems SB, BS 2 and BS 3, two peaks of the temperature of maximum loss rate ($T_{dw/dtmax}$) were recognised, which are related to the decomposition of the binder components in the system. For the system BS 1, only one broader peak was present, indicating that the decomposition of the binder components is more overlapped in this case as compared to the other systems.

Table 16: Initial (T_i), temperature at maximum loss rate ($T_{dw/dtmax}$) and final (T_f) temperatures of the TG curves for the binder components.

	T_i (°C)	$T_{dw/dtmax}$ (°C)	T_f (°C)
Paraffin 65	205.0	440.4	489.2
PE 520	334.5	475.7	500*
PE 190	391.7	472.1	484.1
Hostalen GA 7260 G	389.7	475.1	487.1
Wax C	284.9	434.8	500*
Stearic acid	-	319.5	465.5

*during holding period.

Table 17: Initial (T_i), maximum loss rate ($T_{dw/dtmax}$) and final (T_f) temperatures of the TGA curves for the binder systems.

	T_i (°C)	$T_{dw/dtmax}1$ (°C)	$T_{dw/dtmax}2$ (°C)	T_f (°C)
SB	300.3	442.0	475.5	500*
BS 1	221.1	446.3		500*
BS 2	227.7	418.3	485.2	500*
BS 3	229.1	412.3	477.3	500*

*during holding period

The viscosity values for binder components and binder systems are shown in Table 18. Paraffin wax and the amide wax (Wax C) are the less viscous components. Among the polyethylene waxes, PE 520 is around ten times less viscous than PE 190. Hostalen GA 7260 G is the most viscous material investigated. As the first components of the binder systems have comparable viscosities, the final viscosity of the binder system is mainly dictated by the viscosity of the second component. Systems with more viscous second components are more viscous than systems with less viscous second components. The system BS 3 exhibits a viscosity value which is the closest to the value proposed in the literature (10 Pa·s [38]) among the binder systems studied.

Table 18: Viscosities at 150°C.

Binder components / Binder systems	η (Pa.s) at $\gamma = 100$ s^{-1}
Wax C	0.012
Paraffin 65	0.002
PE 520	0.62
PE 190	14.9
Hostalen GA 7260 G	308
SB	0.15
BS 1	0.04
BS 2	0.53
BS 3	12.4

According to German [38], the viscosity of a binder system may be estimated by the following equation:

$$\ln(\eta_B) = \sum_i w_i \ln(\eta_i)$$ Formula 26

where:

η_B is the viscosity of the binder system

w_i is the weight fraction of the component i

η_i is the viscosity of the component i

The viscosity values of the measurements and the expected values calculated with Formula 26 from the values of the single components (Table 18) are shown in the table below:

Table 19: Measured and calculated values for viscosity of the binder systems.

	SB	BS 1	BS 2	BS 3
Measured binder viscosity (Pa.s)*	0.15	0.04	0.53	12.4
Binder viscosity calculated (Pa.s)**	0.05	0.02	0.06	0.19

* at 150°C, $\gamma = 100$ s^{-1}.

** calculated from viscosities of single components, measured at 150°C, $\gamma = 100$ s^{-1} (Table 18).

It seems that Formula 26 does not predict the viscosity of the binder systems studied in this work. Large deviations from the measured viscosity are seen. Formula 26 was originally proposed by Arrhenius and latter modified by Kendall [125]. The formula is valid for binary mixtures of ideal liquids, where the composition is actually expressed in volume (Arrhenius) or molar fraction (Kendall). The formula does not apply to binder systems which are not close to the ideal solution behaviour, where molecules with very similar nature are involved. The large difference in molecular weight of the binder components involved (section 2.5.1) strongly contributes to the deviation from an ideal behaviour of the system. Mixtures composed of materials with very different physical constants are already reported to deliver great deviations from values predicted by the formula proposed [126].

5.2.3   Warm pressing and green density

The Ti-feedstocks Ti SB, Ti SB SH, Ti BS 1, Ti BS 1 SH, Ti BS 2, Ti BS 2 SH, Ti BS 3 and Ti BS 3 SH were warm pressed. During warm pressing, it was noticed that, already in this simple experimental set up, a slight binder-powder separation took place for the feedstocks with the standard binder (SB) and with the BS 1 system. When the sample was taken out of the form, separated binder could be seen on the die wall and on the pressing plunger. Both binder systems are characterised by their low viscosity. This behaviour was not observed for the samples with the systems BS 2 and BS 3.

The green density of the samples was evaluated by the geometrical and the Archimedes method. As paraffin, polyethylene and Wax C are not soluble in water [59, 127], the measurements with the Archimedes method were carried out without problems for the samples without space holder. It was assumed that the samples were intact after the measurement and could be further used. The results are shown in Figure 51. The theoretical density was calculated by the rule of mixture.
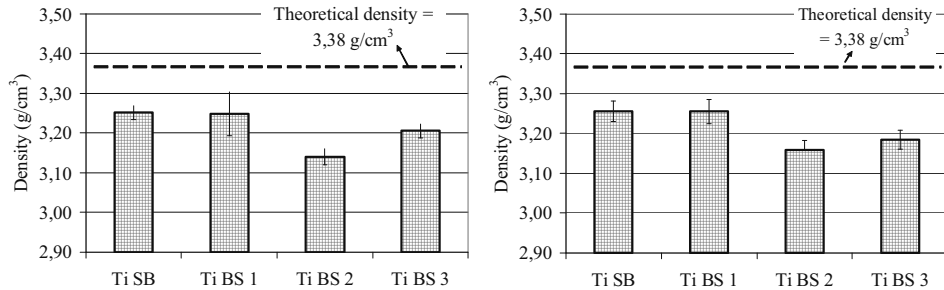
Figure 51: Green density of the samples without space holder, geometrical method (left) and Archimedes method (right) (n=8). Pressing parameters: 110 MPa, 150°C.

All samples exhibit a lower density than the theoretical green density of the feedstock (3,38 g/cm^3). It seems that the mixture does not pack to full density and inevitability voids are formed during the process.

It can be seen that the samples of the standard binder SB and the BS 1 samples tend to have a slight higher green density than the samples of the systems BS 2 and BS 3. This tendency was confirmed by both measurement methods. A possible reason for the slight higher green density of the SB and BS 1 samples is a different wetting behaviour of binder on the particles. The effect of fluid dynamics on wettability has been described in the literature [128]. The final spread of the liquid on a solid substrate is dependent on liquid viscosity and can be mainly attributed to viscous dissipation effects. The viscous dissipation is proportional to the liquid viscosity and a droplet with higher viscosity must overcome more dissipation energy during its spreading process, so that it spreads less than less viscous materials on the same substrate. It is possible that the standard binder SB and the BS 1 binder, being less viscous, wet better on the particle surface and less voids are formed than in the case of BS 2 and BS 3. It is likely that if the pressing parameters are optimised and the pressure employed is increased, the green density of the samples is increased. In this case, more energy would be employed to overcome viscous dissipation effects of the binder materials.

The samples with space holder were measured only with the geometrical method, as it was probable that either NaCl would dissolve in water or the binder components would dissolve in nonpolar solvents [127]. But as both measurement methods showed comparable results for the samples without space holder, it is assumed that the results of the geometrical method are

sufficient for the characterisation of the green density of the samples with space holder. The results are shown in Figure 52 below:
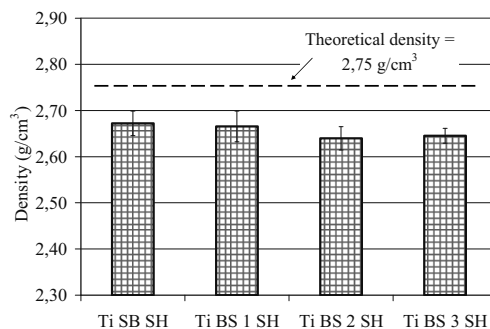
Figure 52: Green density of the samples with space holder, geometrical method (n=8).Samples with 50 Vol.% space holder. Pressing parameters: 110 MPa, 150°C.

The samples with space holder show the same tendency as the samples without space holder. The feedstocks with the SB and BS 1 systems exhibit a slightly higher green density as compared to BS 2 and BS 3 samples. All samples have a lower density than the theoretical value. The reasons for these observations were already discussed above.

5.2.4 *Partial debinding*

The first step of debinding was investigated for the samples with the systems SB, BS 1, BS 2 and BS 3, with and without space holder. For the SB binder, the wicking process was investigated. For the paraffin-based systems, solvent debinding in hexane was performed.

The mass loss of the samples was recorded after various debinding times. Assuming that only binder material is removed during the process, the binder loss was plotted against the debinding time and is shown in Figure 53. The percentage of binder loss was calculated taking into account the theoretical binder amount in the feedstock.
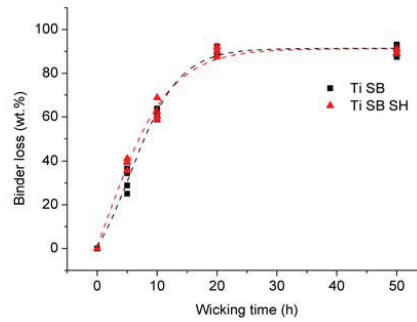
Figure 53: Debinding curves for the feedstocks with the standard binder system SB. Debinding was done by wicking in Al$_2$O$_3$ sand.

In the case of the standard binder SB, it seems that around 90 wt.% of the total binder content is removed if the process is run for 20 hours or more (Figure 53). This is probably due to the fact that both binder components are molten at the wicking temperature of 150°C. The first binder component (Wax C), which has to be removed during the first stage of debinding and represents 60wt% of the total binder content, has a higher melting point than the second component (PE 520) of this system. As both components are molten during wicking, probably they are both extracted by capillary forces during the process, so that 90 wt.% of the total binder content is removed. This is actually not usual, as normally only the first binder component should be extracted during the first stage of debinding. The samples which were further processed (desalination and sintering) and characterised were wicked for 10 hours, as the standard processing parameters used in previous works with this binder system [112].

The influence of the solvent temperature was investigated for the system BS 1. Figure 54 shows the samples with and without space holder subjected to 25 and 50°C debinding temperatures.
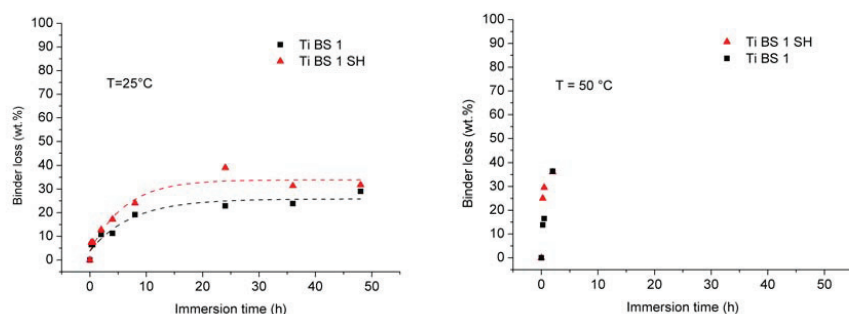
Figure 54: Solvent debinding curves for the feedstocks with the binder system BS 1 at 25 and 50 °C.

In the case of solvent extraction for the system BS 1, around 30 wt.% of binder loss is recorded for extraction at 25°C even after 48 hours. That mass loss is much less than the theoretical amount of paraffin in the binder system (62 wt.%), which was expected to be extracted by the solvent. It seems that higher temperatures than 25 °C have to be employed for complete extraction of paraffin. In the case of the extraction at 50°C, the process is faster for the first hours of debinding. This is already expected, as predicted by Formula 1. Nevertheless, the samples did not withstand longer contact with hexane and were broken off, so that no reliable values for mass loss could be recorded for periods longer than 2 hours.

The debinding curves for the systems BS 2 and BS 3 are shown in Figure 55. In this case, extraction was performed at 50°C, due to the faster debinding as compared to 25°C as seen for BS 1 samples. The samples could withstand the contact with solvent and did not break off in the hexane bad, except for Ti BS 2 at debinding times longer than 36 hours.
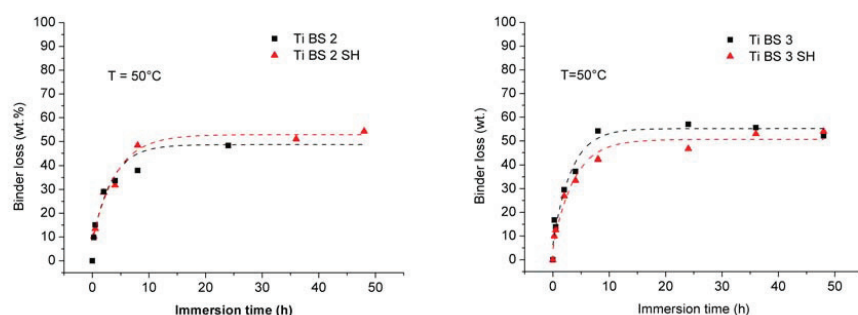
Figure 55: Solvent debinding curves for the feedstocks with the binder system BS 2 and BS 3 at 50 °C.

For the system BS 2 and BS 3, the samples loose around 50 wt.% of binder after 48 hours debinding at 50°C (Figure 55). Probably only paraffin is removed during the extraction and PE 520 remains in the samples, as paraffin is soluble in hexane and polyethylene is not.

For all systems investigated, it seems that there is no relevant difference between the solvent extraction of the first binder component in the samples with or without space holder.

The density of the samples was measured by the geometrical method after the first debinding step. The same tendency as for the green bodies is present for the partially debinded samples. As seen in Figure 56, the SB and BS 1 samples show a slight higher density than the BS 2 and BS 3 samples. This effect is related to the slight higher green density of the samples SB and BS 1.
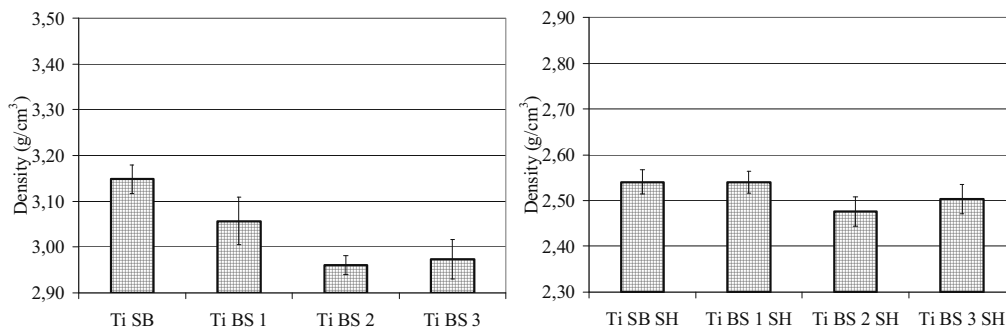
Figure 56: Density of the samples with (right) and without space holder (left) after the first debinding step (n=7). Extraction parameters: 50°C, hexane, 48 h. Wicking parameters: 150°C, Al$_2$O$_3$ bed, 10 h.

The linear change in height and diameter of the samples with respect to the green bodies was recorded. The dimensional change in height (Figure 57) is much more pronounced than the change in diameter (Figure 58). The samples with the paraffin-based systems tend to exhibit a small height expansion, in contrast to the SB samples, which show negligible dimensional change. It seems that there is an influence of the second component used in paraffin-based systems on the height expansion of the samples after debinding. The BS 3 samples, both with and without space holder, show the highest expansion, followed by BS 2 samples. The BS 1 samples expand less than the BS 2 and BS 3 samples. According to the literature [74], the dimensional change during solvent debinding takes place in two stages, where the first swelling stage is due to the swelling of paraffin and the second stage due to the swelling of the insoluble polymers. The polymer material Hostalen GA 7260 G and PE 190 seem to be more sensitive to swelling than PE 520. Additionally to the swelling of the binder

components, it is possible that the voids inside the green body may have acted as stress concentrators and led to the formation of larger voids inside the sample. That would be one of the reasons why the BS 2 and BS 3 samples, which have lower green density as compared to BS 1 samples (Figure 51 und Figure 52), exhibit the higher expansion after solvent debinding.
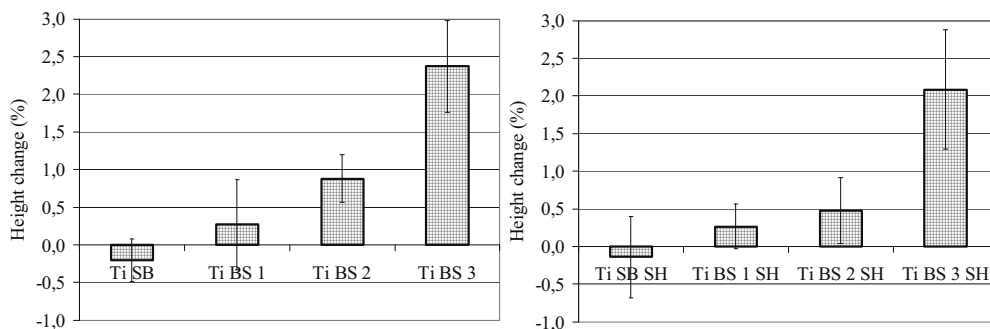
Figure 57: Linear change in height of the samples with (right) and without (left) space holder after the first debinding step (n=7). Extraction parameters: 50°C, hexane, 48 h. Wicking parameters: 150°C, Al$_2$O$_3$ bed, 10 h.
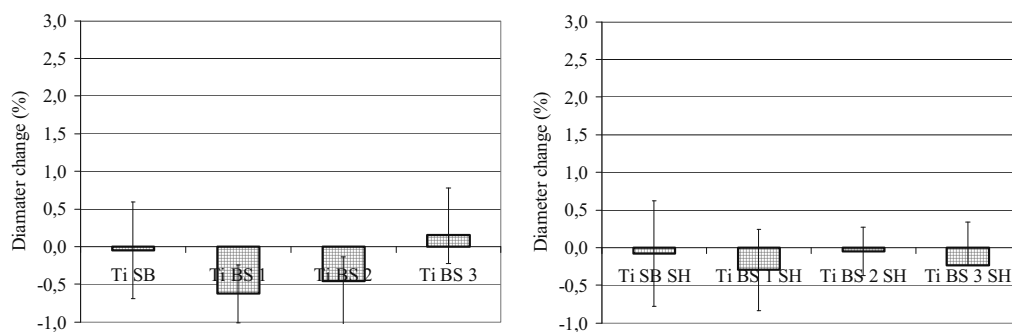
Figure 58: Linear change in diameter of the samples with (right) and without (left) space holder after the first debinding step (n=7). Extraction parameters: 50°C, hexane, 48 h. Wicking parameters: 150°C, Al$_2$O$_3$ bed, 10 h.

Although the swelling is less pronounced for the samples with PE 520 and PE 190 materials, it was observed that some of theses samples were partially broken off during immersion in n-hexane, as mentioned previously. One broken-off sample is shown in Figure 59 A. This effect was more pronounced for BS 1 than for BS 2 samples. Another defect observed was the

formation of cracks at the surface of some samples after the solvent extraction process. This effect was observed mainly for the BS 3 samples.
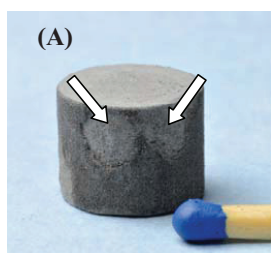
Figure 59: (A) BS 1 sample after solvent debinding. Broken off parts are shown by the arrows.

5.2.5   Desalination

After the partial debinding, the samples with the space holder were further desalinated in water bath at 60°C. After 24 h desalination, the samples were taken out of the water bath and the mass loss determined, in order to check if all NaCl was removed. After 24 h, the samples of the feedstocks Ti SB SH and Ti BS 1 SH showed 100 wt% NaCl loss. On the other hand, the samples of the feedstocks Ti BS 2 SH and Ti BS 3 SH showed 89 wt% loss of NaCl. Therefore, the samples were for further 24 h desalinated. After this second step of desalination, all samples showed 100 wt% loss of NaCl.

The linear change in dimension with respect to the samples after the first stage of debinding was recorded and the results can be seen in Figure 60 below:
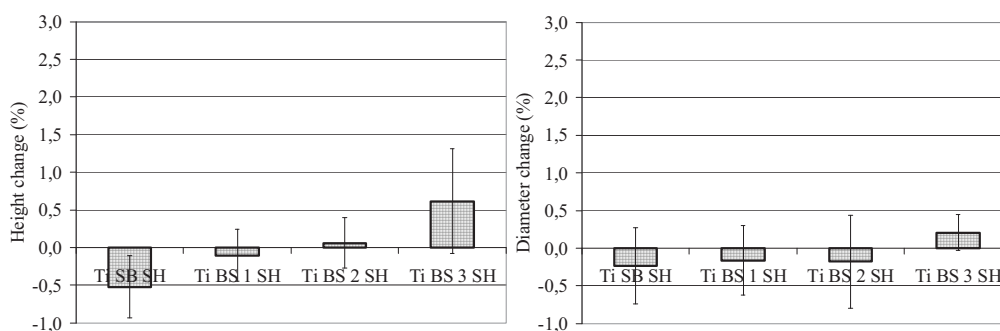
Figure 60: Linear change in diameter (right) and height (left) of the samples after desalination (n=6).

Values calculated with respect to the dimensions of partially debinded samples. Desalination parameters:

60°C, water, 48 h.

As compared to the dimensional changes occurred during solvent debinding (Figure 57 and Figure 58), the dimensional changes after desalination are almost negligible. It seems that few

or no swelling takes place during the process. This is expected, as polyethylene and polyethylene waxes are insoluble in water and no swelling in water is reported in the literature for these materials.

5.2.6 Sintering

All samples could be sintered and the pictures of the sintered samples are shown below in Figure 61:
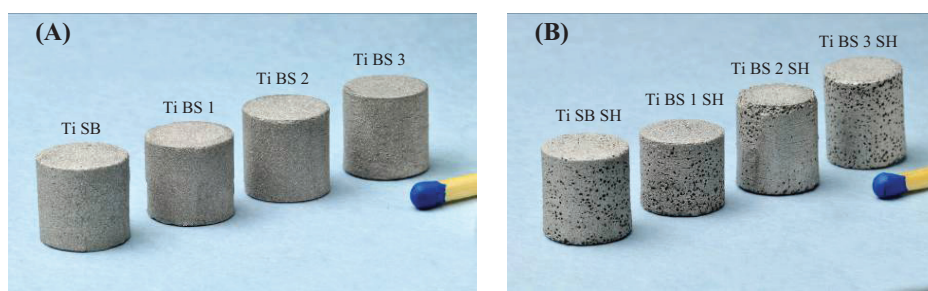
Figure 61: Pictures of the sintered samples. (A) samples without space holder (B) samples with space holder. Sintering parameters: 1300°C, 3 h, vacuum.

The surface porosity of the samples with space holder tended to be partially closed, and this effect was more pronounced for the paraffin-based binder systems. One of the samples, where this effect can be clearly seen is the BS 2 sample in Figure 61 B. For the Ti SB SH series, sand rests from the wicking process must be removed using a scalpel, before desalination. This treatment is though to be one of the reasons for an improved open porosity, due to removal of metal particles by the scalpel along with the sand. This may therefore contribute to open the surface porosity of the samples with the standard binder (SB) in comparison to the samples with the paraffin-based systems. These systems, on the other hand, do not undergo any cleaning or surface treatment after solvent debinding.

The vertical and horizontal shrinkage of the sintered samples with respect to the green bodies were calculated from sample dimensions after sintering. The results are shown in Figure 62 and Figure 63. The samples without space holder exhibit an average shrinkage of 9,8% in height and 11,3% in diameter. The samples with space holder shrink relatively more, with 11,6 and 12,2 % height and diameter shrinkage respectively.
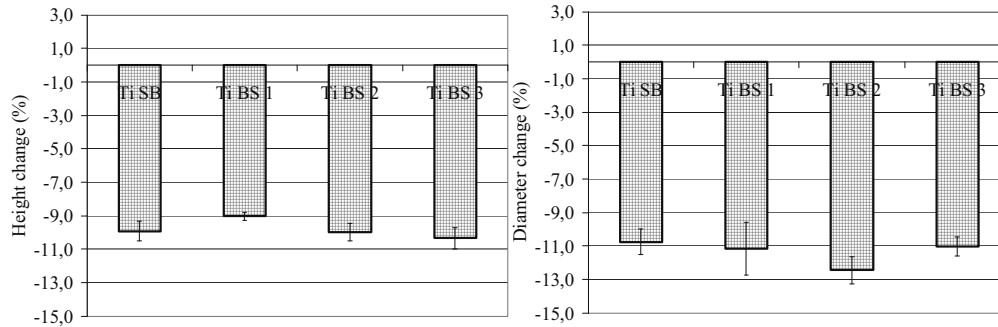
Figure 62: Height and diameter shrinkage for the samples without space holder after sintering (n=5).
Sintering parameters: 1300°C, 3 h, vacuum.
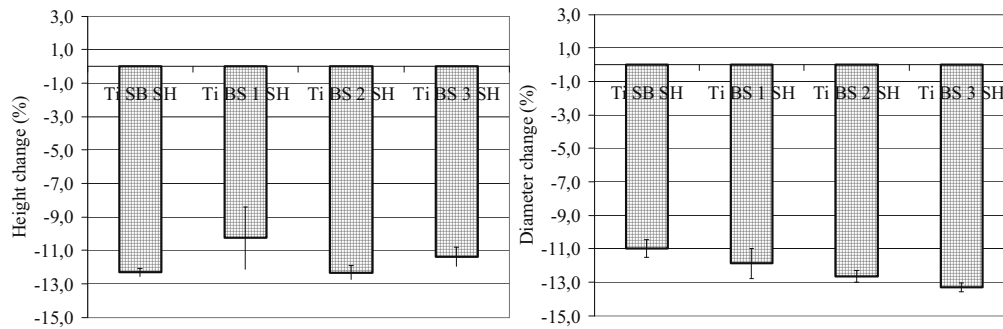
Figure 63: Height and diameter shrinkage for the samples with space holder after sintering (n=5).
Sintering parameters: 1300°C, 3 h, vacuum.

The difference in sintering shrinkage between feedstocks with and without space holder may be attributed to deviations of the actual binder content to the optimal binder content of the mixture. Samples with the optimal binder content (or less binder than the optimal point) have the amount of binder necessary to fill in the voids in the spaces between particles completely. The binder layer at the point where particles touch has normally negligible thickness (around 0,07 μm) at this point [38]. If the feedstock has small excess of binder, the binder thickness in between particles may not be negligible anymore and lead to higher sintering shrinkage. It is possible that the feedstocks with space holder fall into this situation.

The sintered density of the samples was calculated from geometrical measurement results and is shown in Figure 64 below:
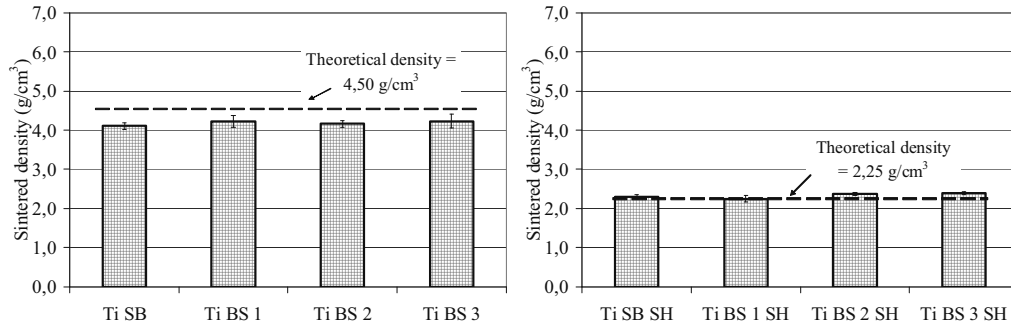
Figure 64: Sintered density of the samples with (right) and without (left) space holder.

The titanium samples without space holder do not reach the theoretical density of the material, whereas the theoretical density is exceeded in the case of the samples with space holder. In both cases, the samples with BS 2 and BS 3 binder systems exhibit slightly higher density values. This is in accordance with the higher shrinkage exhibited by these samples (Figure 62 and Figure 63).

The samples without space holder exhibit in average 7,2% residual porosity from the density values compared to the theoretical density of titanium ($4,50$ g/cm^3). The samples with space holder exhibit 48,2% porosity in average, which leads to higher values of sintered density as compared to a 50% porous titanium sample ($2,25$ g/cm^3). This may be attributed to the high sintering shrinkage of the titanium struts at 1300°C, which also causes a shrinkage of the macropores left by the space holder particles.

5.2.7   Microstructure characterisation

The microstructure of the samples was investigated and the light microscope pictures of the samples without space holder are shown below:
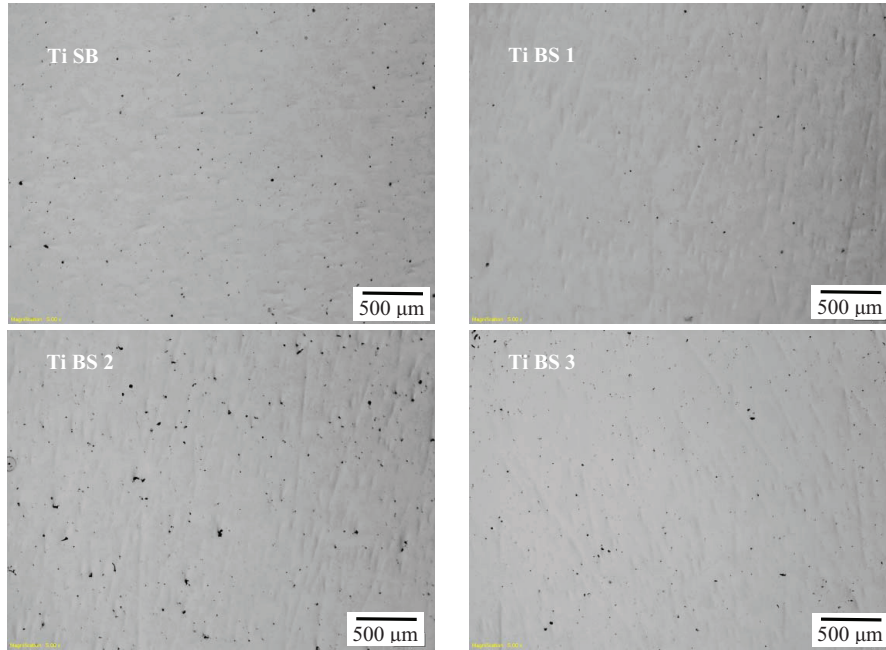
Figure 65: Microstructure of the samples without space holder. Sintering parameters: 1300°C, 3 h, vacuum.

The microstructure of the samples is relatively similar. All samples exhibit a comparable residual porosity in the inner part of the samples.

Although the inner part of the samples is similar, it was observed that the sample with the BS 3 binder exhibited cracks at the border area of the sample. These cracks are probably due to the solvent extraction process, as the strongest expansion in sample dimensions was especially noticed for the samples with this binder system.
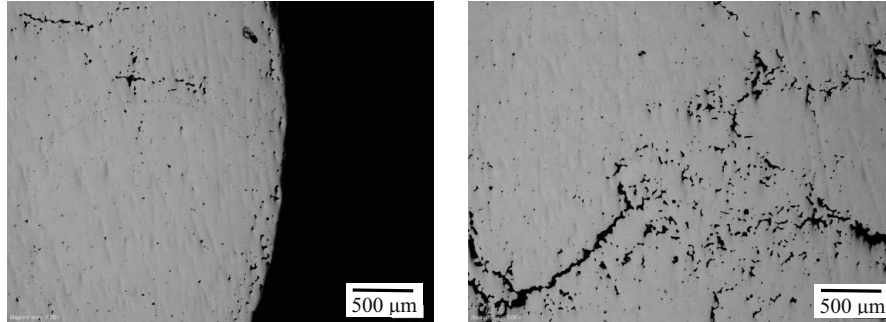
Figure 66: Cracks at the border area of the sample Ti BS 2.

The microstructure of the samples with space holder is shown in Figure 67 below:
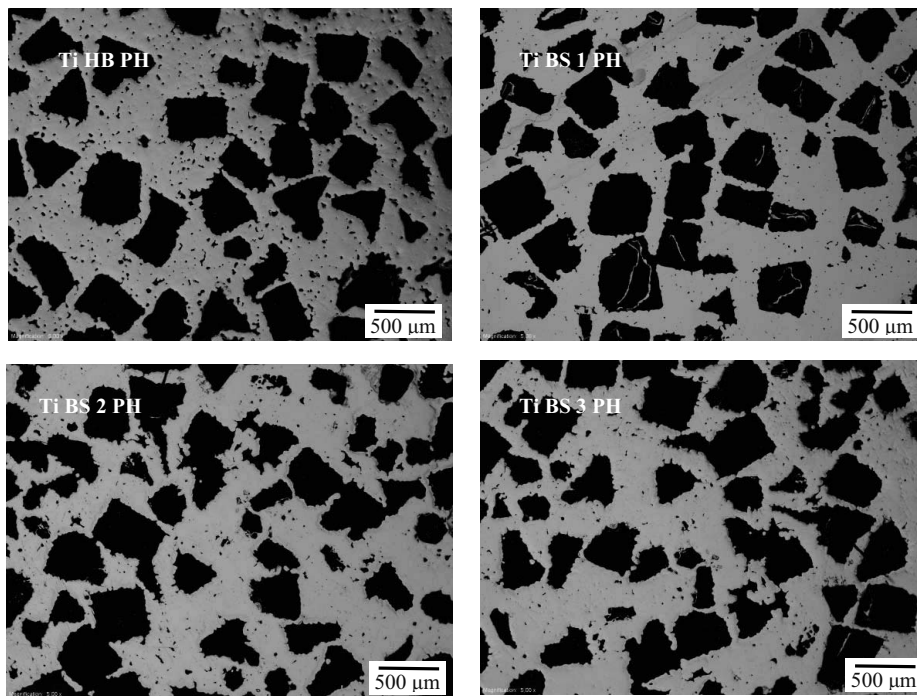
Figure 67: Microstructure of the samples with space holder. Sintering parameters: 1300°C, 3 h, vacuum.

The microstructure of the samples with space holder seems to be quite similar, independent of the feedstock. The pores are homogeneously distributed and the porosity was in average 46%

after calculation with the Analysis Software (3 pictures for each sample). In this case, no cracks in the samples were noticed.

5.2.8   Chemical impurities

The results of the chemical analysis of the starting powder, brown parts and sintered parts are shown graphically in Figure 68.
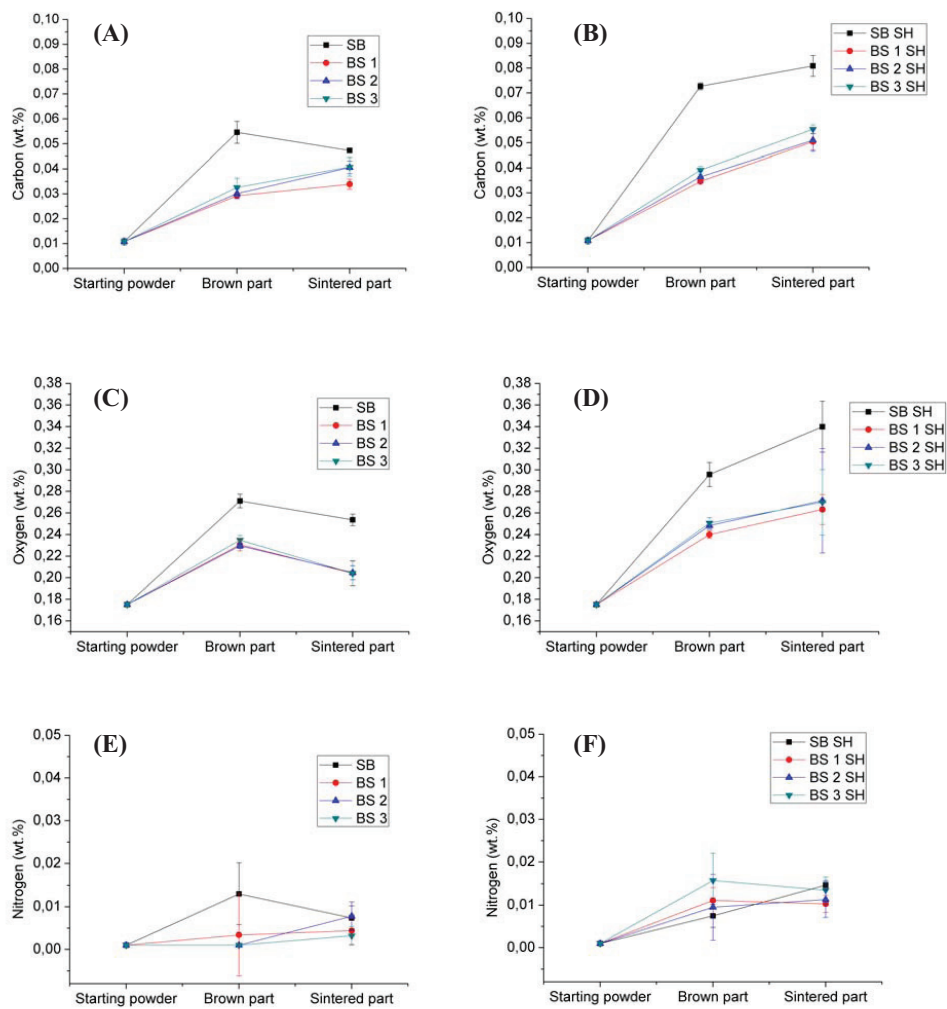
Figure 68: Carbon (A and B), oxygen (C and D) and nitrogen (E and F) content of starting powder, brown and sintered parts. Debinding parameters: 500 °C, 2 h. argon. Sintering parameters: 1300°C, 3 h, vacuum. (n=3-5)

Although the levels of all elements increase as compared to the starting material levels, the contamination of the titanium material with nitrogen seems to be negligible in comparison to carbon and oxygen. Although some samples reached 0.015 wt.% nitrogen content, where the contamination level is higher for the samples with space holder as compared to the samples without space holder, the nitrogen content was below the sensitivity of the equipment (< 0.001 wt.%) for some specimens. The individual results for carbon and oxygen levels of the sintered samples are discussed more in detail and are shown in Table 20.

Table 20: Oxygen and carbon contamination levels of the samples as compared to the starting powder.

Sample	Oxygen (wt.%)				Carbon (wt.%)			
	Starting powder	Sintered part	Increase		Starting powder	Sintered part	Increase	
			Absolute* (wt.%)	Relative ** (-)			Absolute (wt.%)	Relative ** (-)
Ti SB	0.18	0.25	0.07	1.4	0.01	0.05	0.04	5
Ti BS 1	0.18	0.20	0.02	1.1	0.01	0.03	0.02	3
Ti BS 2	0.18	0.20	0.02	1.1	0.01	0.04	0.03	4
Ti BS 3	0.18	0.20	0.02	1.1	0.01	0.04	0.03	4
Ti SB SH	0.18	0.34	0.16	1.9	0.01	0.08	0.07	8
Ti BS 1 SH	0.18	0.26	0.08	1.4	0.01	0.05	0.04	5
Ti BS 2 SH	0.18	0.27	0.09	1.5	0.01	0.05	0.04	5
Ti BS 3 SH	0.18	0.27	0.09	1.5	0.01	0.06	0.05	6

* Absolute increase: contamination of sintered part – contamination of starting powder

** Relative increase: contamination of sintered part / contamination of starting powder

For both carbon and oxygen, the contamination level increases with thermal debinding, for samples with and without space holder. When the samples are sintered, the tendency is that the contamination levels of both carbon and oxygen decrease for the samples without space holder and increase for the samples with space holder. It seems that the addition of space holder particles to the feedstock and especially the desalination step at 60°C to which the samples are subjected probably contaminate the titanium particles more than in the case of space holder free feedstocks.

The influence of the binder system composition on the contamination level of the samples is clear. For both carbon and oxygen, the contamination level is always higher for the samples with the SB system than for the paraffin-based systems. This occurs for both materials with or without space holder, as brown or sintered part. Sintered samples without space holder with the paraffin-based systems have around 0.20 wt.% oxygen and therefore fulfil the ASTM requirements of grade 2 (< 0.25 wt.% oxygen). The samples with space holder are just 0.02

wt.% above grade 2 level. The SB samples without space holder, on the other hand, are on the limit of grade 2 due to their oxygen content of 0.25 wt%. The SB samples with space holder are on the limit of grade 3 (< 0.35wt.% oxygen), with 0.34 wt.% oxygen. In previous studies [112], only ASTM grade 4 was achieved for 50 % porous titanium samples.

The different oxygen contamination levels of samples with SB and paraffin-based systems is probably due to the chemical composition of the binder materials employed. Paraffin-based systems are composed of oxygen-free molecules, in contrast to the SB system, where Wax C is an oxygen containing material. The oxygen of remaining Wax C in the sample after the first stage of debinding probably reacts with the titanium powder during thermal debinding and sintering. It seems that Wax C influences the contamination of the samples with carbon as well. The carbon contamination of the samples with the BS 1 system is significant lower than the SB samples, although both systems have the same second binder component (PE 520). This suggests that residuals of Wax C remain in the sample after the first stage of debinding and contaminate the SB samples with carbon during debinding and sintering.

5.2.9   Graded samples by warm pressing

The possibility of the production of samples with a gradient in porosity with the investigated binder systems was evaluated by warm pressing feedstocks with and without space holder, one after another. The samples were debinded, desalinated and sintered. Parts with a gradient in porosity could be produced with all feedstocks. A picture of the cross-section of the samples produced, together with the typical microstructure, is shown in Figure 69.
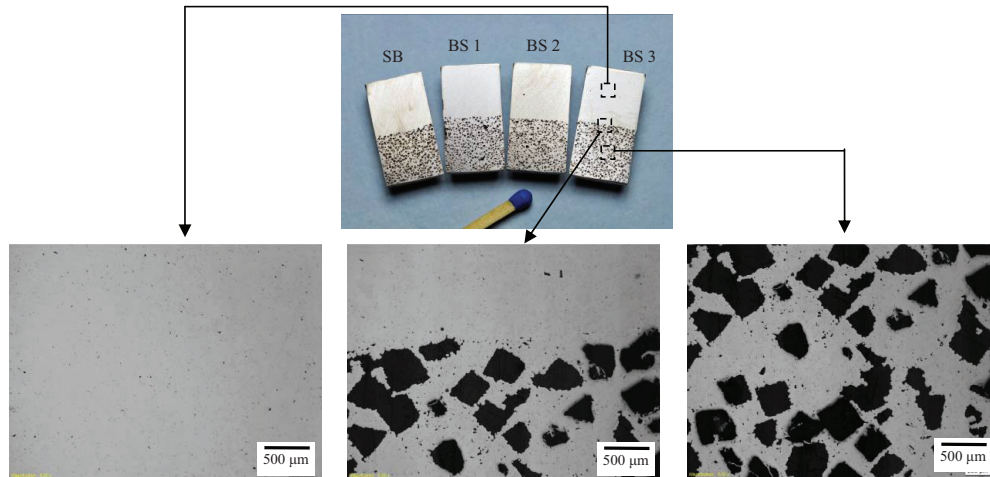
Figure 69: Pictures of titanium samples with a gradient in porosity. The microstructure of the sample with the BS 3 binder system is shown as an example. Sintering parameters: 1300°C, 3 h, vacuum.

All samples exhibit a similar microstructure. The interface between the porous and dense parts, deriving from feedstocks with and without space holder particles, is very well defined. All samples still show less than 1% standard deviation in diameter shrinkage (n=3), despite of the gradient in porosity and the different shrinkages of the dense and porous masses. The only exception here are the samples with the BS 1 system, which were partially broken off at the surface after solvent debinding and therefore showed increased dimensional deviation.

5.2.10 Feedstock flowing behaviour and choice of preferred binder system

After confirming the potential of the investigated feedstocks for the production of samples with a gradient in porosity, the rheology of the feedstocks was investigated. The objective here was to choose the feedstocks which are best suitable for the 2-C-MIM application. The feedstocks without space holder (Ti SB, Ti BS 1, Ti BS 2 and Ti BS 3 with 68 Vol.% solid content each) were investigated hereby at first.

After feeding the feedstock in the bore, the feedstocks Ti SB and Ti BS 1 showed binder-powder separation during the heating up phase. Binder material with powder particles in suspension flowed out of the capillary. When the test was started, the capillary was clogged by the remaining Ti-particles and no measurement could be carried out. The phase separation observed was already expected for these feedstocks, as their binder systems exhibit a very low

viscosity (Table 18) as compared to the other feedstocks investigated and to the value suggested in the literature (up to 10 Pa·s) [38]. Further studies at the capillary rheometer with these feedstocks were discontinued. Their use for the 2-C-MIM application seems to be unsuitable, especially if used in the vertical injection unit.

No binder-powder separation was observed during the heating up phase for the feedstocks Ti BS 2 and Ti BS 3. Nevertheless, when the measurement was started, the feedstock started to flow but stopped before reaching 1000 s^{-1} shear rate. This seems to be an indication that the solids content was over the critical limit. It was presumed that the optimum powder content of the feedstocks must be found for transferring the results of warm pressing to the 2-C-MIM process. Therefore, the solids loading of the feedstocks were varied for the further investigation. This study was done using Fe22Cr powder. The feedstocks Fe BS 2 and Fe BS 3 were produced with reduced solids contents (50 and 60 Vol.% powder). Here, two different behaviours were observed when heating up the feedstocks in the equipment bore. The feedstock Fe BS 2 flowed considerably out of the capillary during the heating up phase, whereas a negligible flow was observed for Fe BS 3.

As it is not desirable that the feedstock flows during the heating up phase, as the use in the vertical injection unit would be affected in the case of 2-C-MIM, further tests with the feedstock Fe BS 2 were discontinued. The investigation was further carried out with the Fe BS 3 feedstock, where the solids loading was further varied.

5.3 Optimisation of feedstock solids loading and flowing behaviour using Fe22Cr powder

After investigating the flowing behaviour of the titanium feedstocks and choosing the most promising binder system for the 2-C-MIM application, the feedstock solids loading was optimised. Moreover, the effects of stearic acid addition, space holder particles, and binder component ratio were further studied. The results obtained are presented in the next sections.

5.3.1 Effect of solids loading

The shear viscosity of the feedstock Fe BS 3 versus the shear rate curves are shown in Figure 70 for different solids loadings, with and without Bagley and Rabinowitsch corrections.
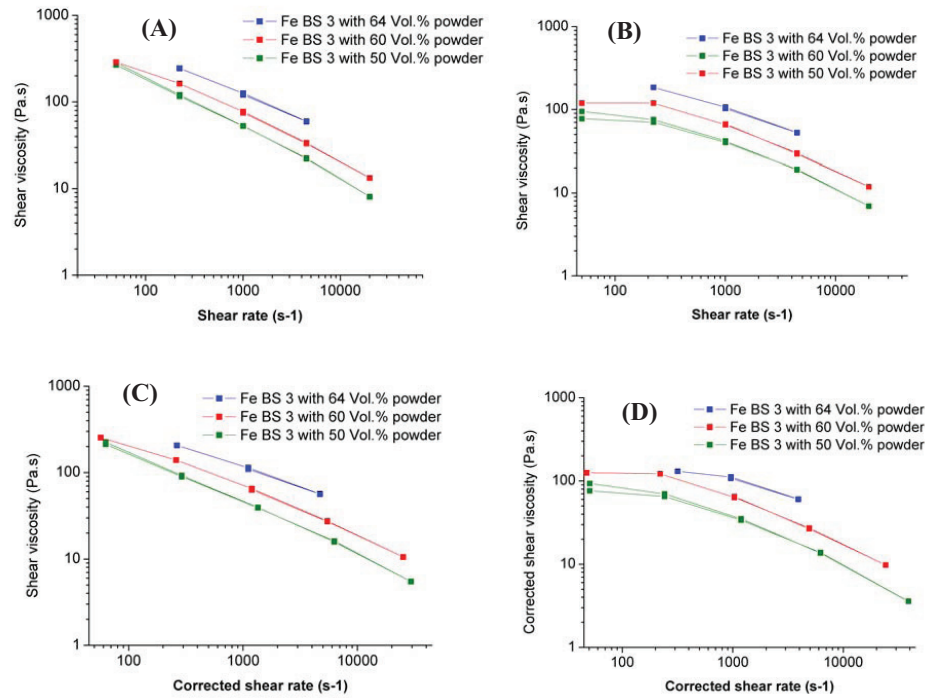

Figure 70: Shear viscosity versus shear rate for feedstocks Fed BS 3 with different powder contents. (A) No corrections applied. (B) With Bagley correction. (C) With Rabinowitsch correction. (D) With both corrections. Temperature of the measurements: 150°C.

It seems that the Bagley correction has a greater influence than the Rabinowitsch correction. No significant difference is seen between the uncorrected curves (Figure 70 A) and the curves with the Rabinowitsch correction (Figure 70 C). On the other hand, when the curves are submitted to the Bagley correction (Figure 70 B), the viscosity values are clearly lower than the uncorrected ones (Figure 70 A). That is probably due to a high pressure drop at the capillary entrance.

The viscometer encountered difficulties in measuring the viscosity at 4000 s^{-1} shear rate for the 64 Vol.% solids loading feedstock, as the maximal force of the rheometer was reached. An attempt was made to measure the viscosity of the feedstock with 68 Vol.% powder, but in this case no measurement was possible. As the test was started after the heating up phase, the capillary was clogged. This is an indication that the critical point of the mixture was reached.

As expected, the viscosity of the feedstock increases with increasing solids loading, as described by Formula 5. Independent of the solids content, all materials exhibit shear thinning behaviour, as known also for other PIM-feedstocks [38].

An attempt was made to compare the values of shear viscosity obtained by capillary measurements with values obtained the formula described in the literature to predict viscosity of suspensions as a function of the solids loading (Formula 5). For the calculation, the parameter ϕ_c, related to the particle packing, was considered as 0.68, which is described as the appropriate value when smooth spheres are used [91]. The binder viscosity μ_B was taken from the values obtained from the rotational viscometer at 1000 s^{-1} (2.2 Pa·s; Table 12). The viscosity values were calculated and the results obtained are shown in Table 21.

Table 21: Feedstock viscosity calculated by formula in the literature and results obtained from the

capillary viscometer. Measurement parameters: $\dot{\gamma}$ = 1000 s^{-1}, T = 150°C.

Solids loading (Vol.%)	Feedstock viscosity calculated by Formula 5 (Pa.s)	Measured feedstock viscosity (Pa.s)
50	31.4	34.4
60	159.0	64.1
64	635.8	109.6

It seems that the formula proposed in the literature predicts well the feedstock viscosity at 50 Vol.% solids loading, but fails to predict the value at higher solids loadings. The values predicted at 60 and 64 Vol.% powder are much higher than the values measured at the capillary viscometer. Formula 5 is an empirical equation, obtained with polymer melts with various fillers up to 40 Vol.% powder [89]. Another empirical equation proposed in the

114

literature [99], where solids loadings up to 60 Vol.% were tested, showed even strongest disagreement with the data obtained from the capillary viscometer.

5.3.2 Effect of stearic acid

For further improvement of flowing behaviour, stearic acid was added to the mixture in the case of the feedstock Fe BS 4. The results are shown in Figure 71.
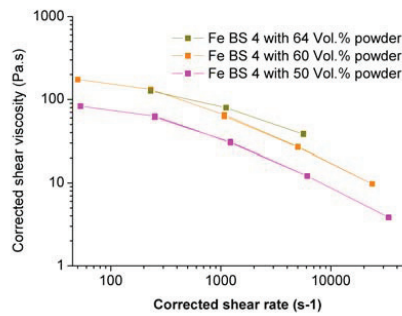
Figure 71: Shear viscosity versus shear rate for feedstocks Fed BS 4 with different powder contents. Temperature of the measurement: 150 °C.

As expected, the viscosity increases again with increasing powder content. Figure 72 shows that if the feedstocks with and without stearic acid are compared, it seems that there is no significant difference in viscosity for the powder contents of 50 and 60 Vol.%. On the other hand, the difference in viscosity of the feedstocks with and without stearic acid is considerable for the 64 Vol.% solids content, as can be seen in Figure 72 B.
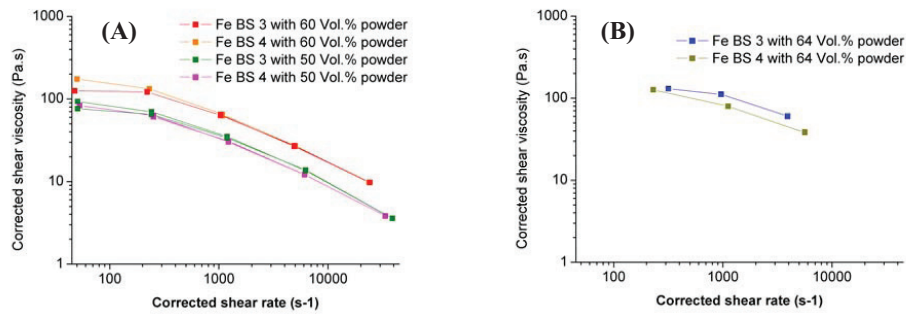
Figure 72: Corrected shear viscosity versus corrected shear rate for the feedstocks Fe BS 3 and Fe BS 4. (A) 50 and 60 Vol.% powder. (B) 64 Vol.% powder. Temperature of the measurement: 150 °C.

115

If a the viscosity is plotted against the powder content at a constant shear rate, the difference in viscosity of Fe BS 3 and Fe BS 4 at 64 Vol.% powder is evident. The curves are shown in Figure 73.
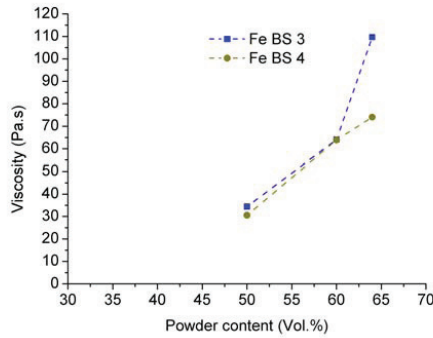
Figure 73: Viscosity versus powder content for the feedstocks Fe BS 3 (without stearic acid) and Fe BS 4 (with stearic acid). Measurement parameters: $\dot{\gamma} = 1000$ s^{-1}, T = 150°C.

For both feedstocks, with and without stearic acid, no viscosity could be measured for the feedstock with 68 Vol.% powder, as the capillary was clogged when the test was started. The critical point seems to be already reached at 68 Vol.% powder. The viscosity increases drastically if the solids content reaches 64 Vol.% powder for Fe BS 3. The addition of stearic acid in the feedstock Fe BS 4 decreased the viscosity considerably at this powder content. On the other hand, it seems that stearic acid does not have a significant influence on feedstock viscosity at solid contents far from the critical point (50 and 60 Vol.% powder). Due to the lower viscosity value when nearing the critical point of the mixture, the use of stearic acid was favoured in this work and this additive was used for further investigations.

5.3.3   *Effect of space holder particles*

Feedstocks with space holder particles were investigated using the binder system BS 4. The results for the feedstocks with 50, 60 and 68 Vol.% solids contents are shown in Figure 74.
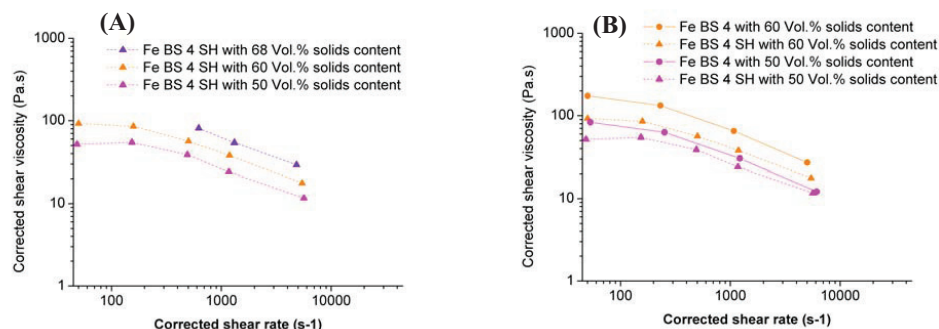
Figure 74: Corrected shear viscosity versus corrected shear rate for the feedstocks Fe BS 4. (A) Feedstocks with space holder. (B) Comparison of feedstocks with and without space holder with 50 and 60 Vol.% solids loading. Temperature of the measurements: 150°C.

The viscosity of the feedstock Fe BS 4 SH could be measured with the capillary viscometer up to 68 Vol.% solids loading. The feedstock with 72 Vol.% solids loading could not be injected through the capillary, indicating that the critical point was already reached at this solid content for this system.

As expected, the viscosity increases with increasing solids content for feedstocks with space holder particles. This was observed for the feedstocks without space holder as well. When feedstocks with and without space holder are compared, it becomes obvious that the addition of space holder particles decreases the viscosity of the feedstock with the same binder system and solids content. The decrease of viscosity observed in bimodal systems when compared to systems with monosized particles was already described in the literature [98, 99]. The decrease in viscosity may be explained by the decrease of the number of particles near the capillary wall, which was observed in previous studies with bimodal systems [98].

The viscosity values obtained for feedstocks with and without space holder were plotted against the solids loading and are shown in Figure 75.
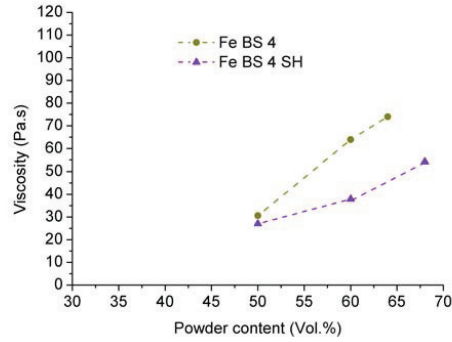
Figure 75: Viscosity versus powder content for the feedstocks Fe BS 4 (without space holder) and

Fe BS 4 SH (with space holder). Measurement parameters: $\dot{\gamma}$ = 1000 s^{-1}, T = 150°C.

The difference in viscosity of feedstocks with and without space holder is evident and is more pronounced for the feedstocks with more than 60 Vol.% solids loading.

5.3.4 *Effect of component ratio*

The influence of the variation of the binder components ratio was investigated as well. The binder system BS 5, which contained 5 Vol.% less amount of the second component Hostalen GA 7260 G as compared to the BS 4 system, was hereby investigated for feedstocks with space holder. The results obtained are shown in Figure 76.
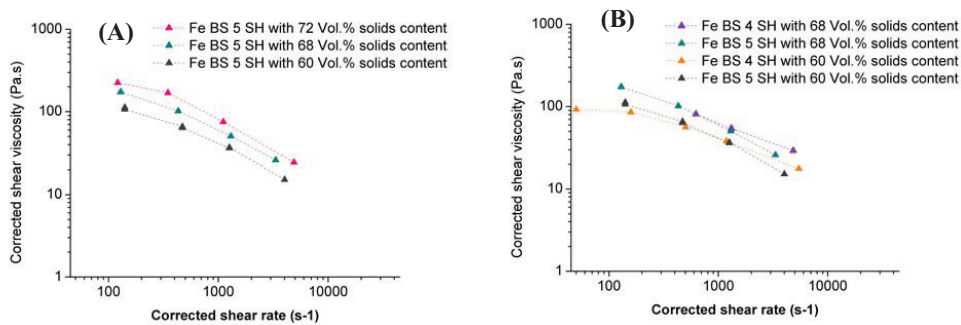
Figure 76: Corrected shear viscosity versus corrected shear rate. (A) Feedstock Fe BS 5 SH (B)
Comparison of feedstocks Fe BS 5 SH and Fe BS 4 SH with 60 and 68 Vol.% solids loading. Temperature
of the measurements: 150°C.

The viscosity of the feedstock Fe BS 5 SH could be measured with the capillary viscometer up to 72 Vol.% solids loading, as seen in Figure 76 A. The feedstock with 75 Vol.% solids loading could not be injected through the capillary, indicating that the critical point was already reached at this solid content for this system. The decrease of 5 Vol.% in the Hostalen content seem to have contributed to an increase in the maximal solids loading of the feedstock, as compared to the system BS 4.

As expected, the viscosity increases with increasing solids content for the system BS 5 as well. If the feedstocks with the systems BS 4 and BS 5 with the same solids content are compared (Figure 76 B), similar curves are obtained and no significant difference between the feedstocks could be noticed. Only at around 4000 s^{-1} shear rate, the feedstocks with the system BS 5 show a relative lower viscosity as compared to the feedstocks with the system BS 4.

5.3.5 Determination of the optimal solids loading

In the literature, tap density, feedstock density and mixing torque measurements are suggested as methods for the determination of the optimal solids loading for a feedstock. Measurements with these methods were additionally conducted to support and evaluate the results of capillary viscosimetry.

The measurements were performed with Fe22Cr powder, for comparison purposes with the capillary measurements.

Tap density

The tap density of the materials was investigated and the density of feedstocks was measured in order to assist the determination of suitable binder contents for the feedstocks investigated. The tap density of the investigated materials and the percentage of empty spaces in between the particles are shown in Table 23, calculated after formula 24.

Table 22: Tap density as percentage of the theoretical density and empty spaces for Fe22Cr powder and its mixture with NaCl particles.

Material	Tap density -% of the theoretical density	Empty spaces (Vol. %)
Fe22Cr powder	59	41
50 Vol.% Fe22Cr powder + 50 Vol.% NaCl	71	29

The tap density of the mixture of Fe22Cr powder and NaCl particles is higher than in the case of the metal powder alone. This is already expected, as powder and space holder form a bimodal particle distribution, where the smaller particles pack in between the larger ones. Monodispersed systems like the Fe22Cr powder alone always pack to lower densities than bidispersed ones.

Considering that probably the particles do not pack to the highest density possible during the tapping process and there are less empty spaces in reality than the result measured after the method, the optimal solids loading is probably more than 59 Vol.% for the Fe22Cr powder alone and more than 71 Vol.% for the feedstock with space holder particles after this method.

The results achieved show that the tap density measurement gives only a first approximation of the optimal solids loading. With the capillary measurements, the maximal solids loading which could be reached was 64 Vol.% powder for the feedstocks with the systems BS 3 and BS 4. For the feedstocks with space holder, the maximal solids loading reached was 68 Vol.% for the feedstock Fe BS 4 SH and 72 Vol.% for the feedstock Fe BS 5 SH. Capillary viscosimetry results are more adequate for determination of the optimum solids loading due to similarity to the injection moulding process already in the measuring principle. The injection of the feedstock material through the capillary is similar to the injection of the feedstock through the injection unit nozzle.

Density of feedstocks

The density of the feedstocks was measured for the feedstocks without space holder particles with the Archimedes method with various solids contents. For this study, the feedstock Fe BS 3 with various solids loadings was investigated and the results are shown in Figure 77.
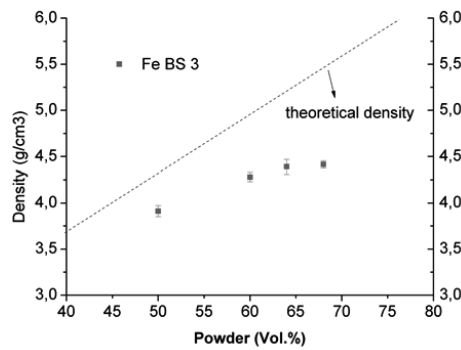
Figure 77: Density of feedstocks versus powder content. (n=3) The theoretical density of the mixture (calculated by the rule of mixture) is shown by the dashed line.

It seems that feedstock density always deviate from the theoretical density for all powder contents investigated. This is not expected from what is described in the literature (Figure 19). It seems that either voids are always present between binder and powder particles in the feedstock or the density values of the starting materials supplied by the producers are not accurate. Another possibility is that some of the powder particles are hollow spheres. Nevertheless, from the results obtained it is possible to see that there is a tendency of increase of the feedstock density up to 64 Vol.%, what is in accordance to the rule of mixture. The feedstock with 68 Vol.% powder shows approximately the same density than the 64 Vol.% and the tendency of density increase is not present anymore. This is probably an indication that at 68 Vol.%, the critical solids loading has already been reached for the feedstock investigated, which is in agreement with capillary measurements.

Torque measurements

Torque measurements were performed with the feedstock Fe BS 3 as well. The torque values at different solids loadings and the respective deviations were plotted and are shown in Figure 78.
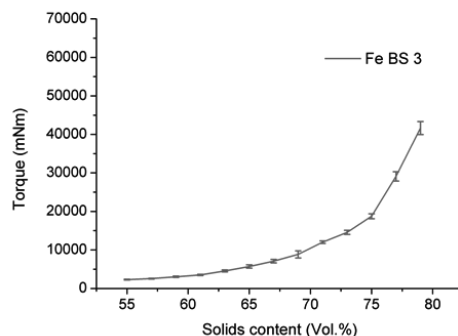
Figure 78: Mixing torque versus powder content for the feedstock Fe BS 3. Measurement temperature: 150°C.

As expected, the mixing torque increases with increasing solids content. Although the values obtained deviate more from an average value as the solids content increase (shown by the error bars in the curve), it was not clear where this deviation could be considered so significant so that the critical point of the mixture was reached. The solids loading inside the torque rheometer could be raised to the theoretical value for monosized spheres (74%) and even over that value, up to 77 Vol.%. It seems that the equipment is able to deliver torque values even when the critical solids has been clearly exceeded. The method seems to be not sensitive enough for the determination of the critical solids loading. Moreover, the method is laborious and great amounts of powder have to be dispensed for the measurement.

The optimal solids loading

All methods for determining the optimal binder amount of a feedstock have their limitations and deficiencies. Nevertheless, it is possible to evaluate the methods investigated by comparing the results obtained and the effort which each method required.

Torque measurements did not deliver reasonable results and is the most laborious among the methods investigated. It is therefore not advisable in the future further experiments with the equipment for the purpose of determining the optimal solids loading.

Although density measurements on feedstocks is a simple method, the results obtained are in disagreement with descriptions in the literature, considering that the theoretical density was never achieved, even for the feedstock with very low solids loading (50 Vol.%). Density

measurements may be advisable as an additional information about the material investigated and if associated to a more efficient method.

It seems that the tap density is a good starting point for predicting the optimal solids loading of a feedstock, but additional measurements of the flowing ability of the feedstock are advisable due to the fact that it does not take into account powder-binder interaction during flow, which could be different for different binder systems. One example is the maximal solids loading of 68 Vol.% for Fe BS 4 SH and 72 Vol.% for Fe BS 5 SH. Only a 5 Vol.% lower amount of the binder component Hostalen led to an increase of the maximal solids loading, which was detected by capillary measurement and would not be detected by a simple tap density measurement.

Capillary measurements seem to deliver the most promising results for the determination of the optimal solids loading. In contrast to tap density, feedstock density or torque measurements, capillary measurements predict the flowing behaviour of the feedstock when pressed through a capillary, which is analogous to the injecting of the feedstock through the nozzle into the mould. The method has though its limitations, as the force reached by the pistons in the capillary viscometer (20 kN for both pistons) is much lower than the force reached by the injection units in the MIM machine (100 kN for each injection unit). It is therefore expected that the feedstocks which could be pressed through the capillaries of the viscometer will be injected in the MIM machine without problems.

5.4 Transfer of optimised binder system to Ti powder

After investigating the flowing behaviour of Fe22Cr feedstocks at various solids contents and determining the optimal solids loadings for the most promising feedstocks, the results were transferred to titanium powder. The comparison of the tap density of both powders with and without space holder particles is shown in Table 23, calculated after Formula 24.

Table 23: Tap density as percentage of theoretical density and empty spaces for Fe22Cr and Ti powder and its respective mixtures with NaCl particles.

Material	Tap density -% of the theoretical density	Empty spaces (Vol. %)
Fe22Cr powder	59	41
Ti powder	65	35
50 Vol.% Fe22Cr powder + 50 Vol.% NaCl	71	29
50 Vol.% Ti powder + 50 Vol.% NaCl	73	27

The tap density of the Fe22Cr powder material is lower than that of the Ti powder. This is valid for the mixtures of these powders with NaCl particles as well. Although the particle size distribution of both Fe22Cr and Ti powders are in a similar range, the particle size distribution of the titanium powder is more advantageous regarding packing density as the Fe22Cr powder (Table 9). The Fe22Cr powder was fractioned in the range 22-53 μm, so that particles smaller than 22 μm are not present. The Ti powder, on the other hand, was fractioned as < 45 μm, so that the small particles fill in the voids between the larger particles and increase therefore the packing density. It is therefore expected that a transfer of the results to titanium powder does not bring complications. A Fe22Cr feedstock which could be injected through the capillary is expected to be injected with titanium powder without problems, due to the lower demand on binder of the titanium powder when compared to Fe22Cr powder.

In this way, the titanium feedstocks Ti BS 4, Ti BS 4 SH and Ti BS 5 SH with respectively 64, 68 and 72 Vol.% solids loading, which were the solids loadings chosen in the previous section for Fe22Cr powder, were produced with titanium powder.

The feedstocks were afterwards warm pressed, debinded, desalinated and sintered. The sintering shrinkage of the samples was recorded (n=3). The samples of the feedstock Ti BS 4 shrink 11,2% in average, whereas the shrinkage for Ti BS 4 SH and Ti BS 5 SH are 17,4 %

and 11,4 % in average. Among the samples with space holder, the samples with the feedstock Ti BS 4 SH shrink much more than the samples with the feedstock Ti BS 5 SH. This is already expected, due to the higher binder amount in Ti BS 4 SH than in Ti BS 5 SH. Pictures of the sintered samples are shown in Figure 79, where even a slight deformation of the cylindrical shape of the sample Ti BS 4 SH is seen. The deformation is probably due to the high content of binder in this feedstock.

(A)

(B)

Ti BS 4

(64 Vol.% solids content)

Ti BS 4 SH

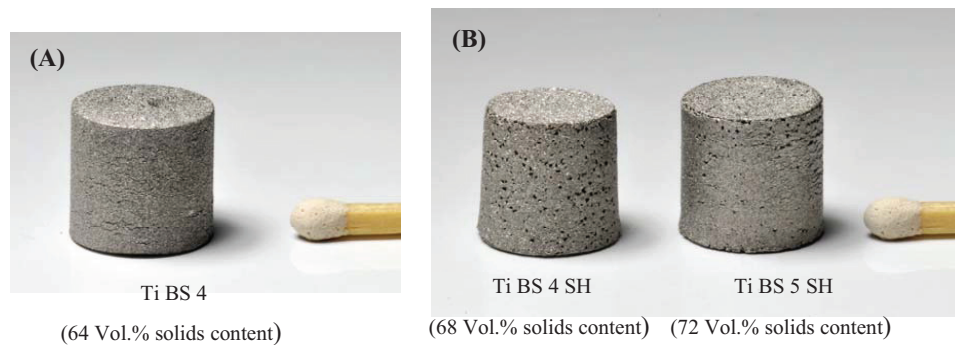(68 Vol.% solids content)

Ti BS 5 SH

(72 Vol.% solids content)

Figure 79: Picture of sintered samples. (A) Feedstock without space holder: Ti BS 4. (B) Feedstocks with space holder: Ti BS 4 SH and Ti BS 5 SH. Sintering parameters: 1300°C, 3 h, vacuum.

In order to be selected for further tests with the 2-C-MIM machine, it is important that the sintering shrinkage of the feedstocks with and without space holder are similar. Due to the more similarity in sintering shrinkage and due to the shape loss of Ti BS 4 SH samples, the feedstocks Ti BS 4 and Ti BS 5 SH were selected for tests with the 2-C-MIM machine with the spinal implant mould.

5.4.1 Effect of temperature on selected Ti feedstocks

The optimal temperature is described in the literature to be specific for each binder system and powder mixture. The temperature of the feedstocks was varied in order to investigate its effect on flowing behaviour and to optimise the working temperature for experiments with the MIM machine.

From the starting point of the primary working temperature selected (150°C), an attempt was made to gradually decrease the temperature. The injection temperature should be high enough to promote feedstock flow, but it is always desirable not to work at higher temperatures than necessary, in order to avoid unnecessary binder decomposition. The obtained curves are shown in Figure 80.
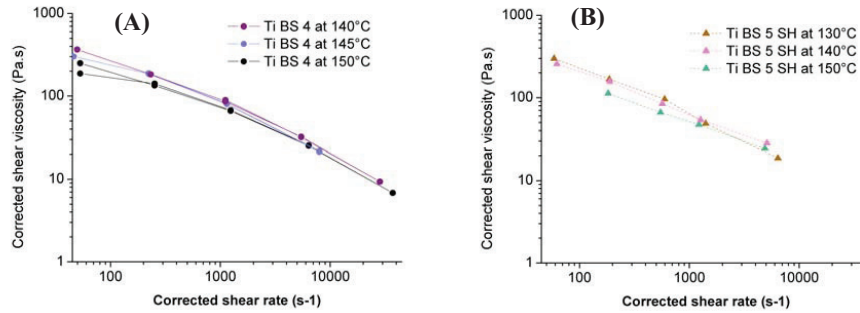
Figure 80: (A) Ti BS 4 at different temperatures. (B) Ti BS 5 SH at different temperatures.

The measurement with the capillary viscometer could be performed without problems for Ti BS 4 until 140°C, but at 135°C the material was already too stiff to be injected. On the other hand, measurements with the feedstock Ti BS 5 SH could be performed up to 130°C. At 125°C, the material was already too stiff and did not flow out of the capillary. The difference in lowest injection temperature between the feedstocks lays on the different systems investigated. Feedstocks with and without space holder particles have different flowing behaviours and different demands on binder amount, as discussed in the last sections. The lower Hostalen content of the binder system BS 5 may also influence the different lowest flowing temperatures of the feedstocks.

A slight difference in viscosity exists in the temperature range investigated for both feedstocks, but it seems to be almost negligible, especially at higher shear rates.

Due to the similarity in flowing behaviour of the feedstocks at the temperature ranges investigated, the injection temperature of 140°C (for both feedstocks with and without space holder) was selected for injection moulding trials.

5.5   Fabrication of a titanium spinal implant with gradient in porosity

5.5.1   2-C-MIM with a fully automated mould

The titanium feedstocks Ti BS 4 and Ti BS 5 SH with respectively 64 and 72 Vol.% solids loading were used for the injection trials with the MIM machine with the spinal implant mould.

The first step was to optimise the parameters for the injection of the feedstock without space holder. Feedstock injection was performed at 140°C, which was the temperature selected after capillary tests. As injection pressure is a very important parameter in order to produce dense parts, maximal injection pressures of 600, 800, 1000 and 1100 bar were investigated. Green parts were produced and the green density was measured with the Archimedes method. Figure 81 shows the green density of the samples as a function of the maximal injection pressure. A pressure of 800 bar seems to be enough to obtain the highest green density possible for this feedstock.
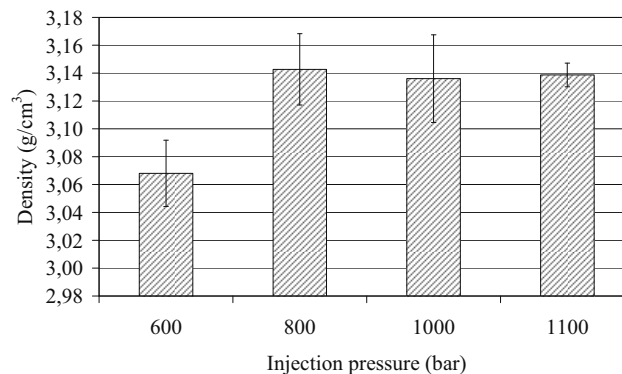
Figure 81: Green density as a function of the maximal injection pressure for the feedstock Ti BS 4.

The same procedure was done for the feedstock with space holder, where the feedstock with space holder was injected after the injection of the feedstock without space holder (at 800 bar injection pressure). Figure 82 shows the complete injection sequence and some of the obtained green parts. The feedstock without space holder was injected through the horizontal injection unit, as the feedstock with space holder was injected through the vertical injection unit.
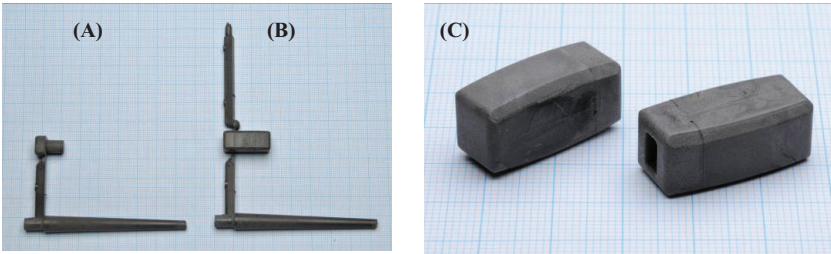
Figure 82: (A) Injection of the feedstock without space holder. (B) Injection of the feedstock with space holder. (C) Final green parts.

The injection pressure of the feedstock with space holder was performed at different maximal injection pressures as well. As the density of samples with space holder can not be measured with the Archimedes method due to the contact of NaCl to water, only the mass of the samples was recorded in this case. The results of the sample mass as a function of the maximal injection pressure are shown in Figure 83. It seems that, in this case, a maximal pressure of 1000 bar is enough to obtain green parts with high densities.
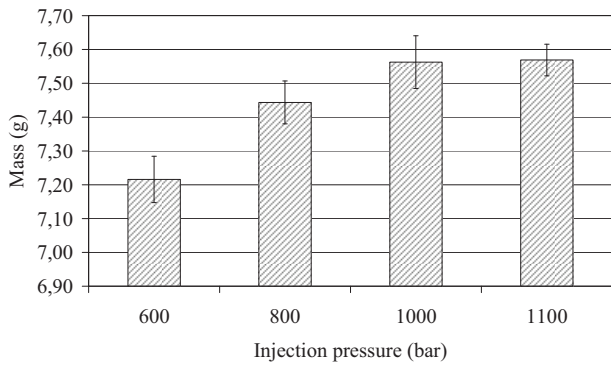
Figure 83: Sample mass as a function of the maximal injection pressure for the feedstock Ti BS 5 SH.

The parameters used for the injection of the feedstocks with and without space holder are shown in Table 24.

Table 24: Injection parameters used for the injection of the feedstocks Ti BS 4 and Ti BS 5 SH.

Feedstock charging*			Temperature*						
Screw rotational velocity (U/min)	Charging volume (cm^3)	Decompression volume (cm^3)	Zone				Nozzle		Mould (°C)
			1 (°C)	2 (°C)	3 (°C)	4 (°C)	5 (°C)		
5	6,75 (4,15)	0,5	60	120	130	138	140		50

Injection pressure* (bar)	Compression pressure*				
	1 (bar)	2 (bar)	3 (bar)	4 (bar)	Total compression time (s)
800 (1000)	800	650	500	100	3,6

*Number in brackets for the feedstock with space holder. If just one number, value used for both feedstocks.

Although both feedstocks could be injected, it must be pointed out that the injection of the feedstock with space holder through the vertical unit was compromised by a construction failure, in which the injection unit did not reach the mould and a nozzle extension had to be coupled to the unit nozzle. Another problem was that some feedstock came out of the nozzle extension after an injection cycle, like in a die swelling process. Die swelling is a common phenomenon in polymer processing, where the material swells back to the former shape after being compressed through a die. It is directly related to entropy and polymer relaxation within the flow stream. It is presumed that the feedstock, which was at the tip of the nozzle, cooled down during the cycle and possibly induced injection problems. The cycle was sometimes interrupted because injection of the feedstock with space holder was blocked at the runner area.

The samples were debinded, desalinated and sintered at 1200 and 1300°C (3 h, vacuum). Samples with injection pressure 800 and 1000 bar of the feedstock with space holder were hereby investigated.

5.5.2 *Characterisation of the implants*

One of the sintered samples is shown in Figure 84 as an example. The dense and porous parts are evident at the sample surface. The samples where measured with a sliding calliper at the locations indicated in the figure.
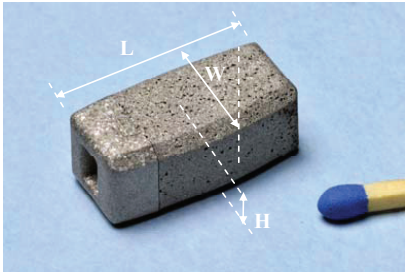
Figure 84: Sintered titanium part produced with feedstocks Ti BS 4 and Ti BS 5 SH with 64 and 72 Vol.%
solids content, respectively. The arrows indicate the locations where the samples were measured:
length (L), width (W) and height (H).

The length L, the heights H_1 and H_2 could be measured without problems. The width W of the sample could be measured only with significant error, due to the curvature of the implant at this location (Figure 40). In this way, only the height H and the length L were used for the calculations. Figure 85 shows the sintering shrinkage of the samples produced at 800 and 1000 bar maximal injection pressure of the feedstock with space holder. The samples injected at 800 bar shrink more than the samples injected at 1000 bar, due to lower green density of the samples obtained at 800 bar. The sintering temperature has an influence on the shrinkage as well. The samples sintered at 1300°C shrink more than the samples sintered at 1200°C. This is already expected, as larger sintering necks are formed at higher temperatures leading to a higher densification of the material.
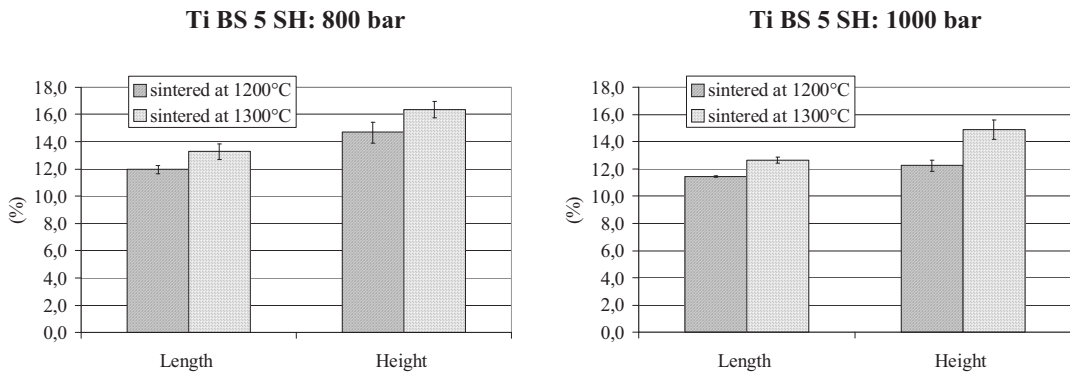

Figure 85: Sintering shrinkage of the samples. The feedstock Ti BS 4 was injected with 800 bar in both
cases. The feedstock Ti BS 5 SH was injected with maximal injection pressure of 800 bar and 1000 bar.
The sintering temperature was varied (1200 or 1300°C), other parameters fixed (3 h, vacuum). (n= 3-5)

The cross sections of the samples with the maximal injection pressures investigated are shown in Figure 86. The samples, for which both feedstocks were injected at 800 bar pressure, showed the porous and the dense structures derived from the injection of the feedstocks with and without space holder from the different injection units. In the case of the samples where the feedstock with space holder was injected at 1000 bar, sample integrity was not preserved, as the green part without space holder was broken off during injection of the feedstock with space holder. Although only the samples sintered at 1300°C are shown in the figure, the same phenomena happened also for the samples sintered at 1200°C.

Figure 86: Pictures of the cross-sections of the samples. Feedstock without space holder was injected at 800 bar, feedstock with space holder injected at 800 and 1000 bar. Sintering parameters: 1300°C, 3 h, vacuum.

The microstructure of the samples was investigated and pictures of the samples were taken at the locations indicated in Figure 87.
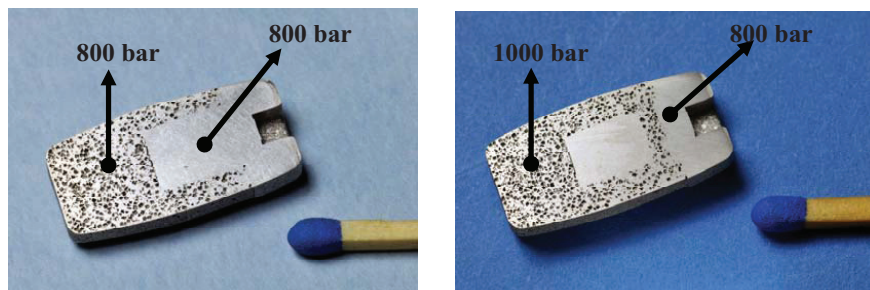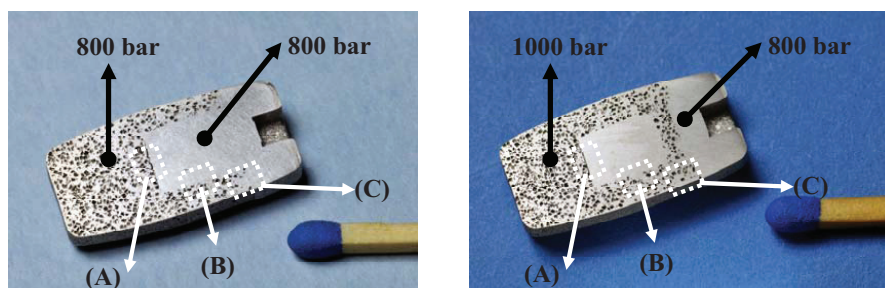

Figure 87: Pictures of the cross-sections of the samples. Feedstock without space holder was injected at 800 bar, feedstock with space holder . injected at 800 and 1000 bar. (A), (B) and (C) indicate locations where LM pictures were taken. Sintering parameters: 1300°C, 3 h, vacuum.

The LM pictures are shown in Table 25. Location (A) seems to be a critical point of interconnectivity between dense and porous parts.

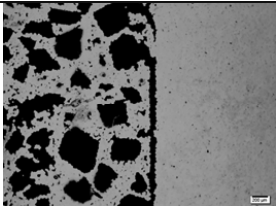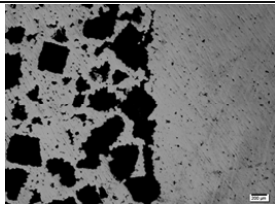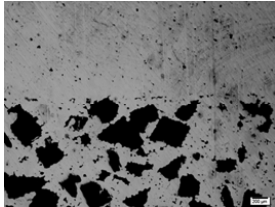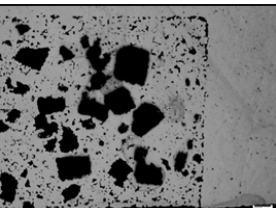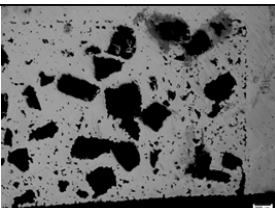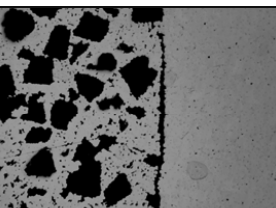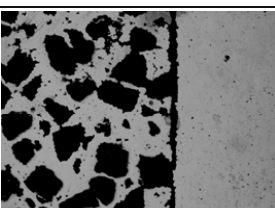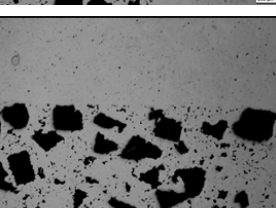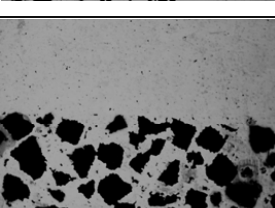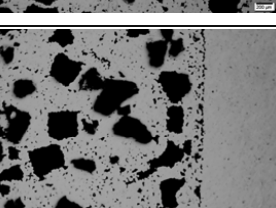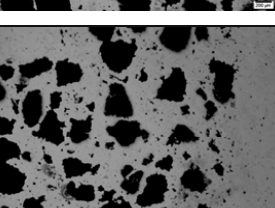At 800 bar injection pressure, the samples sintered at 1200 and 1300°C show delamination between the porous and dense areas. The greatest distance between the porous and the dense parts was measured for both sintering temperatures. The sample sintered at 1200°C shows 71 μm delamination, whereas the value for the part sintered at 1300°C is 125 μm. The lower sintering shrinkage at 1200°C seems to have contributed to a smaller delamination defect.

At 1000 bar injection pressure, the same defect is seen for the samples sintered at different temperatures. The sample sintered at 1200°C shows the lowest delamination distance found (57 μm), whereas the value for the sample sintered at 1300°C is higher (98 μm). Both values are lower as compared to the samples injected at 800 bar with the respective sintering temperatures. The higher green density of the samples injected at 1000 bar seems to have contributed to a minimisation of the delamination defect.

At location (B), all samples exhibit good interconnectivity between porous and dense areas, independent of injection pressure or sintering temperature.

Location (C) showed relative good interconnectivity between porous and dense areas. Only the sample injected at 800 bar and sintered at 1300°C showed a kind of notch at the sample surface at the interface area. This probably has occurred due to the higher sintering shrinkage at this temperature and the lower green density at 800 bar injection pressure.

Table 25: Light microscope pictures of the cross-section of implants. Feedstock without space holder always injected at 800 bar. (A), (B) and (C) indicate the locations defined in Figure 87.

		Sintering temperature, 3 hours, atmosphere: vacuum	
		1200 °C	1300°C
800 bar injection pressure of feedstock with space holder	(A)		
	(B)		
	(C)		
1000 bar injection pressure of feedstock with space holder	(A)		
	(B)		
	(C)		

The chemical impurities of one sample injected with 800 bar pressure (both feedstocks) and sintered at 1300°C were investigated and the results are shown in Table 26. The carbon level is comparable to the levels obtained for the warm pressed samples with space holder with the paraffin-based binder systems BS 1, BS 2 and BS 3 (Table 20). On the other hand, the oxygen level of the sample increased and is comparable to the level obtained for the sample with space holder with the standard binder (SB). This increase in the oxygen level is probably due to the addition of stearic acid to the feedstock BS 4 and BS 5, which were used for the fabrication of the spinal implant. Increased levels of impurity were already reported in the literature when stearic acid was employed [65].

Table 26: Oxygen and carbon contamination levels of the spinal implant as compared to the starting powder.

Sample	Oxygen (wt.%)				Carbon (wt.%)			
	Starting powder	Sintered part	Increase		Starting powder	Sintered part	Increase	
			Absolute* (wt.%)	Relative ** (-)			Absolute (wt.%)	Relative ** (-)
Spinal implant	0.18	0.34	0.16	1.9	0.01	0.06	0.05	6

* Absolute increase: contamination of sintered part – contamination of starting powder

** Relative increase: contamination of sintered part / contamination of starting powder

6 Summary and conclusion

The aim of the present work was the development of feedstocks suitable for the net-shape production of titanium spinal implants with a gradient in porosity by 2-component-metal injection moulding (2-C-MIM). The starting point of the development was a standard binder system (SB), which was the state of the art at the institute IEK-1 at *Forschungszentrum Jülich*. This binder system is suitable for the production of porous MIM parts produced with NaCl as the space holder material. The SB system is composed of 60 Vol.% amide wax (Wax C) and 40 Vol.% polyethylene wax (PE 520). With this binder system, the availability of 2-C-MIM was confirmed with the techniques investigated, namely the 2-C-sandwich-MIM and the 2-C-insertion-MIM. Cylindrical samples with a gradient in porosity were produced, but injection problems occurred due to binder-powder separation. This phase separation was attributed to the very low viscosity of the SB system. Therefore, it was concluded that this system was unsuitable for the 2-C-MIM application, especially when the vertical injection unit was used. The need for a new binder system for 2-C-MIM became obvious, where viscosity control was the key issue. Moreover, it was aspired that the partial debinding method of the SB system (wicking) is substituted by another method with industrial significance, while maintaining the suitability for the space holder method.

The SB system and a series of new binder systems (BS 1, BS 2, BS 3) based on paraffin-polyethylene mixtures were investigated, where the viscosity of the polyethylene materials was chosen so that a wide range of binder viscosities could be covered. Two types of polyethylene waxes (PE 520 and PE 190) and one polyethylene material (Hostalen GA 7260 G) were investigated. Due to its higher molecular mass, the Hostalen material is the most viscous material investigated. The same ratio of the first to the second component as in the SB system (60 / 40 Vol.%) was kept constant for the new binder systems investigated. The partial debinding method used for the new systems was solvent debinding, which is an established method in industry. During the investigation of the binder systems, the low viscosity of the SB system (0.05 Pa·s at 150°C and 100 s^{-1}) was confirmed. The BS 1 system showed a similar viscosity value (0.06 Pa·s) to that of the SB system. The BS 2 (1.1 Pa·s) and BS 3 (12.4 Pa·s) systems were more viscous than BS 1, being BS 3 the most viscous system. The system BS 3 was the one with the closest viscosity value to that one proposed in the literature for a suitable binder system (10 Pa·s). All samples were investigated at a primary working temperature (150°C), which was chosen after DSC measurements. The measurements showed a

135

displacement of melting points in the binder systems as compared to the single components, which indicates miscibility of one component in the other. This phenomenon was more significant for paraffin-based binders.

Feedstocks with the different binder systems were prepared with titanium powders at a solids loading of 68 Vol.% for the feedstocks without space holder and 75 Vol.% for the feedstocks with the space holder particles. Hereby the space holder content was kept constant at 50 Vol.% of the solids loading.

Tests with warm pressed titanium samples showed the influence of temperature on solvent debinding, which was performed in a n-hexane bath. At 25°C, only around 30 Vol. % of the total theoretical binder amount in the feedstock was removed after 48 hours; whereas around 50 Vol. % is extracted if the process is undertaken at 50°C for the same period of time. The expansion of the samples after the first debinding step was recorded. Samples with paraffin-based binder systems expand more than samples with the SB system, which undergo the wicking process. The paraffin-based system BS 3 exhibited the highest expansion among all samples. Cracks in the sintered sample were observed in the microstructure of the BS 3 sample. Nevertheless, the suitability of all systems for the space holder method was confirmed. Warm pressed samples with a gradient in porosity were produced with the systems SB, BS 1, BS 2 and BS 3.

Chemical analysis revealed that the binder system employed has influence on mainly carbon and oxygen levels of titanium samples. The chemical composition of the binder system itself is thought to be responsible for the contamination of the titanium material. For both carbon and oxygen, the contamination level is always higher for the samples with the SB system than for the paraffin-based systems. This occurs for both materials with or without space holder, as brown or sintered part. An improvement of the ASTM level of titanium samples was achieved with the use of paraffin-based binder systems, when starting from the same batch of titanium powder. In previous works in the institute, only ASTM grade 4 was achieved for samples which were produced from this powder with the SB system and NaCl as space holder. By using paraffin-based binder systems, porous titanium samples fulfilling ASTM level grade 3 (<0.35 wt.% oxygen) could be produced. These samples were only 0.02 wt.% above grade 2 (<0.25 wt.% oxygen).

After confirming the suitability of the paraffin-based binders for the production of samples with a gradient in porosity, the flowing behaviour of the systems was investigated by capillary viscosimetry. In this study, Ti powder (< 45 μm) was replaced by Fe22Cr powder (22-53 μm), The similarity in particle size distribution of the powders enabled the material substitution and

136

results comparison. Feedstocks with the low viscous binder systems SB and BS 1 showed phase separation followed by clogging of the capillary in the capillary viscometer. Further investigations with these systems were hence interrupted. Investigations with the BS 2 system showed no phase separation, but the feedstock flowed out of the capillary during the heating up phase of the viscometer, before the measurement was started. Therefore, investigations with this binder system were discontinued as well. Only the system BS 3, the more viscous one, showed satisfactory flowing behaviour during capillary tests. Therefore, the ongoing work was focused on this binder system.

The solids loading of feedstocks with the BS 3 system was further optimised with Fe22Cr powder. The viscosity of feedstocks with and without space holder was measured for various solids contents with the capillary viscometer. For the feedstock without space holder, the maximum solids loading which could be measured was 64 Vol.%, whereas 68 Vol.% was the value achieved for the feedstock with space holder particles with the same binder system. These values are lower than values used for the titanium feedstocks which were previously warm pressed. The reason for this discrepancy lays on the fact that the amount of binder used for warm pressing was not sufficient for providing sufficient feedstock flowability for capillary measurements with the BS 3 system.

For further knowledge of feedstock flowing behaviour, the influence of the addition of stearic acid was investigated in another binder system BS 4. No significant influence was detected for solids loadings lower than 60 Vol.%, but a significant reduction in viscosity was found for 64 Vol.% powder. No measurement was possible if the solids loading was increased again to 68 Vol.% powder, indicating that the critical point of the mixture was already reached at this point. This was observed for feedstocks with and without stearic acid. Due to significant reduction of viscosity near the critical point, the use of stearic acid was seen as advantageous in further feedstock formulations.

The influence of space holder particles on the flowing behaviour of feedstocks was investigated as well. Feedstocks were produced with the BS 4 binder system with space holder. The space holder particles decrease the viscosity of feedstocks as compared to feedstocks without space holder with the same solids loading. The lower viscosity of suspensions with bimodal distributions as compared to monodispersed systems was described in the literature as well. Due to the decrease on viscosity and the lower demand on binder at the same solids content, capillary measurements were possible with up to 68 Vol.% for the feedstock with the system BS 4 with space holder.

The influence of component ratio on the flowing behaviour was investigated as well. The amount of polyethylene material was reduced and feedstocks with space holder with the system BS 5 were produced. Hereby 5 Vol.% of polyethylene material was substituted by paraffin material (as compared to BS 4 system). No significant reduction of feedstock viscosity was noticed, except at high shear rates. Nevertheless, the solids loading of the feedstock with the system BS 5 could be further increased to 72 Vol.%, which was preferred regarding the dimensional accuracy of sintered samples in further processing steps.

In addition to capillary measurements, other methods are in the literature for the determination of the optimal solids loading, including tap density and torque measurements. These methods were tested and compared. Tap density delivered results in accordance to the values obtained by capillary tests, but fails to predict maximum solids loading changes when different binder systems are investigated. The method does not take into account powder-binder interaction during flow and the influence of binder viscosity. Torque measurements were found to be not advisable for determination of feedstock optimal solids loading, due to the great deviation obtained in comparison to other methods and the effort required for the measurement.

Capillary tests with the titanium feedstocks with the binder systems BS 4 (without space holder, 64 Vol.% solids loading) and BS 5 (with space holder, 72 Vo.% solids loading) were performed in order to optimise the working temperature and select a suitable injecting temperature for tests with the MIM machine. Hereby, the preferred injection temperature was selected as 140°C.

Prototypes of a titanium spinal implant could be successfully produced in the 2-C-MIM machine with an automated mould. The maximal injection pressure was varied for both feedstocks and green parts with 800 and 1000 bar maximal injection pressure of the feedstock with space holder were further processed until sintering. Samples were debinded at 50°C for 48 hours in hexane, desalinated for 48 h in water at 60°C and sintered for 3 h in vacuum at 1200 and 1300°C. Independent of the sintering temperature, a small delamination remained at the interface between porous and dense parts inside the samples. Problems were seen in the samples injected at 1000 bar, as green part integrity was not preserved during injection, which is probably caused by the construction of the mould.

The chemical impurities of one prototype of the spinal implant revealed that the carbon level is comparable to the levels obtained for the warm pressed samples with space holder with the paraffin-based binder systems. On the other hand, the oxygen level of the sample increased and is comparable to the level obtained for the sample with space holder with the standard

138

binder (SB). This increase in the oxygen level is probably due to the addition of stearic acid to the feedstock BS 4 and BS 5, which were used for the fabrication of the spinal implant. Despite the increase in oxygen content, the spinal implants still fulfil ASTM grade 3 (< 0.35 wt.% oxygen).

For future works, investigation of other injection parameters than the injection pressure is recommended for further improvement of adhesion between dense and porous areas of the spinal implants. The injection moulding procedure is an elaborated one, where the influence of one parameter on another and on the final part is unique for a specific system. This is especially the case for systems where more than one component is involved, as it is the case of the 2-C-MIM technique. Additionally to injection parameters, finer tuning of feedstock solids loading may contribute to better adhesion between dense and porous parts in the implant, as sintering shrinkage of feedstocks can be varied in this way. Another suggestion for improvement of the 2-C-MIM process is the enhancement of mould design. Repositioning of the injection channel inside the implant mould used would probably preserve green part integrity if high injection pressures are employed.

The increase of the space holder content remains an open challenge to future works. In this work and in previous works at the institute, the maximal space holder content in feedstocks which could be injected at the MIM machine was 50 Vol. %. For a closer proximity to the spinal implant available in the market, a porosity of 65 Vol. % is desirable to match the requirements of the application. Further improvement of the available binder system is recommended for the increase of the space holder content in the feedstock.

Maintaining the open porosity at the surface of the final part is another necessary improvement. One suggestion in this direction is the mechanical treatment of green or sintered parts in a fluidized bed with abrasive materials in order to remove the outer metal layer of the sample.

References

1. Williams, D.F., *Titanium for medical applications*, in *Titanium in medicine: material science, surface science, engineering, biological responses and medical applications*, D.M.T. Brunette, P.; Textor, M.; Thomsen, P., Editor 2001, Springer: Berlin.

2. Wintermantel, E.H., S. W., *Biokompatible Werkstoffe und Bausweisen*, ed. Springer1998.

3. Ratner, B.D., *A perpective in titanium biocompatibility*, in *Titanium in medicine: material science, surface science, engineering, biological responses and medical applications*, D.M.T. Brunette, P.; Textor, M.; Thomsen, P., Editor 2001, Springer: Berlin.

4. Perren, S.M.P., O. E. M.; Schneider, E., *Titanium as implant material for osteosynthesis applications*, in *Titanium in medicine: materials science, surface science, engineering, biological responses and medical applications*, Springer, Editor 2001.

5. Geetha, M.S., A. K.; Asokamani, R.; Gogia, A. K., *Ti-based biomaterials, the ultimate choice for orthopaedic implants - a review.* Progress in Materials Science, 2009. **54**: p. 397-425.

6. Imwinkelreid, T., *Mechanical properties of open-pore titanium foam.* Journal of Biomedical Materials Research Part A, 2007. **81A**(4): p. 964-970.

7. Köhl, M.B., M.; Moser, A.; Buchkremer, H. P.; Beck, T.; Stöver, D., *Characterisation of porous, net-shaped NiTi alloy regarding its damping and energy-absorbing capacity.* Materials Science and Engineering A, 2011. **528**: p. 2454-2462.

8. Thieme, M.W., K. P.; Bergner, F.; Scharnweber, D.; Worch, H.; Ndop, J.; kim, T. J.; Grill, W., *Titanium powder sintering for preparation of porous functionally graded material destined for orthopaedic implants.* Journal of Materials science: Materials in Medicine, 2001. **12**: p. 225-231.

9. Windler, M.K., R., *Titanium for hip and knee protheses* in *Titanium in medicine: materials science, surface science, engineering, biological responses and medical applications*, D.M.T. Brunette, P.; Textor, M.; Thomsen, P., Editor 2001, Springer.

10. Boyan, B.D.D., D. D.; Lohmann, C. H.; Cochran, D. L.; Sylvia, V. L.; Schwartz, Z., *The titanium-bone interface in vitro: the role of the surface in promoting osteointegration*, in *Titanium in medicine: materials science, surface science, engineering, biological responses and medical applications*, Springer, Editor 2001, Springer.

11. www.zimmer.com.

12. Fujibayashi, S.N., M.; Kim, H. M.; Kokubo, T.; Nakamura, T., *Osteoinduction of porous bioactive titanium metal.* Biomaterials, 2004. **25**: p. 443-450.

13. Hulbert, S.F.Y., F. A.; Mathews, R. S.; Klawitter, J. J.; Talbert, C. D.; Stelling, F. H., *Potential of ceramic materials as permanently omplantable skeletal protheses.* Journal of Biomedical Materials Research, 1970. **4**: p. 433-456.

14. Bobyn, J.D.P., R. M.; Cameron, H. U.; Weatherly, G. C., *The optimum pore size for the fixation of porous-surfaced metal implants by the ingrowth of bone.* Clinical Orthopaedics and related research, 1980. **150**: p. 263-270.

15. Pilliar, R.M., *Porous biomaterials*, in *Concise Encyclopedia of Medical & Dental Materials*, D. Williams, Editor 1990, Pergamon Press.

16. Ashby, M.E., A.; Fleck, N. A.; Gibson, L.J.; Hutchinson, J. W.;Wadley, H. N. G., *Metal foams: a design guide*2000: Elsevier.

17. Ryan, G.P., A.; Apatsidis, D. P., *Fabrication methods of porous metals for use in orthopaedic applications.* Biomaterials, 2006. **27**: p. 2651-2670.

18. Dunand, D.C., *Processing of titanium foams.* Advanced Engineering Materials, 2004. **6**: p. 369-376.

19. Kearns, M.W.B., P. A.; Barber, A. C.; Farthing, T. W., *Manufacture of a novel porous metal.* International Journal of Powder Metallurgy, 1988. **24**: p. 59-64.

20. Davis, N.G.T., J.; Schuh, C.; Dunand, D. C., *Solid-state foaming of titanium by superelastic expansion of argon-filled pores.* Journal of Materials Research, 2001. **16**: p. 1508-1519.

21. Quadbeck, P.K., K.; Hauser, R.; Standke, G.; Adler, J.; Stephani, G.; Kieback, B., *Structural and Material Design of Open-Cell Powder Metallurgical Foams.* Advanced Engineering Materials, 2011.

22. Zardiackas, L.D.P., D. E.; Dillon, L. D.; Mitchell, D. W.; Nunnery, L. A.; Poggie, R., *Structure, metallurgy, and mechanical properties of a porous tantalum foam.* Journal of Biomedical Materials Research Part A, 2001. **58**(2): p. 180-187.

23. Hahn, H.P., W., *Preliminary evaluation of porous metal surface titanium for orthopedic implants.* Journal of Biomedical Materials Research, 1970. **4**: p. 571-577.

24. Yang, Y.Z.T., J. M.; Tian, J. T.; Chen, Z. Q.; Deng, X. J.; Zhang, D. H., *Preparation of graded porous titanium coatings on titanium implant materials by plasma spraying.* Journal of Biomedical Materials Research, 2000. **52**: p. 333-337.

25. Munir, Z.A.A.-T., U., *Self-propagating exothermic reactions: the syntheis of high-temperature materials by combustion.* Materials Science Report, 1989. **3**: p. 277-365.

26. Li, B.Y.R., L. J.; Li, Y. Y.; Gjunter; V. E., *Synthesis of porous NiTi shape memory alloys by self-propagating high-temperature synthesis: reaction mechanism and anisotropy in pore structure.* Acta Materialia, 2000. **48**: p. 3895-3904.

27. Yi, H.C.M., J.J., *Combustion synthesis of TiNi intermetallic compounds Part 1.* Journal of Materials Science. **24**: p. 3449-3455.

28. Curodeau, A.S., E.; Caldarise, S., *Design and fabrication of cast orthopedic implants with free form surface textures from 3-D printed ceramic shell.* J. Biomed. Mater. Res., 2000. **53**: p. 525-535.

29. Heinl; P.; Müller, L.K., C.; Singer, R. F.; Müller, F. A., *Cellular Ti-6Al-4V structures with interconnected macro porosity for bone implants fabricated by selective electron beam melting.* Acta Biomaterialia, 2008. **4**: p. 1536-1544.

30. Heinl, P.R., A.; Körner C.; Singer, R. F., *Cellular Titanium by Selective Electron Beam Melting.* Advanced Engineering Materials, 2007. **9**.

31. Lin, C.Y.W., T.; LaMarca, F.; Hollister, S. J., *Structural and mechanical evaluations of a topology optimised titanium interbody fusion cage fabricated by selective laser melting process.* Journal of Biomedical Materials Research Part A, 2007. **83**: p. 272-279.

32. www.arcam.com.

33. Qiu, J.D., J. T.; Lifland, M. I.; Okazaki, K., *Composite titanium dental implant fabricated by electro-discharge compaction.* Biomaterials, 1997. **18**: p. 153-160.

34. Lifland, M.I.O., K., *Properties of titanium dental implants produced by electro-discharge compaction.* Clinical Materials, 1994. **17**: p. 203-209.

35. Bram, M.S., C.; Buchkremer, H. P.; Stöver, D.; Baur, H., *High-porosity titanium, stainless steel and superalloy parts.* Advanced Engineering Materials, 2000. **2**: p. 196-199.

36. Wen, C.E.Y., Y.; Shimojima, K.; Chino, Y.; Hosokawa, H.; Mabuchi, M., *Compressibility of porous magnesium foam: dependency on porosity and pore size.* Material Letters, 2004. **58**: p. 357-360.

37. Jiang, B.Z., N. Q.; Shi, C. S.; Li, J. J., *Processing of open cell aluminum foams with tailored porous morphology.* Scripta Materialia, 2005. **53**: p. 781-785.

38. German, R.M., *Injection molding of metals and ceramics*1997.

39. Hwang, K.S.T., T. H., *Thermal debinding of powder injection moulded parts: observations and mechanisms.* Metallurgical Transactions A, 1992. **23**: p. 2775-2782.

40. Kryachek, V.M., *Injection molding.* Powder metallurgy and metal ceramics, 2004. **43**(7-8): p. 336-348.

41. Rak, Z.S., *New trends in powder injection molding.* Powder metallurgy and metal ceramics, 1999. **38**(3-4): p. 126-132.

42. Malloy, R.A., *Plastic part design for injection molding: an introduction*, ed. Hanser1994.

43. Rosato, D.V.R., Donald V.; Rosato, Marlene G., *Injection molding handbook : the complete molding operation technology, performance, economics*1986, New York.

44. Heaney, D.S., P.; German, R. M. *Two-color injection molding of hard and soft metal alloys*. in *International Conference on Functionally Graded Materials*. 2002. Denver, CO, United States: Metal Powder Industries Federation.

45. Heaney, D.S., P.; German, R. M., *Defect-free sintering of two material powder injection molded components.* Journal of Materials Science, 2003. **38**: p. 4869-4874.

46. Loibl, H.B., H; Gornik, C.; Griesmayer, E.; Kukla, C.; Zlatkov. B., *2-Komponenten-Pulverspritzgießen.* Österr. Kunststoff-Zeitschrift, 2003. **34**: p. 258-260.

47. Baumann, A., Moritz, T. , Lenk, R. *Manufacturing of ceramic-metal composites using multi-component injection molding*. in *Euro PM*. 2007.

48. Hartwig, T. *2C-Molding for MIM*. in *Euro PM*. 2007.

49. Nishiyabu, K.M., S. and Tanaka, S., *Fabrication and Mechanical Properties of Functionally Graded Micro Porous Metals by Mim-Base Powder Space Holder Method*, in *Sandwich Structures 7: Advancing with Sandwich Structures and Materials*, Springer, Editor 2005.

50. Alcock, J., *Co-injection promises further growth for MIM.* Metal Powder Report, 1999. **54**(6): p. 30-35.

51. Alcock, J.L., P. M. ; Stephenson, D. J., *Surface engineering by co-injection molding.* Surface and coatings technology, 1998. **105**: p. 65-71.

52. Foong, M.L., Tam, K.C., *Application of polymer technology to metal injection molding (MIM)*, in *Advanced polymer processing operations*, N.P. Cheremisinoff, Editor 1998, Noyes Publications: New Jersey, USA.

53. Wiech, J.R.E., *MIM binder systems and basic feedstock design*, in *Metal Injection Moulding*, M.P.I.F. K. E. Moyer (ed.), Editor 1988: Princeton, NJ. p. 19-34.

54. Brandrup, J., *Polymer handbook*1975.

55. M. L. Foong, K.C.T., *Application of polymer technology to metal injection molding (MIM)*, in *Advanced polymer processing operations*, N.P. Cheremisinoff, Editor 1998, Noyes Publications: New Jersey, USA.

56. Uwe Wolfmeier, H.S., Franz-Leo Heinrichs, Georg Michalczyk, Wolfgang Payer, Wolfram Dietsche, Klaus Boehlke, Gerd Hohner, Josef Wildgruber, *Waxes*, in *Ullmann's Encyclopedia of Industrial Chemistry*2000, Wiley-VCH Verlag GmbH & Co. KGaA: Weinheim.

57.   Weber, P.D., H. L., *Solubility of paraffin in pure hydrocarbons.* Industrial and engineering chemistry, 1928. **20**: p. 383-384.

58.   Freund, M.C., R.; Keszthelyi, S.; Mozes, Gy., *Paraffin products: properties, technologies, applications*, ed. A. Kiado1982, Budapest.

59.   SciFinder.

60.   Elias, H.G., *Plastics, General survey*, in *Ullmann's Encyclopedia of Industrial Chemistry*2005.

61.   Kenneth S. Whiteley, T.G.H., Hartmut Koch, Ralph L. Mawer, Wolfgang Immel, *Polyolefins*, in *Ullmann's Encyclopedia of Industrial Chemistry*2000, Wiley-VCH Verlag GmbH & Co. KGaA.

62.   Bowden, F.P.T., D., *The friction and lubrication of solids*2001: Oxford University Press.

63.   Edirisinghe, M.J., *The effect of processing additives on the properties of a ceramic-polymer formulation* Ceramics International, 1991. **17**(2): p. 89-96

64.   Evans, J.R.G., *Interfacial aspects of ceramic injection moulding*, in *Surface and colloid chemistry in advanced ceramics processing*, R.J.B. Pugh, L., Editor 1993, CRC Press.

65.   Lin, S.T. and R.M. German, *Interaction between binder and powder in injection moulding of alumina.* Journal of Materials Science, 1994. **29**(19): p. 5207-5212.

66.   Johansson, E.N., L., *XPS study of carboxylic acid layers on oxidized metals with reference to particulate materials.* Surface and Interface Analysis, 2003. **35**: p. 375-381.

67.   Kosswig, K., *Surfactants*, in *Ullmann's Encyclopedia of Industrial Chemistry*2005.

68.   Hwang, K.S., *Fundamentals of debinding processes in powder injection moulding.* Reviews in particulate materials, 1996. **4**: p. 71-103.

69.   Ter Maat, J.H.H.E., J., *Fast catalytic debinding of injection moulded parts*, in *4 th Int Symp Ceramic Materials and Components for Engines*1991: Goteborg.

70.   Lin, S.T.G., R. M., *Extraction debinding of injection molded parts by condensed solvent.* Powder Metallurgy International, 1989. **21**(5): p. 19-24.

71.   Wu, Y.W., R.; Kwon, Y. S.; Park, S. J.; German, R. M., *Injection moulding of HDH titanium powder.* International Journal of Powder Metallurgy, 2006. **42**(3): p. 59-66.

72.   Bakan, H.I.J., Y.; Messer, P. F.; Davies, H. A.; Ellis, B., *Study of processing parameters for MIM feedstock based on composite PEG-PMMA binder.* Powder metallurgy, 1998. **41**(4): p. 289-291.

73.   Shivashankar, T.S. and R.M. German, *Effective Length Scale for Predicting Solvent-Debinding Times of Components Produced by Powder Injection Molding*
doi:10.1111/j.1151-2916.1999.tb01888.x. Journal of the American Ceramic Society, 1999. **82**(5): p. 1146-1152.

74.   Westcot, E.J.B., C.; German, R. M., *In situ dimensional change, mass loss and mechanisms for solvent debinding of powder injection moulded components.* Powder metallurgy, 2003. **46**: p. 61-67.

75.   Tsai, D.S.C., W. W., *Solvent debinding kinetics of alumina gree bodies by powder injection moulding.* Ceramics International, 1995. **21**: p. 257-264.

76.   Köhl, M.H., T.; Bram, M.; Buchkremer, H. P.; Stöver, D.; Köller, M., *Powder Metallurgical Near-Net-Shape Fabrication of Porous NiTi Shape Memory Alloys for Use as Long-Term Implants by the Combination of the Metal Injection Molding Process with the Space-Holder Technique.* Advanced Engineering Materials, 2009. **11**.

77. H. Bockhorn , A.H., U. Hornung and D. Schawaller, *Kinetic study on the thermal degradation of polypropylene and polyethylene.* Journal of Analytical and Applied Pyrolysis, 1999. **48**(2): p. 93-109.

78. Allen, N.E., M., *Fundamentals of polymer degradation an stabilisation*1992.

79. Holland, B.J.H., J. N., *The kinetics and mechanisms of the thermal degradation of poly(methyl methacrylate) studied by thermal analysis-Fourier transform spectroscopy.* Polymer, 2001. **42**: p. 4825-4835.

80. Petzoldt, F., Eifert, H., Hartwig, T., Veltl, G., *Binder design and process control for high performance MIM-materials.* Advances in powder metallurgy & particulate materials, 1995. **2**: p. 6.

81. German, R.M., *Theory of thermal debinding.* International Journal of Powder Metallurgy, 1987. **23**(4): p. 237-245.

82. Aggarwal, G., Park, S-J., Smid, I. German, R. M., *Master decomposition curve for binders used in powder injection molding.* Metallurgical and Materials Transactions A, 2007. **38**(3): p. 606-614.

83. Shengjie, Y.L., Y. C.; Yu, S.C.M.; Tam, K.C., *Thermal debinding modelling of mass transport and deformation in powder injection moulding compact.* Metallurgical and Materials Transactions B, 2002. **33B**: p. 477-488.

84. Haorong Zhang, R.M.G., Animesh Bose, *Wick debinding distortion of injection molded powder compacts.* International Journal of Powder Metallurgy, 1990. **26**(3): p. 217-230.

85. Sohn, H.Y.M., C., *The effect of particle size distribution on packing density.* The Canadian Journal of Chemical Engineering, 1968. **46**.

86. Rei, M.M., E. C.; Gomes, R. M.; Schaefffer, L.; Souza, J. P., *Low-pressure injection moulding processing of a 316-L stainless steel feedstock.* Material Letters, 2001. **52**: p. 360-365.

87. Ozkan Gulsoy, H. and C. Karatas, *Development of poly(2-ethyl-2-oxaline) based water-soluble binder for injection molding of stainless steel powder.* Materials & Design, 2007. **28**(9): p. 2488-2491.

88. Jorge, H., Cunha, A. M. *Development of a water-soluble binder for PIM: effect of the backbone polymer and surfactant.* in *Euro PM.* 2007.

89. Kitano, T.K., T.; Shirota, T., *An empirical equation of the relative viscosity of polymer melts filled with various inorganic fillers.* Rheologica Acta, 1981. **20**: p. 207-209.

90. Maron, S.H.P., P. E., *Application of Ree-Erying generalized flow theory to suspensions of spherical particles.* Journal of Colloid Science, 1956. **11**: p. 80-95.

91. Metzner, A.B., *Rheology of suspensions in polymeric liquids.* Journal of Rheology, 1985. **29**: p. 739-775.

92. German, R.M., *Optimization of the powder-binder mixture for powder injection molding.* Advances in powder metallurgy & particulate materials, 1989. **3**: p. 51-65.

93. Chung, C.I., Rhee, B. O., Cao, M. Y., Liu, C. X., *Requirements of binder for powder injection molding.* Advances in powder metallurgy & particulate materials, 1989. **3**: p. 67-78.

94. Darby, R., *Chemical Engineering Fluid Mechanics.* Second ed2001: Marcel Dekker.

95. Remmler, T., *Bestimmung der Fließeigenschaften von keramischen Massen mit einem Doppelkappilar-Rheometer*, Malvern Instruments.

96. Mutsuddy, B.C.F., R. G., *Ceramic Injection Moulding.* Materials Technology Series1994: Springer.

97. Dihoru, L.V.S., Lyndon M.; Orban, R.; German, Randall M., *Experimental study and neural network modelling of the stability of powder injection moulding feedstocks.* Materials and manufacturing processes, 2000. **15**(3): p. 419-438.

98. Goto, H.a.K., H., *Flow of suspensions containing particles of two different sizes through a capillary tube.* Journal of Rheology, 1982. **26**: p. 387-398.

99. Chong, J.S.C., E. B.; Baer, A. D., *Rheology of concentrated suspensions.* Journal of Applied Polymer Science, 1971. **15**: p. 2007-2021.

100. Bram, M.L., A.; Buchkremer, H. P.; Stöver, D., *Herstellung von hochporössen, endkonturnahen Titan-Formkörpern für biomedizinische Anwendungen.* Materialwissenschaft und Werkstofftechnik, 2004. **35**: p. 213-218.

101. Laptev, A.B., M.; Buchkremer, H. P.; Stöver, D., *Study of production route for titanium parts combining very high porosity and complex shape.* Powder metallurgy, 2004. **47**: p. 85-92.

102. Schiefer, H.B., M.; Buchkremer, H.P:; Stöver, D., *Mechanical examinations of dental implants with porous titanium coating.* J. Mat. Sci.: Materials in medicine, 2009. **20**: p. 1763-1770.

103. Steffen, T.K., J. J.; Karabasz, D.; Bobyn, J. D. *Bone ingrowth into porous titanium foam implants - a histological and mechanical study.* in *51th Annual Meeting of the Orthopaedic Research Society, Poster No. 1396.* 2005.

104. www.synthes.com.

105. Ferri, O.M.E., T.; Bormann, R., *High cycle fatigue behaviour of Ti6Al4V fabricated by metal injection moulding technology.* Materials Science and Engineering A, 2009. **504**: p. 107-113.

106. Aust, E.L., W.; Gerling, R.; Oger B.; Ebel, Th., *Herstellung einer komplexen Titan-Knochenschraube aus Metallpulverspritzguss.* Mat.-wiss. u. Werkstofftech., 2005. **36**(423-428).

107. *Innovatives Spritzgießen von Titan, Company Broschure*, T.M. GmbH, Editor 2008.

108. Bidaux, J.E.J., A.; Zufferey, D.; Carreno Morelli, E. *Metal injection moulding of NiTi shape memory alloys.* in *Euro PM.* 2007. Toulouse: Europena Powder Metallurgy Association.

109. Weil, K.S.N., E.; Simmons, K., *A new binder for powder injection molding titanium and other reactive metals.* Journal of materials processing technology, 2006. **176**: p. 205-209.

110. Dropmann, M., *Pulvermetallurgischer Spritzguß von Niob-Superlegierungen*, 1993, Forschungszentrum Jülich.

111. Fuest, C., *Formgebung von Molybdän- und Titansiliziden über das Pulvermetallformspritzen*, 1994, Forschungszentrum Jülich.

112. Köhl, M., *Pulvermetallurgie hochporöser NiTi-Legierungen für Implantat- und Dämpfungsanwendungen*, in *IEF-1*2009, Ruhr-Universität-Bochum: Jülich.

113. Krone, L., *Metal Injection Moulding (MIM) von NiTi Bauteilen mit Formgedächtniseigenschaften*, 2005, Ruhr-Universität Bochum: Jülich.

114. Bobyn, J.D.T., M.; Miller, J. E., *Fundamental principles of biological fixation*, in *Reconstructive surgery of the joints*, B.F. Morrey, Editor 1996.

115. Lin, T.-Y.C.S.-T., *Effects of stearic acid on the injection moulding of alumina.* J. Am. Ceram. Soc., 1995. **10**: p. 2746-52.

116. S. T. Lin, R.M.G., *The influence of powder loading and binder additive on the properties of alumina injection moulded blends.* Journal of Materials Science, 1994. **29**: p. 5367-5373.

117. Cepeda, B.C.E., *Solubilities of stearic acid in organic solvents and in azeotropic solvent mixtures.* J. Chem. Eng. Data, 2008. **53**: p. 628-633.

118. www.arburg.de.

119. Arburg, *Handbuch Spezialverfharen Pulverspritzgießen*, 2008: Loßburg, Germany.

120. Keattch, C.J.D., D., *An introduction to thermogravimetry*1975: Heyden.

121. Menges, G., *Werkstoffkunde Kunststoff*1998.

146

122. Christopher J. Pipe, T.S.M.a.G.H.M., *High shear rate viscometry.* Rheologica Acta, 2008. **47**(5-6): p. 621-642.

123. Instruments, M., *Rosand RH2000 user manual*, 2006: United Kingdom.

124. Smith, J.M.V.N., H. C.; Abbott, M. M., *Introduction to Chemical Engineering Thermodynamics*1996: Mc-Graw-Hill Internationa Editions.

125. Kendall, J.M., K. P., *The viscosity of liquids. II. The viscosity-composition curve for ideal liquid mixtures.* The Journal of the American Chemical Society, 1917. **9**: p. 1787-1802.

126. A., V.d.W.A.J., *Viscosity of binary liquids.* Nature, 1936. **138**: p. 845-846.

127. Lide, D.R., Hrsg., *CRC Handbook of chemistry and physics*. 86th ed2005: Boca Raton, Fla. : Taylor and Francis.

128. de Gennes, P.G., *Wetting:statics and dynamics.* Reviews of Modern Physiks, 1985. **57**(3): p. 827-861.

References

148

Schriften des Forschungszentrums Jülich
Reihe Energie & Umwelt / Energy & Environment

11. **Kerosinreformierung für Luftfahrtanwendungen**
von R. C. Samsun (2008), VII, 218 Seiten
ISBN: 978-3-89336-531-9

12. **Der 4. Deutsche Wasserstoff Congress 2008 – Tagungsband**
hrsg. von D. Stolten, B. Emonts, Th. Grube (2008), 269 Seiten
ISBN: 978-3-89336-533-3

13. **Organic matter in Late Devonian sediments as an indicator for environmental changes**
by M. Kloppisch (2008), XII, 188 pages
ISBN: 978-3-89336-534-0

14. **Entschwefelung von Mitteldestillaten für die Anwendung in mobilen Brennstoffzellen-Systemen**
von J. Latz (2008), XII, 215 Seiten
ISBN: 978-3-89336-535-7

15. **RED-IMPACT**
Impact of Partitioning, Transmutation and Waste Reduction Technologies on the Final Nuclear Waste Disposal
SYNTHESIS REPORT
ed. by W. von Lensa, R. Nabbi, M. Rossbach (2008), 178 pages
ISBN 978-3-89336-538-8

16. **Ferritic Steel Interconnectors and their Interactions with Ni Base Anodes in Solid Oxide Fuel Cells (SOFC)**
by J. H. Froitzheim (2008), 169 pages
ISBN: 978-3-89336-540-1

17. **Integrated Modelling of Nutrients in Selected River Basins of Turkey**
Results of a bilateral German-Turkish Research Project
project coord. M. Karpuzcu, F. Wendland (2008), XVI, 183 pages
ISBN: 978-3-89336-541-8

18. **Isotopengeochemische Studien zur klimatischen Ausprägung der Jüngeren Dryas in terrestrischen Archiven Eurasiens**
von J. Parplies (2008), XI, 155 Seiten, Anh.
ISBN: 978-3-89336-542-5

19. **Untersuchungen zur Klimavariabilität auf dem Tibetischen Plateau - Ein Beitrag auf der Basis stabiler Kohlenstoff- und Sauerstoffisotope in Jahrringen von Bäumen waldgrenznaher Standorte**
von J. Griessinger (2008), XIII, 172 Seiten
ISBN: 978-3-89336-544-9

20. **Neutron-Irradiation + Helium Hardening & Embrittlement Modeling of 9%Cr-Steels in an Engineering Perspective (HELENA)**
    by R. Chaouadi (2008), VIII, 139 pages
    ISBN: 978-3-89336-545-6

21. **in Bearbeitung**

22. **Verbundvorhaben APAWAGS (AOEV und Wassergenerierung) – Teilprojekt: Brennstoffreformierung – Schlussbericht**
    von R. Peters, R. C. Samsun, J. Pasel, Z. Porš, D. Stolten (2008), VI, 106 Seiten
    ISBN: 978-3-89336-547-0

23. **FREEVAL**
    Evaluation of a Fire Radiative Power Product derived from Meteosat 8/9 and Identification of Operational User Needs
    Final Report
    project coord. M. Schultz, M. Wooster (2008), 139 pages
    ISBN: 978-3-89336-549-4

24. **Untersuchungen zum Alkaliverhalten unter Oxycoal-Bedingungen**
    von C. Weber (2008), VII, 143, XII Seiten
    ISBN: 978-3-89336-551-7

25. **Grundlegende Untersuchungen zur Freisetzung von Spurstoffen, Heißgaschemie, Korrosionsbeständigkeit keramischer Werkstoffe und Alkalirückhaltung in der Druckkohlenstaubfeuerung**
    von M. Müller (2008), 207 Seiten
    ISBN: 978-3-89336-552-4

26. **Analytik von ozoninduzierten phenolischen Sekundärmetaboliten in *Nicotiana tabacum* L. cv Bel W3 mittels LC-MS**
    von I. Koch (2008), III, V, 153 Seiten
    ISBN 978-3-89336-553-1

27. **IEF-3 Report 2009. Grundlagenforschung für die Anwendung**
    (2009), ca. 230 Seiten
    ISBN: 978-3-89336-554-8

28. **Influence of Composition and Processing in the Oxidation Behavior of MCrAlY-Coatings for TBC Applications**
    by J. Toscano (2009), 168 pages
    ISBN: 978-3-89336-556-2

29. **Modellgestützte Analyse signifikanter Phosphorbelastungen in hessischen Oberflächengewässern aus diffusen und punktuellen Quellen**
    von B. Tetzlaff (2009), 149 Seiten
    ISBN: 978-3-89336-557-9

30. **Nickelreaktivlot / Oxidkeramik – Fügungen als elektrisch isolierende Dichtungskonzepte für Hochtemperatur-Brennstoffzellen-Stacks**
von S. Zügner (2009), 136 Seiten
ISBN: 978-3-89336-558-6

31. **Langzeitbeobachtung der Dosisbelastung der Bevölkerung in radioaktiv kontaminierten Gebieten Weißrusslands – Korma-Studie**
von H. Dederichs, J. Pillath, B. Heuel-Fabianek, P. Hill, R. Lennartz (2009), Getr. Pag.
ISBN: 978-3-89336-532-3

32. **Herstellung von Hochtemperatur-Brennstoffzellen über physikalische Gasphasenabscheidung**
von N. Jordán Escalona (2009), 148 Seiten
ISBN: 978-3-89336-532-3

33. **Real-time Digital Control of Plasma Position and Shape on the TEXTOR Tokamak**
by M. Mitri (2009), IV, 128 pages
ISBN: 978-3-89336-567-8

34. **Freisetzung und Einbindung von Alkalimetallverbindungen in kohlebefeuerten Kombikraftwerken**
von M. Müller (2009), 155 Seiten
ISBN: 978-3-89336-568-5

35. **Kosten von Brennstoffzellensystemen auf Massenbasis in Abhängigkeit von der Absatzmenge**
von J. Werhahn (2009), 242 Seiten
ISBN: 978-3-89336-569-2

36. **Einfluss von Reoxidationszyklen auf die Betriebsfestigkeit von anodengestützten Festoxid-Brennstoffzellen**
von M. Ettler (2009), 138 Seiten
ISBN: 978-3-89336-570-8

37. **Großflächige Plasmaabscheidung von mikrokristallinem Silizium für mikromorphe Dünnschichtsolarmodule**
von T. Kilper (2009), XVII, 154 Seiten
ISBN: 978-3-89336-572-2

38. **Generalized detailed balance theory of solar cells**
by T. Kirchartz (2009), IV, 198 pages
ISBN: 978-3-89336-573-9

39. **The Influence of the Dynamic Ergodic Divertor on the Radial Electric Field at the Tokamak TEXTOR**
von J. W. Coenen (2009), xii, 122, XXVI pages
ISBN: 978-3-89336-574-6

40. **Sicherheitstechnik im Wandel Nuklearer Systeme**
von K. Nünighoff (2009), viii, 215 Seiten
ISBN: 978-3-89336-578-4

41. **Pulvermetallurgie hochporöser NiTi-Legierungen für Implanat- und Dämpfungsanwendungen**
von M. Köhl (2009), XVII, 199 Seiten
ISBN: 978-3-89336-580-7

42. **Einfluss der Bondcoatzusammensetzung und Herstellungsparameter auf die Lebensdauer von Wärmedämmschichten bei zyklischer Temperaturbelastung**
von M. Subanovic (2009), 188, VI Seiten
ISBN: 978-3-89336-582-1

43. **Oxygen Permeation and Thermo-Chemical Stability of Oxygen Permeation Membrane Materials for the Oxyfuel Process**
by A. J. Ellett (2009), 176 pages
ISBN: 978-3-89336-581-4

44. **Korrosion von polykristallinem Aluminiumoxid (PCA) durch Metalljodidschmelzen sowie deren Benetzungseigenschaften**
von S. C. Fischer (2009), 148 Seiten
ISBN: 978-3-89336-584-5

45. **IEF-3 Report 2009. Basic Research for Applications**
(2009), 217 Seiten
ISBN: 978-3-89336-585-2

46. **Verbundvorhaben ELBASYS (Elektrische Basissysteme in einem CFK-Rumpf) - Teilprojekt: Brennstoffzellenabgase zur Tankinertisierung - Schlussbericht**
von R. Peters, J. Latz, J. Pasel, R. C. Samsun, D. Stolten
(2009), xi, 202 Seiten
ISBN: 978-3-89336-587-6

47. **Aging of ^{14}C-labeled Atrazine Residues in Soil: Location, Characterization and Biological Accessibility**
by N. D. Jablonowski (2009), IX, 104 pages
ISBN: 978-3-89336-588-3

48. **Entwicklung eines energetischen Sanierungsmodells für den europäischen Wohngebäudesektor unter dem Aspekt der Erstellung von Szenarien für Energie- und CO_2 - Einsparpotenziale bis 2030**
von P. Hansen (2009), XXII, 281 Seiten
ISBN: 978-3-89336-590-6

49. **Reduktion der Chromfreisetzung aus metallischen Interkonnektoren für Hochtemperaturbrennstofzellen durch Schutzschichtsysteme**
von R. Trebbels (2009), iii, 135 Seiten
ISBN: 978-3-89336-591-3

50. **Bruchmechanische Untersuchung von Metall / Keramik-Verbundsystemen für die Anwendung in der Hochtemperaturbrennstoffzelle**
von B. Kuhn (2009), 118 Seiten
ISBN: 978-3-89336-592-0

51. **Wasserstoff-Emissionen und ihre Auswirkungen auf den arktischen Ozonverlust**
Risikoanalyse einer globalen Wasserstoffwirtschaft
von T. Feck (2009), 180 Seiten
ISBN: 978-3-89336-593-7

52. **Development of a new Online Method for Compound Specific Measurements of Organic Aerosols**
by T. Hohaus (2009), 156 pages
ISBN: 978-3-89336-596-8

53. **Entwicklung einer FPGA basierten Ansteuerungselektronik für Justageeinheiten im Michelson Interferometer**
von H. Nöldgen (2009), 121 Seiten
ISBN: 978-3-89336-599-9

54. **Observation – and model – based study of the extratropical UT/LS**
by A. Kunz (2010), xii, 120, xii pages
ISBN: 978-3-89336-603-3

55. **Herstellung polykristalliner Szintillatoren für die Positronen-Emissions-Tomographie (PET)**
von S. K. Karim (2010), VIII, 154 Seiten
ISBN: 978-3-89336-610-1

56. **Kombination eines Gebäudekondensators mit H2-Rekombinatorelementen in Leichwasserreaktoren**
von S. Kelm (2010), vii, 119 Seiten
ISBN: 978-3-89336-611-8

57. **Plant Leaf Motion Estimation Using A 5D Affine Optical Flow Model**
by T. Schuchert (2010), X, 143 pages
ISBN: 978-3-89336-613-2

58. **Tracer-tracer relations as a tool for research on polar ozone loss**
by R. Müller (2010), 116 pages
ISBN: 978-3-89336-614-9

59. **Sorption of polycyclic aromatic hydrocarbon (PAH) to Yangtze River sediments and their components**
by J. Zhang (2010), X, 109 pages
ISBN: 978-3-89336-616-3

60. **Weltweite Innovationen bei der Entwicklung von CCS-Technologien und Möglichkeiten der Nutzung und des Recyclings von CO₂**
Studie im Auftrag des BMWi
von W. Kuckshinrichs et al. (2010), X, 139 Seiten
ISBN: 978-3-89336-617-0

61. **Herstellung und Charakterisierung von sauerstoffionenleitenden Dünnschichtmembranstrukturen**
von M. Betz (2010), XII, 112 Seiten
ISBN: 978-3-89336-618-7

62. **Politikszenarien für den Klimaschutz V – auf dem Weg zum Strukturwandel, Treibhausgas-Emissionsszenarien bis zum Jahr 2030**
hrsg. von P. Hansen, F. Chr. Matthes (2010), 276 Seiten
ISBN: 978-3-89336-619-4

63. **Charakterisierung Biogener Sekundärer Organischer Aerosole mit Statistischen Methoden**
von C. Spindler (2010), iv, 163 Seiten
ISBN: 978-3-89336-622-4

64. **Stabile Algorithmen für die Magnetotomographie an Brennstoffzellen**
von M. Wannert (2010), ix, 119 Seiten
ISBN: 978-3-89336-623-1

65. **Sauerstofftransport und Degradationsverhalten von Hochtemperaturmembranen für CO2-freie Kraftwerke**
von D. Schlehuber (2010), VII, 139 Seiten
ISBN: 978-3-89336-630-9

66. **Entwicklung und Herstellung von foliengegossenen, anodengestützten Festoxidbrennstoffzellen**
von W. Schafbauer (2010), VI, 164 Seiten
ISBN: 978-3-89336-631-6

67. **Disposal strategy of proton irradiated mercury from high power spallation sources**
by S. Chiriki (2010), xiv, 124 pages
ISBN: 978-3-89336-632-3

68. **Oxides with polyatomic anions considered as new electrolyte materials for solid oxide fuel cells (SOFCs)**
by O. H. Bin Hassan (2010), vii, 121 pages
ISBN: 978-3-89336-633-0

69. **Von der Komponente zum Stack: Entwicklung und Auslegung von HT-PEFC-Stacks der 5 kW-Klasse**
von A. Bendzulla (2010), IX, 203 Seiten
ISBN: 978-3-89336-634-7

70. **Satellitengestützte Schwerewellenmessungen in der Atmosphäre und Perspektiven einer zukünftigen ESA Mission (PREMIER)**
von S. Höfer (2010), 81 Seiten
ISBN: 978-3-89336-637-8

71. **Untersuchungen der Verhältnisse stabiler Kohlenstoffisotope in atmosphärisch relevanten VOC in Simulations- und Feldexperimenten**
von H. Spahn (2010), IV, 210 Seiten
ISBN: 978-3-89336-638-5

72. **Entwicklung und Charakterisierung eines metallischen Substrats für nanostrukturierte keramische Gastrennmembranen**
von K. Brands (2010), vii, 137 Seiten
ISBN: 978-3-89336-640-8

73. **Hybridisierung und Regelung eines mobilen Direktmethanol-Brennstoffzellen-Systems**
von J. Chr. Wilhelm (2010), 220 Seiten
ISBN: 978-3-89336-642-2

74. **Charakterisierung perowskitischer Hochtemperaturmembranen zur Sauerstoffbereitstellung für fossil gefeuerte Kraftwerksprozesse**
von S.A. Möbius (2010) III, 208 Seiten
ISBN: 978-3-89336-643-9

75. **Characterization of natural porous media by NMR and MRI techniques: High and low magnetic field studies for estimation of hydraulic properties**
by L.-R. Stingaciu (2010), 96 pages
ISBN: 978-3-89336-645-3

76. **Hydrological Characterization of a Forest Soil Using Electrical Resistivity Tomography**
by Chr. Oberdörster (2010), XXI, 151 pages
ISBN: 978-3-89336-647-7

77. **Ableitung von atomarem Sauerstoff und Wasserstoff aus Satellitendaten und deren Abhängigkeit vom solaren Zyklus**
von C. Lehmann (2010), 127 Seiten
ISBN: 978-3-89336-649-1

78.   **18th World Hydrogen Energy Conference 2010 – WHEC2010**
        Proceedings
        Speeches and Plenary Talks
        ed. by D. Stolten, B. Emonts (2010)
        ISBN: 978-3-89336-658-3

78-1.   **18th World Hydrogen Energy Conference 2010 – WHEC2010**
        Proceedings
        Parallel Sessions Book 1:
        Fuel Cell Basics / Fuel Infrastructures
        ed. by D. Stolten, T. Grube (2010), ca. 460 pages
        ISBN: 978-3-89336-651-4

78-2.   **18th World Hydrogen Energy Conference 2010 – WHEC2010**
        Proceedings
        Parallel Sessions Book 2:
        Hydrogen Production Technologies – Part 1
        ed. by D. Stolten, T. Grube (2010), ca. 400 pages
        ISBN: 978-3-89336-652-1

78-3.   **18th World Hydrogen Energy Conference 2010 – WHEC2010**
        Proceedings
        Parallel Sessions Book 3:
        Hydrogen Production Technologies – Part 2
        ed. by D. Stolten, T. Grube (2010), ca. 640 pages
        ISBN: 978-3-89336-653-8

78-4.   **18th World Hydrogen Energy Conference 2010 – WHEC2010**
        Proceedings
        Parallel Sessions Book 4:
        Storage Systems / Policy Perspectives, Initiatives and Cooperations
        ed. by D. Stolten, T. Grube (2010), ca. 500 pages
        ISBN: 978-3-89336-654-5

78-5.   **18th World Hydrogen Energy Conference 2010 – WHEC2010**
        Proceedings
        Parallel Sessions Book 5:
        Stategic Analysis / Safety Issues / Existing and Emerging Markets
        ed. by D. Stolten, T. Grube (2010), ca. 530 pages
        ISBN: 978-3-89336-655-2

78-6.   **18th World Hydrogen Energy Conference 2010 – WHEC2010**
        Proceedings
        Parallel Sessions Book 6:
        Stationary Applications / Transportation Applications
        ed. by D. Stolten, T. Grube (2010), ca. 330 pages
        ISBN: 978-3-89336-656-9

78 Set (complete book series)

18ᵗʰ World Hydrogen Energy Conference 2010 – WHEC2010
 Proceedings
ed. by D. Stolten, T. Grube, B. Emonts (2010)
  ISBN: 978-3-89336-657-6

79. **Ultrafast voltex core dynamics investigated by finite-element micromagnetic simulations**
by S. Gliga (2010), vi, 144 pages
ISBN: 978-3-89336-660-6

80. **Herstellung und Charakterisierung von keramik- und metallgestützten Membranschichten für die CO₂-Abtrennung in fossilen Kraftwerken**
von F. Hauler (2010), XVIII, 178 Seiten
ISBN: 978-3-89336-662-0

81. **Experiments and numerical studies on transport of sulfadiazine in soil columns**
by M. Unold (2010), xvi, 115 pages
ISBN: 978-3-89336-663-7

82. **Prompt-Gamma-Neutronen-Aktivierungs-Analyse zur zerstörungsfreien Charakterisierung radioaktiver Abfälle**
von J.P.H. Kettler (2010), iv, 205 Seiten
ISBN: 978-3-89336-665-1

83. **Transportparameter dünner geträgerter Kathodenschichten der oxidkeramischen Brennstoffzelle**
von C. Wedershoven (2010), vi, 137 Seiten
ISBN: 978-3-89336-666-8

84. **Charakterisierung der Quellverteilung von Feinstaub und Stickoxiden in ländlichem und städtischem Gebiet**
von S. Urban (2010), vi, 211 Seiten
ISBN: 978-3-89336-669-9

85. **Optics of Nanostructured Thin-Film Silicon Solar Cells**
by C. Haase (2010), 150 pages
ISBN: 978-3-89336-671-2

86. **Entwicklung einer Isolationsschicht für einen Leichtbau-SOFC-Stack**
von R. Berhane (2010), X, 162 Seiten
ISBN: 978-3-89336-672-9

87. **Hydrogen recycling and transport in the helical divertor of TEXTOR**
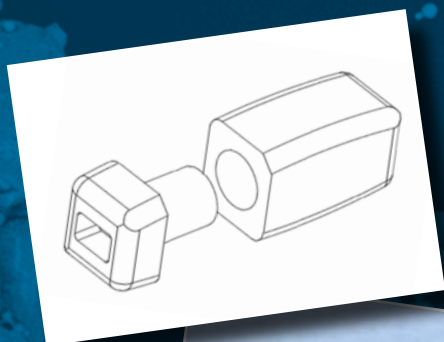by M. Clever (2010), x, 172 pages
ISBN: 978-3-89336-673-6

88. **Räumlich differenzierte Quantifizierung der N- und P-Einträge in Grund-wasser und Oberflächengewässer in Nordrhein-Westfalen unter besonde-rer Berücksichtigung diffuser landwirtschaftlicher Quellen**
von F. Wendland et. al. (2010), xii, 216 Seiten
ISBN: 978-3-89336-674-3

89. **Oxidationskinetik innovativer Kohlenstoffmaterialien hinsichtlich schwe-rer Lufteinbruchstörfälle in HTR´s und Graphitentsorgung oder Aufarbei-tung**
von B. Schlögl (2010), ix, 117 Seiten
ISBN: 978-3-89336-676-7

90. **Chemische Heißgasreinigung bei Biomassenvergasungsprozessen**
von M. Stemmler (2010), xv, 196 Seiten
ISBN: 978-3-89336-678-1

91. **Untersuchung und Optimierung der Serienverschaltung von Silizium-Dünnschicht-Solarmodulen**
von S. Haas (2010), ii, 202 Seiten
ISBN: 978-3-89336-680-4

92. **Non-invasive monitoring of water and solute fluxes in a cropped soil**
by S. Garré (2010), xxiv, 133 pages
ISBN: 978-3-89336-681-1

93. **Improved hydrogen sorption kinetics in wet ball milled Mg hydrides**
by L. Meng (2011), II, 119 pages
ISBN: 978-3-89336-687-3

94. **Materials for Advanced Power Engineering 2010**
ed. by J. Lecomte-Beckers, Q. Contrepois, T. Beck and B. Kuhn
(2010), 1327 pages
ISBN: 978-3-89336-685-9

95. **2D cross-hole MMR – Survey design and sensitivity analysis for cross-hole applications of the magnetometric resistivity**
by D. Fielitz (2011), xvi, 123 pages
ISBN: 978-3-89336-689-7

96. **Untersuchungen zur Oberflächenspannung von Kohleschlacken unter Vergasungsbedingungen**
von T. Melchior (2011), xvii, 270 Seiten
ISBN: 978-3-89336-690-3

97. **Secondary Organic Aerosols: Chemical Aging, Hygroscopicity, and Cloud Droplet Activation**
by A. Buchholz (2011), xiv, 134 pages
ISBN: 978-3-89336-691-0

98. **Chrom-bezogene Degradation von Festoxid-Brennstoffzellen**
von A. Neumann (2011), xvi, 218 Seiten
ISBN: 978-3-89336-692-7

99. **Amorphous and microcrystalline silicon applied in very thin tandem solar cells**
by S. Schicho (2011), XII, 190 pages
ISBN: 978-3-89336-693-4

100. **Sol-gel and nano-suspension electrolyte layers for high performance solid oxide fuel cells**
by F. Han (2011), iv, 131 pages
ISBN: 978-3-89336-694-1

101. **Impact of different vertical transport representations on simulating processes in the tropical tropopause layer (TTL)**
by F. Plöger (2011), vi, 104 pages
ISBN: 978-3-89336-695-8

102. **Untersuchung optischer Nanostrukturen für die Photovoltaik mit Nahfeldmikroskopie**
von T. Beckers (2011), xiii, 128 Seiten
ISBN: 978-3-89336-696-5

103. **Impact of contamination on hydrogenated amorphous silicon thin films & solar cells**
by J. Wördenweber (2011), XIV, 138 pages
ISBN: 978-3-89336-697-2

104. **Water and Organic Nitrate Detection in an AMS: Laboratory Characterization and Application to Ambient Measurements**
by A. Mensah (2011), XI, 111 pages
ISBN: 978-3-89336-698-9

105. **Entwicklung eines neuen Konzepts zur Steuerung der thermischen Ausdehnung von glaskeramischen Verbundwerkstoffen mit angepasster Fließfähigkeit am Beispiel der Hochtemperatur-Brennstoffzelle**
von E. Wanko (2011), xi, 134 Seiten
ISBN: 978-3-89336-705-4

106. **Tomographic reconstruction of atmospheric volumes from infrared limb-imager measurements**
by J. Ungermann (2011), xiv, 153 pages
ISBN: 978-3-89336-708-5

107. **Synthese und Identifizierung von substituierten Mg-Al-Cl Doppelhydroxidverbindungen mit Schwerpunkt IR-Spektroskopie**
von B. Hansen (2011), XII, 121 Seiten
ISBN: 978-3-89336-709-2

108. **Analysis of spatial soil moisture dynamics using wireless sensor networks**
by U. Rosenbaum (2011), xxii, 120 pages
ISBN: 978-3-89336-710-8

109. **Optimierung von APS-ZrO2-Wärmedämmschichten durch Variation der Kriechfestigkeit und der Grenzflächenrauhigkeit**
von M. E. Schweda (2011), 168 Seiten
ISBN: 978-3-89336-711-5

110. **Sorption of a branched nonylphenol isomer and perfluorooctanoic acid on geosorbents and carbon nanotubes**
by C. Li (2011), X, 102 pages
ISBN: 978-3-89336-716-0

111. **Electron Transport in the Plasma Edge with Rotating Resonant Magnetic Perturbations at the TEXTOR Tokamak**
by H. Stoschus (2011), iv, 113 pages
ISBN: 978-3-89336-718-4

112. **Diffusion and Flow Investigations in Natural Porous Media by Nuclear Magnetic Resonance**
by N. Spindler (2011), viii, 144 pages
ISBN: 978-3-89336-719-1

113. **Entwicklung und Erprobung des Hygrometer for Atmospheric Investigations**
von T. Klostermann (2011), IV, 118 Seiten
ISBN: 978-3-89336-723-8

114. **Application of functional gene arrays for monitoring influences of plant/seasons on bacterial functions and community structures in constructed wetlands (Bitterfeld, Germany)**
by J. Ning (2011), xiv, 157 pages
ISBN: 978-3-89336-724-5

115. **Wasseraustrag aus den Kathodenkanälen von Direkt-Methanol-Brennstoffzellen**
von A. Schröder (2011), VII, 228 Seiten
ISBN: 978-3-89336-727-6

116. **CITYZEN Climate Impact Studies**
ed. by M. Schultz (2011), 45 pages
ISBN: 978-3-89336-729-0

117. **Software Tools zum interoperablen Austausch und zur Visualisierung von Geodatensätzen über das Internet**
von M. Schultz, M. Decker, S. Lührs (2011), iv, 156 Seiten
ISBN: 978-3-89336-730-6

118. **Optimierung eines Leichtbaudesigns für ein SOFC-Brennstoffzellenstack**
von T. Nguyen-Xuan (2011), III, 154 Seiten
ISBN: 978-3-89336-732-0

119. **Institute of Energy and Climate Research IEK-6:**
Nuclear Waste Management & Reactor Safety Report 2009/2010
Material Science for Nuclear Waste Management
ed. by M. Klinkenberg, S. Neumeier, D. Bosbach (2011), 242 pages
ISBN: 978-3-89336-735-1

120. **Fate of the Antibiotic Sulfadiazine in Yangtze River Sediments: Transformation, Sorption and Transport**
by N. Meng (2011), XII, 111 pages
ISBN: 978-3-89336-736-8

121. **Thermodynamische Eigenschaften gasförmiger und kondensierter Verbindungen für Hochtemperaturanwendungen**
von T. Markus (2011), II, 131 Seiten
ISBN: 978-3-89336-728-3

122. **Ein neues LIF-Instrument für flugzeug- und bodengebundene Messungen von OH- und HO$_2$-Radikalen in der Troposphäre**
von S. Broch (2011), IV, 160 Seiten
ISBN: 978-3-89336-742-9

123. **Processes in the Yangtze River System - Experiences and Perspectives**
Workshop-Proceedings
ed. by S. Küpper, G. Subklew, R.-D. Wilken (2011), 83 pages
ISBN: 978-3-89336-744-3

124. **Thermo-Mechanical Properties of Mixed Ion-Electron Conducting Membrane Materials**
by B. Huang (2011), 130 pages
ISBN: 978-3-89336-746-7

125. **Growth, Etching, and Stability of Sputtered ZnO:Al for Thin-Film Silicon Solar Cells**
by J. I. Owen (2011), xv, 192 pages
ISBN: 978-3-89336-749-8

126. **Entwicklung geträgerter Ba$_{0,5}$Sr$_{0,5}$Co$_{0,8}$Fe$_{0,2}$O$_{3-\delta}$ Sauerstoff-Permeationsmembranen**
von F. Schulze-Küppers (2011), ii, 119 Seiten
ISBN: 978-3-89336-752-8

127. **Development of the 2-Component-Injection Moulding for Metal Powders**
by A. P. Cysne Barbosa (2011), XIV, 150 pages
ISBN: 978-3-89336-753-5

JÜLICH
FORSCHUNGSZENTRUM